CHARGE-CHANGING CROSS-SECTIONS

OF

$N_1^+(\sigma_{12})$ AND $Ar^{++}(\sigma_{21})$ IN Ne, Ar, and Kr

by

Ho Chun SUK

A thesis submitted to the School of Graduate Studies of the University of Ottawa in partial fulfilment of the requirements for the degree of Doctor of Philosophy.

Department of Physics
Faculty of Science and Engineering
University of Ottawa
Ottawa, Canada
1976.

ABSTRACT

The absolute total cross-sections were measured for both the single electron loss collisions of N_1^+(30 keV - 150 keV) ions and the single electron capture collisions of Ar^{++}(50 keV - 200 keV) ions on the gas targets Ne, Ar, and Kr.

The power series solution of the differential equations for a four-charge-component system in the beams was used to determine the cross-sections. It was found that both the low order target thickness corrections and the angular and energy spread corrections are significant, so that it was shown not only that the conventional observation of a linear function between the counting rate ratio and the target gas pressure is an unreliable method for the single collision conditions, but also that the lack of agreement among the previous measurements seems to be explainable in terms of the different angular spread and target thickness treatments.

Using the corrected energy defects, the two-state theory of Rapp and Francis-Lee and Hasted fits well to both the absolute magnitudes and the energy variations of the present electron loss cross-sections, but not so well to the electron capture cross-sections. Firsov's statistical theory which describes electron stripping is unable to account for the considerable differences in the electron loss cross-sections between the three targets. The difference between theory and experiment are to be expected in view of the crudity of the theory and the many approximations which it assumes.

ACKNOWLEDGEMENTS

I wish to sincerely express my heartfelt appreciation to Dr. B. Hird for his encouragement, illuminating discussions, and candid comments during the course of this work. Financial assistance from Professor Hird, in the form of a N.R.C. research assistantship held during this work, is gratefully acknowledged.

Professor Hird originally planned the present atomic collisions laboratory of the University of Ottawa and supervised the set-up and construction of the apparatus in the laboratory.

I would like to thank Dr. B. Logan for candid discussions on a number of instrumental problems during the setting-up and construction of the apparatus.

I would like to thank the staff of the machine and electronics shop of the Department of Physics, University of Ottawa, for their assistance in the setting-up and construction of the apparatus. I would also like to thank Mrs. L. Leroux for typing this thesis.

Finally, thanks are due to my parents and my wife, Mi Hae, for their constant aid and encouragement.

TABLE OF CONTENTS

LIST OF TABLES

LIST OF FIGURES

CHAPTER I INTRODUCTION

Over the last 20 years, a number of experiments[3-8] have been done to measure the absolute or differential cross-sections for the single electron loss of fast N_1^+ ions and the single electron capture of fast Ar^{++} ions during their passage through target gases.. This thesis describes measurements of the absolute total cross-sections for the asymmetric processes of both the single electron loss of N_1^+ ions and the single electron capture of Ar^{++} ions during their passage through the inert gas targets Ne, Ar, and Kr, where the ion energy ranges of the N_1^+ and Ar^{++} ions are from 30 keV to 150 keV and from 50 keV to 200 keV, respectively. Some parts of this work have already been published[1,2].

There are two theoretical papers[9,13] which give the atomic asymmetric charge-changing cross-sections in a form suitable for practical use in the present projectile velocity ranges. These theories have been based one of two opposite simplifying assumptions. One assumption[9-12] is a two-state approximation to the quantum mechanical model which assumes only one final state to be significantly populated in the interaction. The predictions of this theory for asymmetric collisions show a rise in the cross-section with energy to a maximum which corresponds to the Massey criterion[11] followed by a steady decrease at higher energies. The present results of both the single electron loss and capture cross-section measurements are compared with the two-state, quasi-adiabatic theory in a numerical form which was given by Lee and Hasted[10] who had slightly modified the asymmetric cross-section theory by Rapp and Francis[9]. The other simplifying assumption[13] is a statistical approximation to the electron stripping model which considers the transferred electron to be statistically excited into one of a large number of closely spaced states of a Thomas-Fermi gas. This statistical theory ignores all the quantized details of the electronic structures. For a given incident ion or atom, the statistical theory predicts the cross-section to increase with increasing atomic number of the target and with increasing impact energy.

Both the two-state and statistical theories are summarized in section II-1, and the comparison with the present experimental data of charge-changing cross-sections is described in section V-2, of Chapter V.

There is considerable conflict in the previous experimental data[3-8]. These discrepancies between data from different groups are an interesting aspect of experimental technique. A discussion of these experiments appears in section II-2 of Chapter II.

The ions from our 150 kV accelerator could be accurately defined in energy and direction both before and after passing through the thin gas target. Integration over the angle and energy of the charge-changed ions was investigated and corrections made to eliminate the errors due to small angular variations of the ion detection system. The experimental arrangement and apparatus used in this work are described in detail in Chapter III.

It has become customary to express the probability of a charge-changing collision by a total cross-section σ_{if} where i represents the initial charge of the incident ions in units having the magnitude of the electronic charge and f is the charge after the event. During the ion passage through a thin target, the cross section σ_{if} is defined by $dN^f/d\pi = \sigma_{if}N^i$ where N^i and N^f are the numbers of the ions to be found respectively with charges i and f in a beam before and after the collision, and π is the target thickness expressed as the number of target particles per unit cross-sectional area. The integration of the differential equation for a finite target thickness and the expansion as a power series in the target thickness are discussed in Chapter IV of experimental method and procedure.

The experimental results and discussions are presented in Chapter V, and the conclusions in Chapter VI.

CHAPTER II BACKGROUND OF THEORY AND PREVIOUS EXPERIMENTAL MEASUREMENTS

This part of the thesis describes the two-state theory and the statistical theory for atomic charge-changing cross-sections, and describes previous experimental measurements. The comparison of the theories and previous experimental data with the present results is given in Chapter V.

II-1A Two Two-state Theory

The group of atomic or molecular collision theories which consider only one final state is called the two-state theory. Collisions can be considered "slow" or "fast" depending on whether the velocity of the active electron is greater or less than the relative velocity of the two nuclei. Roughly, these correspond to ion velocity less than 10^4 cm/sec and more than 10^9 cm/sec, respectively. A region of "intermediate" velocities occurs where the ion velocities are not higher than the electron velocities, but at the same time they are great enough for a straight line trajectory approximation to be reasonably valid.

Symmetric collisions

The symmetric collision, where an electron is exchanged between identical particles, is easier to treat and will be considered first, following the method of Gurnee and Magee[14] for a charge transfer process $A^+ + (A^+ + e^-) \rightarrow (A^+ + e^-) + A^+$.

Denoting atomic orbital wave functions w_i and w_f for the target and scattered atoms $(A^+ + e^-)$ which behave asymptotically like the reactants $A^+ + (A^+ + e^-)$ and like the products $(A^+ + e^-) + A^+$, respectively, the total wave function W and the total Hamiltonian for the collision complex A_2^+ system may be expressed, respectively as

$$W = (c_i w_i + c_f w_f) \exp(-iEt/\hbar) \tag{2-1}$$

$$H = H_o + H_i \tag{2-2}$$

where $H_o W = EW$, and c_i and c_f are complex numbers which are functions of the time t. H_o is that part of the Hamiltonian which represents the sum of the internal energies and electronic energies of the atom and ion, and H_i is that part of the Hamiltonian which represents the interaction between the electron and the other ion. Substitution of eqs. (2-1) and (2-2) into the time dependent Schrodinger equation $i\hbar(dW/dt) = HW$ yields:

$$i\hbar \left[\frac{d(c_i w_i)}{dt} + \frac{d(c_f w_f)}{dt} \right] = c_i H_i w_i + c_f H_i w_f \tag{2-3}$$

from which, multiplying by w_i^* and w_f^* and integrating over all space coordinates, a set of coupled equations is obtained

$$i\hbar \left[\frac{dc_i}{dt} + \frac{dc_f}{dt} F \right] = c_i H_{ii} + c_f H_{if} \tag{2-4}$$

$$i\hbar \left[\frac{dc_i}{dt} F + \frac{dc_f}{dt} \right] = c_i H_{fi} + c_f H_{ff} \tag{2-5}$$

where $H_{if} = \int w_i^* H_i w_f dV$ and similar definitions for H_{ii}, H_{ff}, and H_{fi},

$F = \int w_i^* w_f dV = \int w_f^* w_i dV$, and $\int w_i^* w_i dV = \int w_f^* w_f dV = 1$, in which V is the total volume with the element dV.

Gurnee and Magee[14] wrote the initial and final probability amplitudes as

$$c_i = g \exp(iz) \tag{2-6}$$

$$c_f = i(1 - g^2)^{\frac{1}{2}} \exp(iz) \tag{2-7}$$

where g and z are functions of time. Substituting eqs. (2-6) and (2-7) into either eq. (2-4) or eq. (2-5), equating the real and imaginary parts from the equation, and then integrating these two equations using $dt = dx/v$ where v is the ion velocity assumed to be constant, the final result of Gurnee and Magee[14] is that the probability $P_s(b,v)$ of symmetric resonance charge transfer in the collision with impact parameter b is given by

$$P_s(b,v) = c_f^* c_f(t = \infty) = \sin^2 \int_{-\infty}^{+\infty} \frac{(H_{fi} - F\,H_{ii})}{\hbar v(1 - F^2)} dx \tag{2-8}$$

where $H_{if} = H_{fi}$ and $H_{ii} = H_{ff}$ for the symmetric collision.

If it can be assumed that the important electron exchange region is outside the region of high electron density, then the valence electron is approximately in an atomic hydrogen-like state. A suitable wave function for the $(A^+ + e^-)$ system is then the Iovitsu and Ionescu-Pallas[15] one electron wave function which was used by Rapp and Francis[9]

$$w_{i,f}(r) = (\pi a_o^3)^{-\frac{1}{2}} \ (I/13.6)^{3/4} \exp[- (I/13.6)^{\frac{1}{2}} \ r/a_o] \tag{2-9}$$

where I is the ionization potential in electron volts of the atom A,

a_o is the Bohr radius, and r is the separation of A^+ from e^-. Eq. (2-9) is the equation of an atomic hydrogen-like wave function, but has been corrected to agree asymptotically with the binding energy I of the valence electron.

A variational calculation can be used to show that

$$\frac{H_{if} - F\,H_{ii}}{1 - F^2} = \tfrac{1}{2}(E_s - E_a) \qquad (2\text{-}10)$$

where $E_{s,(a)}$ are the energies of the symmetric (antisymmetric) states of the molecular ion A_2^+. Assuming $R^2 = x^2 + b^2$ to be large compared with $(a_o/\gamma)^2$ where $\gamma = (I/13.6)^{\frac{1}{2}}$ and using the wave function of eq. (2-9), the resonance splitting $(E_s - E_a)$ is calculated as

$$E_s - E_a = 2I\,\frac{R}{a_o}\,\exp(-\gamma R/a_o) \qquad (2\text{-}11)$$

where R is the internuclear separation.

Substituting eq. (2-11), through eq. (2-10), into eq. (2-8), the probability is given in the form

$$P_s(b,v) = \sin^2 \int_{-\infty}^{+\infty} (I/a_o\hbar v)\,(x^2 + b^2)^{\frac{1}{2}} \exp[-\gamma(x^2 + b^2)^{\frac{1}{2}}/a_o]\,dx \qquad (2\text{-}12)$$

This integral has been evaluated by Dalgarno et al.[16], the result being

$$P_s(b,v) = \sin^2\left\{ \frac{2Ib^2}{a_o\hbar v}\left[K_o(\gamma b/a_o) + \frac{K_1(\gamma b/a_o)}{(\gamma b/a_o)} \right] \right\} \qquad (2\text{-}13)$$

where $K_o(\gamma b/a_o)$ and $K_1(\gamma b/a_o)$ are the zero- and first-order modified Bessel functions of the second kind, respectively.

The cross section for the symmetric resonant charge transfer collision is then calculated from

$$\sigma_s(b,v) = 2\pi \int_o^\infty P_s(b,v)\ b\ db \qquad (2\text{-}14)$$

Asymmetric Collisions

Atomic asymmetric charge transfer collisions of the type $A^+ + (B^+ + e^-) \rightarrow (A^+ + e^-) + B^+$ were treated by Rapp and Francis[9]. These differ from the symmetric collisions in that the molecular wave function cannot be expressed as either a symmetric or an antisymmetric wave function, and that the initial and final state energies are different. The energy difference, the so-called energy defect, Q is given by

$$Q = E_f\ (R \rightarrow \infty) - E_i(R \rightarrow \infty) = I_A - I_B \qquad (2\text{-}15)$$

The LCAO wave function, equivalent to eq. (2-1), is written as

$$W_a = c_A w_A \exp(-I_A t/\hbar) + c_B w_B \exp(-I_B t/\hbar) \qquad (2\text{-}16)$$

with the same approximations as before, that w_A is the atomic orbital wave function for the $(A^+ + e^-)$ system which behaves asymptotically like the products $(A^+ + e^-) + B^+$, and w_B is the atomic orbital wave function for the $(B^+ + e^-)$ which behaves asymptotically like the reactants $A^+ + (B^+ + e^-)$. The perturbations H_A and H_B on their initial and final systems are different. Similar algebra to that used to obtain eqs. (2-4) and (2-5) results in the simultaneous equations to the time-dependent coefficients c_A and c_B

$$i \frac{dc_B}{dt} = k_1(t)\ c_A \exp(i\delta t) + n_1(t)\ c_B \tag{2-17}$$

$$i \frac{dc_A}{dt} = n_2(t)\ c_A + k_2(t)\ c_B \exp(i\delta t) \tag{2-18}$$

where

$$k_1(t) = \left[\frac{(H_B)_{BA} - F(H_B)_{AA}}{(1 - F^2)\hbar} \right], \quad k_2(t) = \left[\frac{(H_A)_{AB} - F(H_A)_{BB}}{(1 - F^2)\hbar} \right]$$

$$n_1(t) = \left[\frac{(H_A)_{BB} - F(H_A)_{AB}}{(1 - F^2)\hbar} \right], \quad n_2(t) = \left[\frac{(H_B)_{AA} - F(H_B)_{BA}}{(1 - F^2)\hbar} \right]$$

Here, F is the overlap integral as before, $(H_a)_{bc} = \int w_b^* H_a w_c dV$, and $\delta = (I_A - I_B)/\hbar$. Rapp and Francis[9] examined the behaviour of the perturbation integrals at large impact parameters and concluded that $k_2(t) \simeq (H_A)_{AB}$, $k_1(t) \simeq (H_B)_{BA}$, and $k >> n$. A difficulty arises because of the different choices of the perturbations for the initial and final states that[17]

$$(H_A)_{AB} - (H_B)_{BA} = (I_A - I_B)F \tag{2-19}$$

In the limit of the small energy defect, the difference of equation (2-19) becomes small, and with the large impact parameter approximation the simultaneous equations of eqs. (2-17) and (2-18) become

$$i\,\frac{dc_B}{dt} = \bar{k}\; c_A\; \exp(i\delta t) \qquad (2\text{-}20a)$$

$$i\,\frac{dc_A}{dt} = \bar{k}\; c_B\; \exp(-i\delta t) \qquad (2\text{-}20b)$$

where $\bar{k}$ is an appropriate mean of $k_1(t)$ and $k_2(t)$.

Using $dx/dt = v$ as before, these become

$$i\,\frac{dc_B}{dx} = [k(x/v)\;\; c_A\; \exp(i\delta x/v)]/v \qquad (2\text{-}21)$$

$$i\,\frac{dc_A}{dx} = [k(x/v)\;\; c_B\; \exp(-i\delta x/v)]/v \qquad (2\text{-}22)$$

When the phase factors of eqs. (2-21) and (2-22) vary so slowly that they are roughly constant over the interaction region, corresponding to either a small energy defect or a high ion velocity, then these equations reduce to the symmetric case, and a similar treatment to that for eq. (2-9) gives

$$|c_A\;(\infty)|^2 = \sin^2 \int_{-\infty}^{+\infty} (1/v)\bar{k}\; dx$$

so that $\bar{k}$ is to be associated with the $E_a - E_s$ of the symmetric collisions. At somewhat lower ion velocities, or higher energy defects, the phase factor oscillates through the interaction region. Gurnee and Magee[14] postulated that the eqs. (2-17) and (2-18) have asymptotically solutions of the form

$$c_A = [\sin \int_{-\infty}^{x} (\bar{k}/v)\;\exp(-i\delta x/v)dx]\;\exp[\,-i \int_{-\infty}^{x}(n_1/v)dx] \quad (2\text{-}23a)$$

$$c_B = [\cos \int_{-\infty}^{x} (\bar{k}/v)\;\exp(-i\delta x/v)dx]\;\exp[\,-i \int_{-\infty}^{x}(n_2/v)dx] \quad (2.23b)$$

which satisfy the simultaneous equations and are out of phase with each other as is required from the Hermiticity of the interaction. These equations give

$$|c_A(+\infty)|^2 = \sin^2 \int_{-\infty}^{+\infty} (\bar{k}/v) \cos (\delta x/v)\, dx \tag{2-24}$$

since $\bar{k}$ is an even function of x.

A slightly different approximation was made by Rosen and Zener who postulated that they could replace $\bar{k}$ by $y_1 \operatorname{sech}(y_2 x)$ which has the correct general shape. They showed that the general form of the solution to the differential equations of eqs. (2-21) and (2-22) is then

$$|c_A(+\infty)|^2 = \frac{[\sin^2 \int_{-\infty}^{+\infty}(\bar{k}/v)\,dx]\,[\int_{-\infty}^{+\infty}(\bar{k}/v) \cos(\delta x/v)\,dx]^2}{[\int_{-\infty}^{+\infty}(\bar{k}/v)\,dx]^2} \tag{2-25}$$

which gives immediately

$$|c_A(+\infty)|^2 = [\sin^2(\pi y_1/v y_2)][\operatorname{sech}^2(\pi\delta/2 v y_2)] \tag{2-26}$$

Skinner[19] compared numerically the equations of Gurnee and Magee[14], eq (2-23) and Rosen and Zener[18], eq. (2-25) with each other, and with an exact integration using several simple analytical expressions for $\bar{k}$. The Rosen and Zener Approximation[18] was on the whole rather better than the other, and was chosen by Rapp and Francis.

In order to find the suitable constants y_1 and y_2, Rapp and Francis[9] compared the Rosen and Zener form

$$\bar{k} = y_1 \operatorname{sech}(y_2 x) \tag{2-27}$$

to the equivalent $\bar{k}$ form in the symmetric collisions which was obtained from the hydrogen-like wave functions,

$$\bar{k} = (I/a_o\hbar)(x^2 + b^2)^{\frac{1}{2}} \exp\left[-\gamma(x^2 + b^2)^{\frac{1}{2}}/a_o\right] \tag{2-28}$$

with I some suitable mean between I_A and I_B. Matching the two forms at x = 0 and normalizing both, the solutions for y_1 and y_2 are

$$y_1 = (I/a_o\hbar)b \exp(-j) \tag{2-29}$$

$$y_2 = \{\pi \exp(-j)\}/\{2b [K_o(j) + K_1(j)/j]\} \tag{2-30}$$

where

$$j = \gamma b/a_o \tag{2-31}$$

Substituting these into eq. (2-26) the probability $P_a(b,v)$ of an asymmetric charge tranfer is given by

$$P_a(b,v) = s\, P_s(b,v) \operatorname{sech}^2 [(\delta a_o/\gamma v)F(j)] \tag{2-32}$$

where

$$F(j) = j[\exp(j)][K_o(j) + K_1(j)/j] \tag{2-33}$$

and $P_s(b,v)$ is the symmetric charge transfer probability. Here, the statistical weighting factor s is the fraction of the initial molecular states which have the correct quantum numbers to form allowed final molecular states after the charge transfer. Only those initial molecular states with the same symmetry and the same spin configurations as the final molecular states can produce charge transfer in this theory.

Rapp and Francis[9] approximated the Bessel functions by their first term in the large argument expansions[20]

$$K_o(j) \simeq K_1(j) \simeq (\pi/2j)^{\frac{1}{2}} \exp(-j) \tag{2-34}$$

to obtain

$$P_s(b,v) = \sin^2 [(2\pi/\gamma^2)^{\frac{1}{2}} (Ia_o/\hbar v) \; j^{3/2} (1 + 1/j) \exp(-j)] \tag{2-35}$$

for the probability of symmetric charge transfer. It turns out that the argument of the $\sin^2$ function in this expression lies with a few percent of the argument of the $\sin^2$ function in the more general expression for $P_s(b,v)$ of eq. (2-13) when j is greater than about unity. For velocities less than, for example, 1.4×10^8 cm/sec (140 keV N_1^+), this approximation is quite good for most of the range of b, and the cross-section of eq. (2-14) is well reproduced, with little error due to this approximation. The sech^2 function in $P_a(b,v)$ of eq. (2-32) is also simplified by the Bessel function expansion to[9]

$$\text{sech}^2[(\delta/v)\ (a_o\pi b/2\gamma)^{\frac{1}{2}}]$$

Rapp and Francis[9] considered three regions of velocity v. When v is large, the argument of the sech^2 function is small, so that the sech^2 term is approximately unity. With this latter approximation the sech^2 term factors out of the integral, and the cross-section $\sigma_a(b,v)$ for asymmetric charge transfer becomes

$$\sigma_a(b,v) = 2\pi \int_o^\infty P_a(b,v)\ b\ db \qquad (2\text{-}36)$$

$$= s\ \sigma_s(b,v) \qquad (2\text{-}37)$$

Thus the cross-section for asymmetric charge transfer decreases with increasing velocity in the same way as the cross-section for symmetric charge transfer.

At the other extreme, for small velocities, the sech^2 term decreases more rapidly than the $P_s(b,v)$ with increasing b. The $P_s(b,v)$ function oscillates rapidly between 0 and 1 throughout the important region of small b, so that it can be averaged to $P_s(b,v) = \frac{1}{2}$. The cross-section $\sigma_a(b, v)$ then becomes:

$$\sigma_a(b,v) = (8/\pi)(\gamma/a_o)^2(v/\delta)^4 \int_o^\infty [\mathrm{sech}^2(u)]\, u^3\, du \qquad (2\text{-}38)$$

where

$$u = (\delta/v)(a_o\pi b/2\gamma)^{\frac{1}{2}} \qquad (2\text{-}39)$$

and the integral equals 1.147. Thus the cross-section increases with ion energy at the lowest velocities and decreases with ion energy at the highest velocities.

In between them there is a maximum which is the equivalent of the Massey criterion[11] for the adiabatic maximum rule, and which physically corresponds to a few oscillations of the quantum beats between the initial and final states. The maximum is therefore expected in the region of v such that $(\delta X_a/2\pi v) \simeq 1$, where the so-called adiabatic parameter X_a is some measure of the interaction length and is of the order of atomic dimensions[11,12]. Hasted and Lee[12] have found. empirically that the product of X_a and the number of electrons transferred is equal to 7Å for a wide range of charge transfer collisions. Mathematically this velocity region represents the situation where the probability $P_s(b,v)$ and the sech^2 term both vary significantly with b in the important region. In the intermediate velocity region, Rapp and Francis [9] chose an upper limit of integration of eq. (2-23), $b = b_1$, which was determined by the relative magnitudes of the sech^2 function and the probability $P_s(b,v)$ of eq. (2-32). Their condition for the choice of b_1 was the largest value of b to satisfy

$$P_s(b_1, v) = \tfrac{1}{4}\,\mathrm{sech}^2\left[(\delta/v)(a_o\pi b_1/2\gamma)^{\frac{1}{2}}\right] .$$

Lee and Hasted [10] chose an upper limit of integration b_1 such that it is the largest value of b to satisfy $P_s(b, v) = \sin^2(\pi/6)$ in the approximation of eq. (2-32). Dalgarno[16] chose a slightly smaller upper limit, b_1, such that $P_s(b, v) = \sin^2(\pi/4)$. For values of b below this upper limit b_1, $P_s(b_1, v)$ was set to ½ so that the cross-section for the asymmetric charge transfer is given by

$$\sigma_a(b_1, v) = \tfrac{1}{2}\, s \int_o^{b_1} [\mathrm{sech}^2(\delta/v)(a_o\pi b/2\gamma)^{\frac{1}{2}}]\, 2\pi b\, db$$

$$= s\, \tfrac{1}{2}\pi b_1^2\, \Phi(u_1) \tag{2-40}$$

where

$$\Phi(u_1) = (4/u_1^4) \int_o^{u_1} [(\mathrm{sech}^2(u)]\, u\, du \tag{2-41}$$

and u_1 is the value of eq. (2-39) when $b = b_1$. Table AI-2 in Appendix I is a more detailed table than the one given for the integral $\Phi(u_1)$ by Lee and Hasted[10].

To examine the accuracy of some of the approximations, calculations were made at 30 keV and 140 keV for the $N_1^+ \to$ Ne collisions which have an average ionization potential of 14.8 eV and a (corrected) energy defect of 11.3 eV. Fig. 2-1 shows the probability $P_s(b, v)$ of symmetric charge transfer given by eq. (2-13) and for comparison its approximation given by eq. (2-35). Also shown are $\mathrm{sech}^2 [(\delta a_o/\gamma v)\, F(\gamma b/a_o)]$ and approximation $\mathrm{sech}^2[(\delta/v)(a_o\pi b/2\gamma)^{\frac{1}{2}}]$. The values of b_1 as defined by the different authors[9,10,16] are shown in the sech^2 distributions.

The approximation $P_s(b, v) = \frac{1}{2}$ was compared to the average value over the range of b from zero to b_1 using eq. (2-35) and the various definitions of b_1:

Fig.2-1

The following calculations were made at the velocity $v=6.47 \times 10^7$ cm/sec(30 keV) and $v=1.34 \times 10^8$ cm/sec(140 keV) for the $N_1^+ \rightarrow Ne$ collisions which have an average ionization potential of 14.8 eV and a corrected energy defect of 11.3 eV.

(A). The arguments of $\sin^2$ functions that occur in Eqs.(2-13) and (2-35)

(B). The $\sin^2$ functions showing the probabilities, $P_s(b,v)$, of symmetric charge transfer vs. impact parameter at a fixed ion velocity.

(C). The $\mathrm{sech}^2[(\delta a_o/\gamma v)\ F(j)]$ and its approximation $\mathrm{sech}^2[(\delta/v)(a_o\pi b/2\gamma)^{\frac{1}{2}}]$, which occur in Eqs.(2-42) and (2-40), respectively, vs. impact parameter at a fixed ion velocity. Also shown are the values of the impact parameter b_1(in atomic units) defined by the different authors, Rapp and Francis(=RF)[9], Lee and Hasted(=LH)[10], and Dalgarno(=D)[16].

Fig.2-1

$\sigma_{12}(N_1^+ \rightarrow Ne)$ Collision(I=14.8 eV; Q_c=11.3 eV)

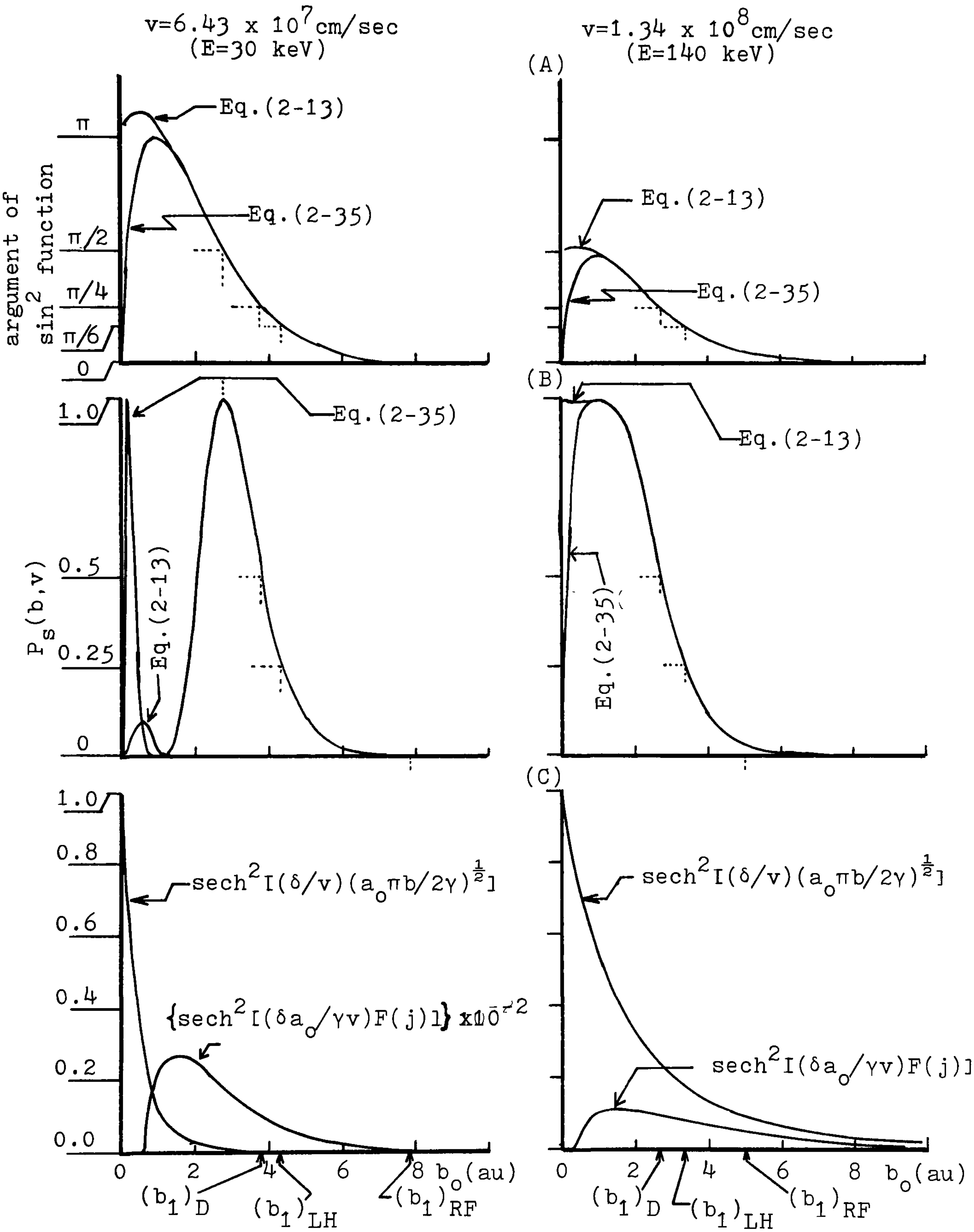

velocity	6.43×10^7 cm/sec	1.34×10^8 cm/sec
$P_s(RF^9)$	0.29	0.54
$P_s(LH^{10})$	0.48	0.73
$P_s(D^{16})$	0.50	0.83

The more accurate value of the integral obtained from

$$\sigma_a(b, v) = s \int_o^\infty \{\sin^2[(2Ia_o/\gamma^2\hbar v) j\ F(j)]\ \mathrm{sech}^2[(\delta a_o/\gamma v)\ F(j)]\}2\pi b\ db \qquad (2\text{-}42)$$

by numerical integration is compared with intermediate velocity approximation of eq. (2-40):

velocity	6.43×10^7 cm/sec	1.34×10^8 cm/sec
σ_a/s;eq. (2-42)	1.30×10^{-18} cm^2	2.32×10^{-17} cm^2
$\sigma_a(b_1 \equiv LH^{10})/s$;eq. (2-40)	7.30×10^{-17} cm^2	1.63×10^{-16} cm^2

It can be seen that in this intermediate velocity region both the approximation eq. (2-35) for eq. (2-13) and the approximation $P_s(b_1, v) = \frac{1}{2}$ are quite good, but on the other hand, the approximation to the Bessel functions in the sech^2 function of eq. (2-32) is poor.

Moreover because the shape of the $P_s(b, v)$ function in the integral of eq. (2-42) is far from being constant, the approximation of eq. (2-40) is very poor.

Since the Rapp and Francis formalism[9], as modified by Lee and Hasted[10] is the only two-state theory in a convenient numerical form, this was used in the comparison with experimental results in spite of its many crude approximations.

Corrections to obtain Effective Energy Defects

Hasted and Lee[12] considered that, during an atomic collision, the effective energy defect at the interaction distance r must be changed by an energy E_i from the energy defect Q which is calculated for infinite internuclear separations. Their work was initially based on a survey of the cross-section maxima, which they found to be much more uniform when the E_i corrections were included. They considered the Coulomb interaction energy E_c between the final products of the process $A^{n+} + B^{o} \rightarrow A^{(n-m)+} + B^{m+} + Q$ when $n \neq m$

$$E_c = (n-m)m\, e^2/r \qquad (2\text{-}44)$$

and the polarization energy E_p due to the induced dipole interaction of the atom due to the charge ne of the ion

$$E_p = -n\,(P_A - P_B)\; e^2/2r^4 \qquad (2\text{-}45)$$

where P_A and P_B are the polarizabilities of A and B atoms. Since the polarization correction was much smaller than the Coulomb correction, it was neglected when the Coulomb correction was present. Hasted and

Lee[12] estimated the mean of the Coulomb interaction energy in a spherically symmetric charge distribution by

$$\bar{E}_c = \left(\int_{r_1}^{r_2} E_c \, 4\pi \, r^2 \, dr\right) / \left(\int_{r_1}^{r_2} 4\pi \, r^2 dr\right)$$

$$= \frac{3}{2}(n-m)\, m \, e^2 \, (r_1^2 - r_2^2)/(r_1^3 - r_2^3) \qquad (2\text{-}46)$$

To obtain the limits on the effective interaction radii, they performed a graphical integration procedure using radial density functions for a typical atom (argon) which took some account of screening to obtain

$$r_1 = 1.44 \left[(Z_A - n)^{3/2} + Z_B^{3/2}) \right]^{1/2} \quad \text{a.u.} \qquad (2\text{-}47a)$$

$$r_2 = (0.48/1.44)\, r_1 \qquad (2\text{-}47b)$$

where Z_A and Z_B are the atomic numbers of A and B atoms, respectively. The corrected energy defect Q_c is in most cases a significant correction to the mean energy defect $\bar{E}_c$, and in some cases it may even change the sign of the effective energy defect.

II-1B The Statistical Theory

The statistical model of electron stripping cross-sections assumes that the charge-changing process in slow collisions above the ionization threshold proceeds by means of a large number of crossings, or pseudo-crossings of the interatomic potential curves of the two heavy systems in a two-state theory developed by Landau[21], Zener[22], and Stueckelberg[23]. The process corresponding to the ionization has been also theoretically treated, assuming it to be statistical in nature, by Mittleman and Wilets[24], Russek and co-workers[25], and Firsov[13] who worked independently. Among their formulations, only Firsov[13] derived a formula for the electron stripping cross-sections without unknown phenomenological parameters. Taking account of collisional ionization process as a friction-like mechanism, he considered the process as an evaporation of electrons from the heated electron gas during the collision. The ionization potential was computed from a Thomas-Fermi atom, and the result[13] is given in the form

$$\sigma = \sigma_o \left[(v/v_o)^{1/5} - 1 \right]^2 \qquad \text{cm}^2 \tag{2-48}$$

with

$$\sigma_o = 33 \times 10^{-16} / (Z_A + Z_B)^{2/3} \qquad \text{cm}^2 \tag{2-49}$$

and

$$v_o = 23 \times 10^6 \; I/(Z_A + Z_B)^{5/3} \qquad \text{cm/sec} \tag{2-50}$$

where v is the impact velocity in cm/sec, I is equal to the smaller ionization potential, in eV, of the two colliding atoms, and Z_A and Z_B are the atomic numbers of projectile and target atoms, respectively. This formula was derived for the electron stripping cross-sections in collisions between neutral-neutral atoms, which implies that the electrons are stripping from both the projectile and target particles. As a result of comparisons between some experiments and this formula, he suggested that eq. (2-48) generally gives the cross-section for ionization for any pair of colliding atoms over a wide range of relative velocity with an accuracy to a factor of two. A recent survey by Fleischmann et al.[26] compared this formula with previous available experimental data.

II-2. Previous Experimental Measurements

The present review includes details of previous experimental measurements and uncertainties. It is confined to atomic collisions of $N_1^+(\sigma_{12})$ and $Ar^{++}(\sigma_{21})$ ions on the Ne, Ar, and Kr atoms at projectile ion energies above a few keV.

In all the published measurements, a particle beam of the desired degree of ionization was prepared with an accelerator and usually a magnetic analyzer. After the passage through a thin gas target in which only single collisions of the beam particles were assumed to occur, the collision products in the beam were analyzed with a magnetic or electrostatic analyzer. They measured directly the cross-section σ_{if} for transition from one ionization state i of the projectile to another state f by finding the variation of the fraction of the scattered and projectile intensities as a function of the target gas pressure.

Early measurements by Fedorenko[7] were carried out to determine the total cross-sections σ_{12} [N_1^+ (10 keV)→ H_2, Ne, N_2, Ar; N_1^+ (20 keV) → Kr] and σ_{21} Ar^{++}[(6-60 keV) → Ne, N_2, Ar]. The cross-sections, which included all the scattering angles up to 5°, were obtained, and the experimental uncertainties were estimated as ±50%.

Measurements by Dimitriev et al.[5] were reported on the total cross-sections σ_{12} and $\sigma_{i,i+1}$ for the collisions of N_1^+ (500 keV - 2400 keV) in He, H_2, Ar, and Kr, and were confined to projectile scattering angles up to 5 mili-radians, whereas Pivovar et al.[4] measured the differential and integral cross-sections for N_1^+ (250 keV -

1400 keV) ions in Ne, Ar, Kr, and Xe gases by taking the charge distributions as a function of the energy and scattering angle at 1^{o}, 2^{o}, and 3^{o}. They estimated the experimental errors at between ±15% and ±20% on both of the results.

Unpublished experiments by Brackmann and Fite[3] determined the electron loss and capture cross-sections σ_{12} and σ_{10} for N_1^+ (30 keV - 1400 keV) ions in Ne, N_2, O_2, and Ar gases. In their report, there are no details of checks on small angle scattering, and no estimation of experimental uncertainties.

Early measurements by Flaks and Solov'ev[6] were carried out to determine the cross-sections σ_{21}, σ_{20}, $(\sigma_{21} + \sigma_{20})$ for the collisions of the doubly charged ions Ne^{++}, Ar^{++}, Kr^{++}, and Xe^{++} with their own and other inert gases in the ion energy range from 6 keV to 60 keV, whereas Islam et al.[29] measured the cross-sections $(\sigma_{21} + \sigma_{20})$ for these ions in their own gases at the ion energy range between 7 keV and 90 keV. Recently, Klinger et al.[8] investigated the electron capture processes of multiply charged argon ions in argon gas at ion energies between 10 keV and 90 keV. These three experiments contain no estimate of the small angle scattering of the ions. They estimated the errors as ±15% in the first two sets and ±30% in the last set.

Even though experimental uncertainties of around ±20% were quoted in the above original references, considerably larger errors are clearly evident in the disagreement between different laboratories[3,4,5] for the electron loss cross-sections σ_{12} for N_1^+ ions in the ion energy range from 500 keV to 1400 keV, and between the data[6,7,8] for the electron capture cross-sections σ_{21} of Ar^{++} ions in the ion energy range from 10 keV to 60 keV. In the collisions of N_1^+ ions on Ne or Ar gas, the cross-section σ_{12} values of Brackmann and Fite[3] disagree systematically by 50% with the results of Pivovar et al.[4] above 350 keV where the two sets of data overlap, and the results of Dimitriev et al.[5] above 500 keV, lie somewhere between the other sets of measurements. In the σ_{21} values for Ar^{++} ions in Ne and Ar gases, the results of Flaks and Solov'ev are somewhat larger than those of Fedorenko[7], and are smaller by a factor of about two than those of Klinger et al.[8] in the case of the $Ar^{++} \rightarrow Ar$ collisions where the ion energy ranges from 10 keV to 60 keV.

Most of these electron loss and capture cross-sections σ_{12} and σ_{21}[3-8] were not compared in detail with theories such as those mentioned in the previous section. However, Dimitriev et al[5] discussed the electron loss cross-sections in terms of the velocity in Massey's adiabatic hypothesis[11] and of the atomic number of the gaseous medium, and suggested a strong influence of the polarization of gaseous atoms. Flaks and Solov'ev[6] and Islam et al.[29] discussed the experimental results of the $(\sigma_{21} + \sigma_{20})$ measurements in terms of a quantum theory by Fetisov and Firsov[30].

The cross-sections σ_{12} for N_1^+ ions in Ne and Ar gases measured by Brackmann and Fite[3] can be directly compared with the present results, whereas the other data mentioned above can only be compared with the present data by extrapolation.

CHAPTER III EXPERIMENTAL ARRANGEMENT AND APPARATUS

III-1 General Assembly

The apparatus in this laboratory was designed primarily for charge-changing differential cross-section measurements on atomic collisions, so that the direction, energy and ion species of the projectile beam could be accurately determined, and the direction and energy of the scattered ions which were allowed to reach the detector could be also well defined. A plan of the laboratory room and a general schematic view of the apparatus are shown in figs. 3-1 and 3-2, respectively.

The 150 kV accelerator (Model 150-1H, Texas Nuclear Corporation, Austin, Texas) used in this experiment had been primarily designed and used for the production of intense neutron fluxes. The ion source is a radio-frequency ion source whose frequency was about 25 MHz. The only modification made to the original neutron generator was a replacement of the palladium leak with a thermal mechanical leak (Ortec Model 341). The unmodified rf ion source was found to give good beams of several different charge states of the common gases.

The mass-energy selection of the desired projectile beam was made with a double focussing and 90° deflection-66 cm(=26") radius magnetic analyzer (High Voltage Engineer Corporation, Model 90-26). The object and image slits for this magnetic analyzer were both set to be approximately 0.05 cm width which gives a momentum resolution of

<u>Fig.3-1</u>

Plan of atomic collisions laboratory of University of Ottawa. The labelled components are identified as follows: D=2", 4" or 6" diffusion pump; S=Steering magnet; Q=2" Quadrupole doublet; F=Faraday cup and Viewer; H=#-type slit; I=4" ion pump; R= Rotary pump; V=2" or 4" valve; P_a=150 kV accelerator high voltage power supply; P_m=90° magnet power supply.

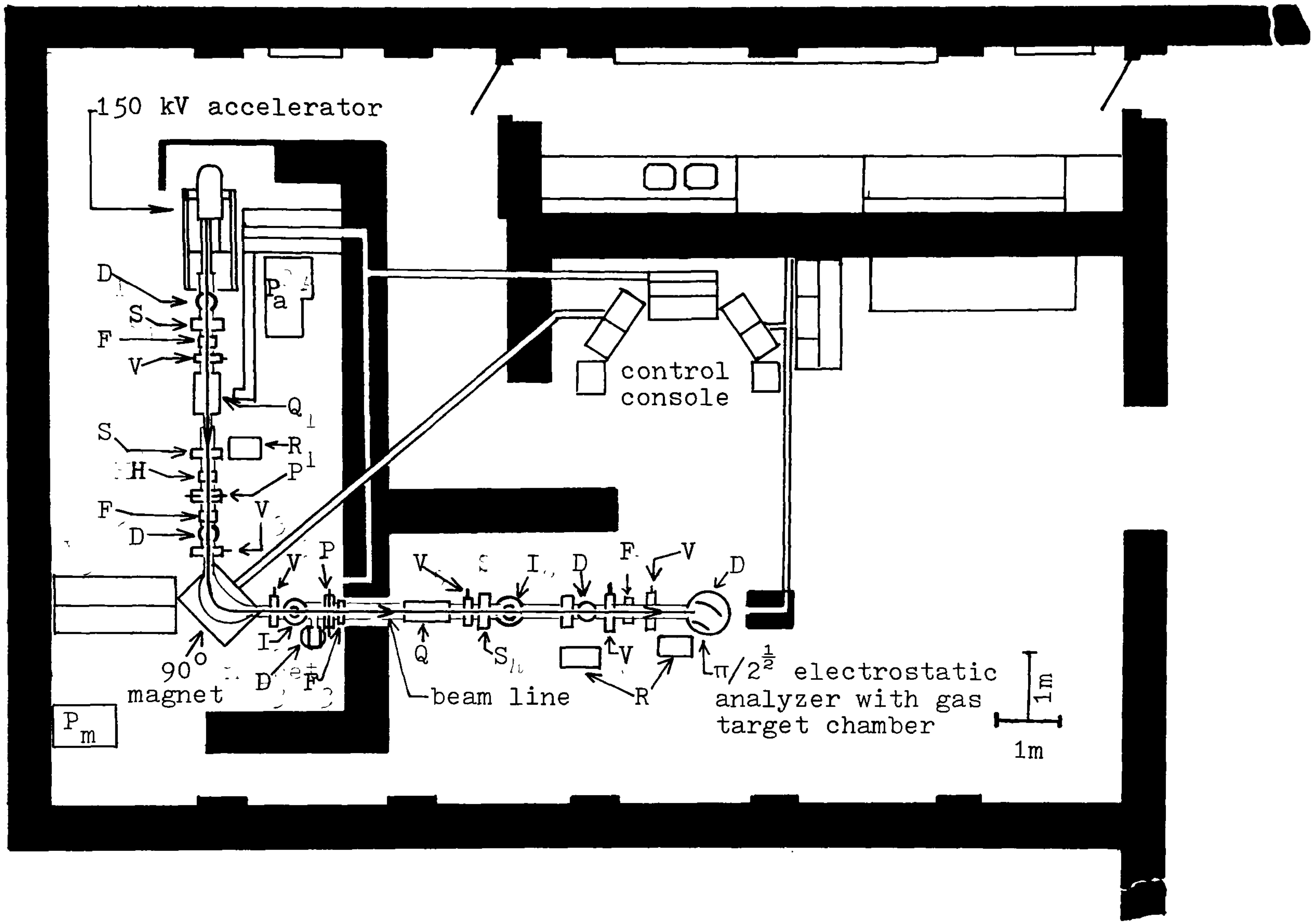

Fig.3-2 Schematic diagram of the accelerator and the apparatus which accurately define the incident and the scattered beams both in energy and direction. All the beam focussing and antisattering devices which do not alter the beam emittance have been omitted.

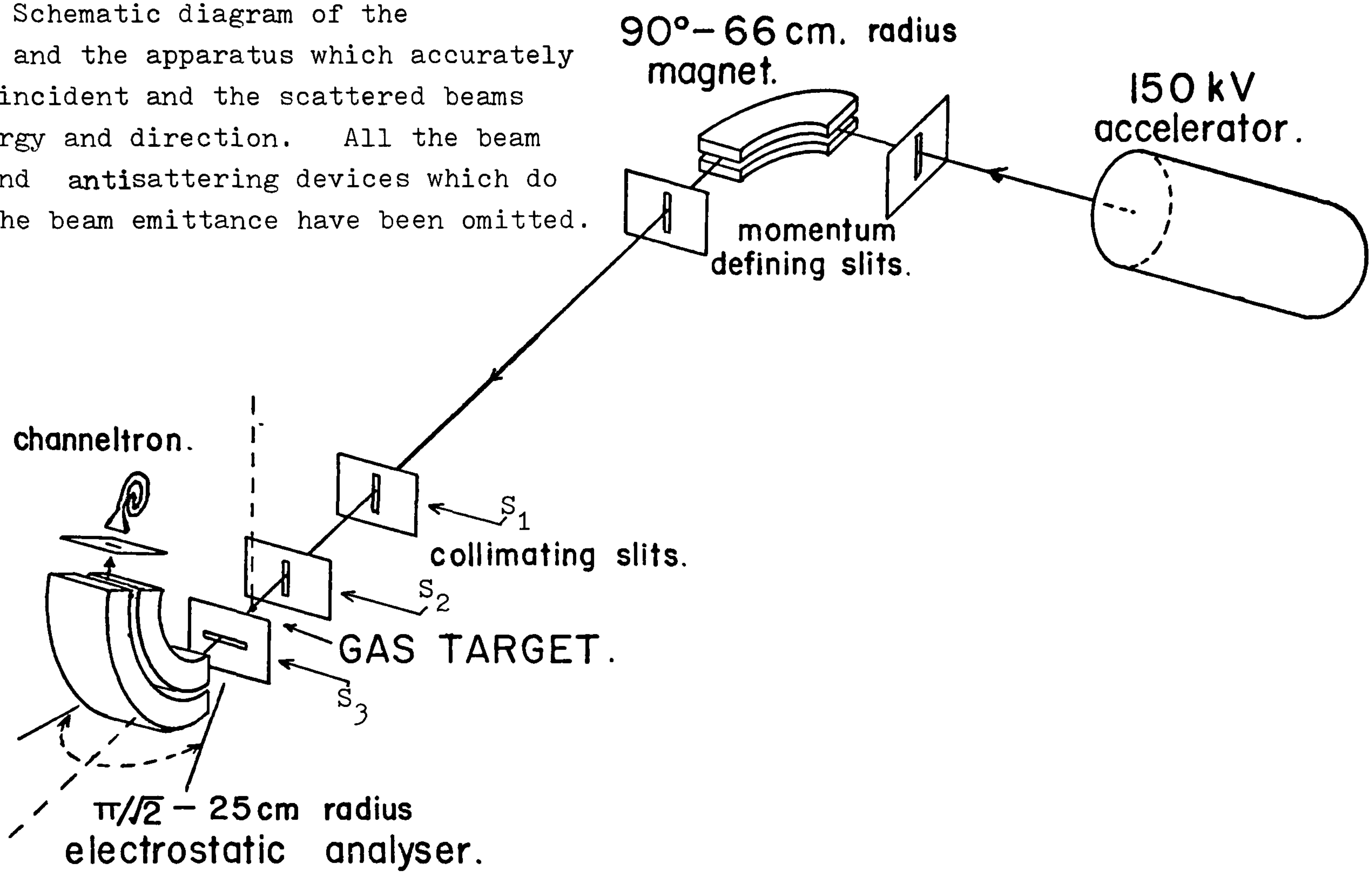

$\delta p/p = 8 \times 10^{-4}$ in this experiment . The current of the magnet power supply was stabilized to a few parts in 10^5 over several hours. In order to provide a final focus on to a collimator consisting of two slits just in front of the target chamber, the beam was focussed and steered by means of two 5 cm (=2") quadrupole doublets and several steering magnets. One quadrupole doublet focussed the beam from the accelerator on to the object slit of the 90° magnetic analyzer. The other focussed the beam from the 90° magnetic analyzer on to the collimator in front of the target chamber. Each slit at the position shown in Fig. 3-1 was provided with a movable Faraday-cup and a quartz viewer for preliminary beam adjustment.

Emerging from the collimator, a portion of the ions which traversed the target, passed through the exit slit of the target chamber, and entered a $\pi/2^{\frac{1}{2}}$ cylindrical electrostatic analyzer where they were deflected in an upward direction. The target chamber and the electrostatic analyzer are described in detail of the following section (III-2). In this experiment, all the charged particles emerging from the image-exit slit of the electrostatic analyzer were detected with a channeltron (=channel electron multiplier) as a particle detector[2] located immediately after the exit slit. The signals from the detector were observed by means of a pulse counting system which is described in section III-3 of this chapter.

A pressure of about 1×10^{-7} Torr was maintained in most of the about 10 meters of the beam line with two ion pumps and four diffusion pumps. The pressure was about 3×10^{-6} Torr at the exit to the accelerator when it was operating. The accelerator was located at a distance 5 meters from the 90° magnetic analyzer. A pressure in the electrostatic analyzer with a diffusion pump system was about 8 x 10^{-7} Torr with gas in the target chamber. As described in section III-5 of this chapter, the gas pressure within the target chamber was measured with a capacitance manometer and was controlled by a thermal mechanical leak.

III-2 A $\pi/2^{\frac{1}{2}}$ Electrostatic Analyzer with Gas Target Chamber

A Theoretical Considerations

Since Hughes and Rojansky[31] first found that a radial direction focussing occurs after $\pi/2^{\frac{1}{2}}$ rad. (127°17') in a cylindrical electrostatic field, the focussing properties of many different configurations of analyzers for the deflection and analysis of charged particles have been investigated both theoretically and experimentally by others[32-34]. An electrostatic field plotted in plane polar coordinates: radius r and azimuth θ, any radial dependence of the field has been described as a function of r^k where k is the so-called field index.

The electrostatic field under consideration is assumed to have rotational symmetry with respect to the axial z axis and reflection symmetry with respect to the x-y plane at z = 0. The radial field strength E_r (r, z = 0) is given within an annular region near the x-y plane at z = 0, which is expressed as

$$E_r(r,\ z = 0) \quad = \quad E_o\ (r/r_o)^k$$

$$= \quad E_o\ [\ 1 + kg + \frac{k(k-1)}{2!} g^2$$

$$+ \quad \frac{k(k-1)(k-2)}{3!} g^3 + \ldots$$

$$+ \quad \frac{k!}{(k-n)!\ \ n!} g^n + \ \ \ldots.\ ] \tag{3-1}$$

where $E_o(r_o,\ z = 0)$ is a given radial electrostatic field strength on the optic axis $r = r_o$ and $z = 0$, k is the field index, and $g = (r - r_o)/r_o$ $<< 1$ represents the fractional deviation of r from the mean value r_o. The potential $P(r,\ z)$ at r can be expressed in the form

$$P(r,\ z) \quad = \quad \sum_{u}^{\infty} p_u(r) \quad z^{2u} \tag{3-2}$$

where $u = 0,\ 1,\ 2,\ \ldots.$, and $P(r,\ z = 0) = p_o(r)$. Using eqs. (3-1) and (3-2), the explicit formulae of the potential and field within the annular spatial region in the vicinity can be obtained to the appropriate orders in g and h, using div $E = 0$.

$$P(r,\ z) \quad = \quad -E_o\ r_o\ [g + \tfrac{1}{2}k_1 g^2 \quad - \quad \tfrac{1}{2}(1 + k_1)h^2] \tag{3-3}$$

$$E_r(r,\ z) \quad = \quad E_o\ [1 + k_1 g + k_2 g^2 + \tfrac{1}{2}(1 - k_1 - 2k_2)h^2] \tag{3-4}$$

$$E_z(r,\ z) \quad = \quad E_o\ \ [-\ \ (1 + k_1)h + \ \ (1 - k_1 - 2k_2)\ gh] \tag{3-5}$$

for $g << 1$ and $h = z/r_o << 1$, where $k_1 = k$, $k_2 = k(k - 1)/2!$, $k_2 = k(k - 1)(k - 2)/3!$.

One considers that an ion of electronic charge e, mass m and velocity v moves along from the object space, and through a sector-shaped electrostatic field space, and finally to the image space as shown in Fig. 3-3. It is assumed that there is an electrostatic field represented by the two components given by eqs. (3-4) and (3-5). We denote m_o and v_o as the mass and velocity of the ion which enters perpendicular to the field boundary at r_o, $\theta = 0$, and $z = 0$ in the object space, and moves along the optic axis, and finally exits at the field boundary at r_o, $\theta = \phi$, and $z = 0$ in the image space. The mass m and velocity v in the trajectory shown in Fig. 3-3 are defined as

$$m = m_o\ (1 + \beta); \qquad \beta \ll 1 \tag{3-6}$$

$$v = v_o\ (1 + \gamma); \qquad \gamma \ll 1 \tag{3-7}$$

where β and γ represent the fractional deviations from the mass m_o and velocity v_o, respectively. The equation of non-relativistic motion of the ion in cylindrical coordinates (r, θ, z) are given by

$$m\left[d^2r/dt^2 - r(d\theta/dt)^2\right] = e\ E_r(r,\ z = 0) \tag{3-8}$$

$$\frac{m}{r}\frac{d}{dt}(r^2\ d\theta/dt) = 0 \tag{3-9}$$

$$m(d^2z/dt^2) = e\ E_z(r,\ z = 0) \tag{3-10}$$

These equations of motion immediately give two differential equations involving the time rate variation of r and θ. Since eq. (3-9) involving θ can easily be integrated to

$$d\theta/dt = C/r^2 \tag{3-11}$$

where C is a constant of integration; and since

$$\frac{d^2i}{dt^2} = \left(\frac{d\theta}{dt}\right)^2 \frac{d^2i}{d\theta^2} + \left(\frac{di}{d\theta}\right)^2 \frac{d\theta}{dt}\ \frac{d}{di}\ \left(\frac{d\theta}{dt}\right) \tag{3-12}$$

where i is r or z, it is possible to eliminate the time variable and obtain the differential equation for r as a function of θ. The dependent variable g $\ll 1$ will be a function of its value at entry into the field area, of β and γ, and of the entrance angle α_r in the following derivations. We assume that the entrance angle α_r is an order magnitude larger than the fractional deviations β and γ, and that g and $dg/d\theta$ are proportional to α_r so that the cubic and higher order terms in g and $dg/d\theta$ can be neglected. The squares and cross products of β and γ will be neglected.

From eq. (3-11), the constant C and therefore $d\theta/dt$ in general can be evaluated in terms of the angular velocity possessed by the particle at the time of entry on the median plane into the field region, $\theta = z = 0$. Then, a differential equation for g as a function of θ can be obtained from eq. (3-12):

$$d^2g/d\theta^2 + k_r^2(g - j) = 2(dg/d\theta)^2 - \tfrac{1}{2}k_r^2(k_r^2 + 1)g^2 - k_r^2g_1^2 - \alpha_r^2 \tag{3-13}$$

where

$$k_r = (k + 3)^{\frac{1}{2}} \tag{3-14}$$

$$j = (2\gamma + \beta)/(k + 3) \tag{3-15}$$

Here, the subscript 1 denotes initial values at $\theta = z = 0$. Similarly, the differential equation for h as a function of θ can easily be obtained from eq. (3-10).

$$d^2h/d\theta^2 + k_z^2h = 0 \tag{3-16}$$

where

$$k_z = [- (k + 1)]^{\frac{1}{2}} \tag{3-17}$$

Fig.3-3

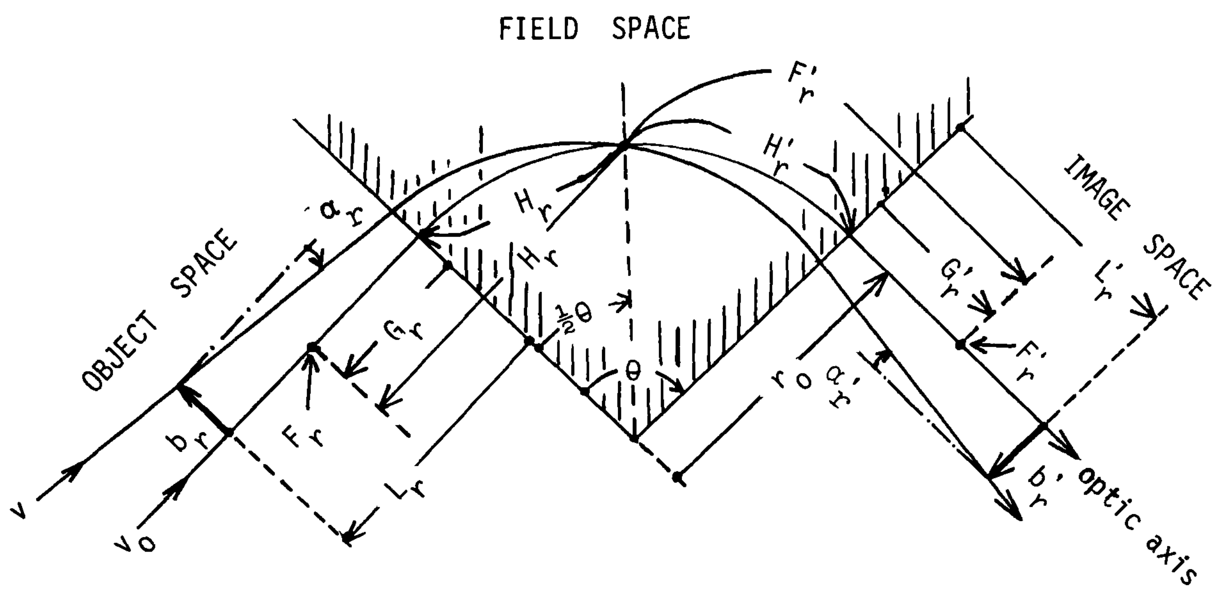

(a). Radial motion

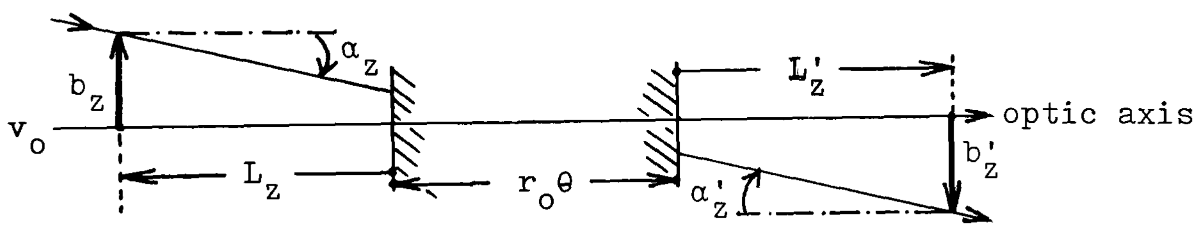

(b). Axial motion

Diagram showing path of a charged particle through a sector shaped electrostatic lens. Particle is shown leaving object space at a distance b from optic axis a and at a diverging angle α.

k_i (i = r or z) is a characteristic parameter of the field, representing the lens action in the i direction, and the angle of the half period is given by $\phi_{1/2} = \pi/k_i$. j is a factor representing the chromatic dispersion with respect to β and γ. Equation (3-16) shows that there is no chromatic dispersion in the z-direction.

Exact solutions to the types of eq. (3-16) can easily be obtained, whereas those to the types of eq. (3-13) are not known. To find the required second-order solution to eq. (3-13), we replace the g^2 and $(\frac{dg}{d\theta})^2$ in the second-order terms on the right by the square of the first order solution for g and its derivative. The result of the approximate second-order solution at θ and z = 0 is given by

$$
\begin{aligned}
g = & -\alpha_r \left[k_r^{-1} \sin(k_r\theta) + (L_r/r_o) \cos(k_r\theta)\right] + j \left[1 - \cos(k_r\theta)\right] \\
& + (b_r/r_o) \cos(k_r\theta) + \alpha_r^2\{ - (k_r^2 + 2)L_r \sin(k_r\theta)/(3r_o k_r) \\
& + \left[(k_r^2 + 2)/(3k_r^2) + (k_r^2 - 1)L_r^2/(6r_o^2)\right] \cos(k_r\theta) \\
& + (k_r^2 + 5)L_r \sin(2k_r\theta)/(6k_r r_o) - \frac{1}{12}(k_r^2 + 5)(k_r^{-2} - L_r^2/r_o^2)\cos(2k_r\theta) \\
& - \tfrac{1}{4}(k_r^2 + 1)(k_r^{-2} + L_r^2/r_o) \}
\end{aligned}
\tag{3-18}
$$

where b_r and L_r are the object and its distance. The solution to eq. (3-23) for the axial motion is obtained in a similar way

$$
h = -\alpha_z\left[k_z^{-1} \sin(k_z\theta) + (L_z/r_o)\cos(k_z\theta)\right] + (b_z/r_o)\cos(k_z\theta) \tag{3-19}
$$

In the region beyond the field in the image space for the given coordinates, b'_r, L'_r and α'_r as shown in fig. 3-3, an equation of the radial motion for the particle can be now written as

$$\begin{aligned} b'_r &= r_o g' + L'_r \tan \alpha'_r \\ &= r_o g' + L'_r (1 - g')(dg'/d\theta) \end{aligned} \tag{3-20}$$

where g' is the value of g at $\theta = \emptyset$ and $z = 0$. Substituting eq. (3-18) in which we set $\theta = \emptyset$ into eq. (3-19) to obtain g' and then developing the optical parameters and their interrelationship, all the analogues to an optical lens can be obtained as summarized in the following table. All the quantities are illustrated in fig. 3-3, and the unprimed and single primed symboles refer to the values in the object and image regions, respectively:

Focal length: $F_i = F'_i = r_o / [k_i \sin(k_i \emptyset)]$ (3-21)

Distance of the focus from the edge: $G_i = G'_i [r_o \cot(k_i \emptyset)]/k_i$ (3-22)

Distance of $\frac{1}{2}\emptyset$ trajectory in the field space:

$$H_i = H'_i = [-r_o \tan(\tfrac{1}{2} k_i \emptyset)]/k_i \tag{3-23}$$

Newton's equations: $(L_i - G_i)(L'_i - G_i) = F_i^2$ (3-24a)

$$(L_i - H_i)^{-1} + (L'_i - H_i)^{-1} = F_i^{-1} \tag{3-24b}$$

Magnification of the image: $M_i = (L'_i - G_i)/F_i = F_i/(L_i - G_i)$ (3-25)

Dispersion due to the mass and/or velocity difference:

$$D_i = r_o j(1 + M_i) \tag{3-26}$$

Relation between the object and image:

$$b'_r = r_o(1 + M_r)\, j - b_r M_r \tag{3-27}$$

$$b'_z = - b_z M_z \tag{3-28}$$

Focussing angle: $\alpha'_r = \alpha_r/M_r - b_r/F_r + r_o j/F_r$ (3-29)

$$\alpha_z' = \alpha_z/M_z - b_z/F_z \tag{3-30}$$

where i = r or z. The equations (3-21) to (3-30) are the general expressions for the first-order angular aberration in the sector-shaped analyzer.

When the particle mass is m_o so that $\beta = 0$ in eq. (3-6), the energy resolution in first-order approximation is given by

$$\frac{\delta W}{W_o(v_o)} = \frac{W(v) - W_o(v_o)}{W_o(v_o)} = 2\gamma \tag{3-31}$$

which gives, using eq. (3-15), the energy resolution for the radial motion

$$\delta W/W_o = k_r^2 \; j_{\beta=0} \tag{3-32}$$

where, for the second-order angular aberration in the case of $\phi = n\pi/k_r$ (n = an odd integer) and $M_r = 1$,

$$j_{\beta=0} = (b_r' + b_r)(2r_o)^{-1} + \alpha_r^2(6k_r^2)^{-1}\left[2(k_r^2 + 2) + 3(k_r^2 + 1)\right.$$
$$\left.(k_r L_r/r_o)^2\right] \tag{3-33}$$

Since the factors k_r and k_z respectively in eqs. (3-14) and (3-17) must have real values, the field index k must have a value between -1 and -3. When the lens action factor k_z is zero, the field index k = -1 is obtained from eq. (3-17) and therefore $k_r = 2^{\frac{1}{2}}$ from eq. (3-14). A sector-shaped electrostatic field with k = -1 focusses the charged particles only in the radial direction of the motion. For equivalently focussing in both the radial and axial directions of the motion, it is necessary that the radial focal length is the same as the axial focal length, i.e., $F_r = F_z$ given in eq. (3-21), so that the field index for the double focussing is given by k = -2 and therefore $k_r = k_z = 1$.

We consider the focussing properties when the particle energy varies with the scattering angle θ_s due to the kinematics of atomic collisions and scattering as shown in fig. 3-4 were the plane of the entrance angle α_r is assumed to be the same as the scattering plane. To simplify the analysis, it is assumed that the projectile mass m_p is equal to the target mass m_t, so that the laboratory energy W_o of the scattered particle moving along the optic axis of the electrostatic analyzer is given in terms of the incident projectile energy W_p by $W_o/W_p = \cos^2\theta$. For two other orbits which deviate from perpendicular entrance into the field by angles α_r^+ and α_r^-, respectively, the fractional energy deviations from the mean energy W_o are given in the form by using eq. (3-32)

$$j^{\pm}_{\beta=0} = \frac{\cos^2(\theta_s \mp \alpha_r^{\pm}) - \cos^2\theta_s}{\cos^2\theta_s} \tag{3-34}$$

By taking into account of the first-order angular aberration in eq. (3-18), the orbital equations of the radial motion in the electrostatic analyzer are given as

$$g^{\pm} = \mp\alpha_r^{\pm} k_r^{-1} \sin(k_r\emptyset) + \frac{\cos^2(\theta_s \mp \alpha_r^{\pm}) - \cos^2\theta_s}{\cos^2\theta_s} \tag{3-35}$$

where it is assumed that $L_r = b_r = 0$. The focussing condition of $g^+ = g^-$ in eq. (3-35) provides a relation in the form

$$\tfrac{1}{2} k_r \cot(k_r\emptyset) = -\tan\theta_s \tag{3-36}$$

Fig.3-4

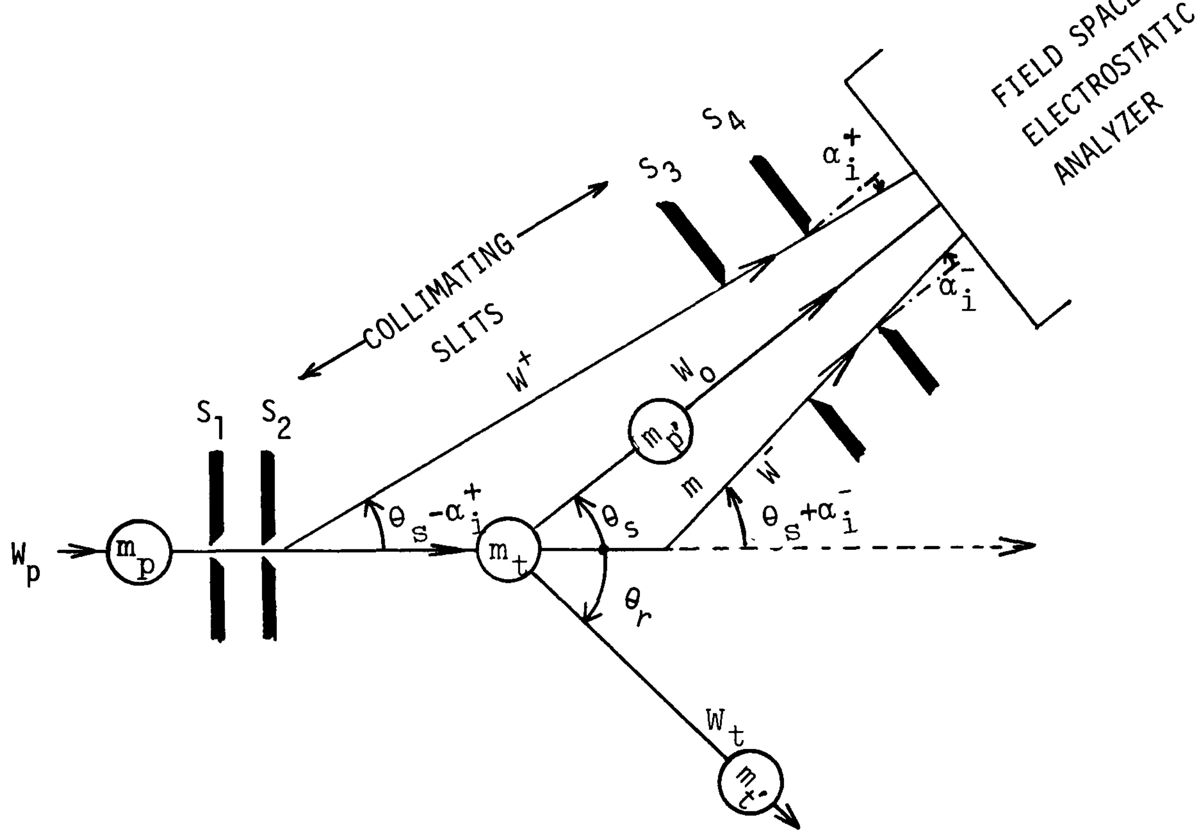

Schematic diagram of kinematics of atomic collisions and scattering into an electrostatic analyzer. All particle trajectories are assumed to consist of linear lines in laboratory system. The impinging incident particle with energy W_p and mass m_p is moving towards the gas target particle with mass m_t initially at rest. The particle with energy W_o, mass m_p, and scattering angle θ_s is scattered into the electrostatic analyzer after collision, where the particle with energy W_t and mass m_t recoils out at an angle θ_r. To simplify the analysis, it is assumed that $m_p=m_{p'}=m_t=m_{t'}$, and the Q value is very small; $Q<<W_p$, so that

$$W_o \simeq W_p \cos^2 \theta_s$$

for the small values of $\alpha_r^+ = \alpha_r^-$. Connecting in eq. (3-36) with the focussing properties, it is noted that for a given field index $k = k_r^2 - 3$ the deflection angle ϕ of a sector-shaped electrostatic analyzer should vary with the scattering angle θ_s, or, for a given deflection angle ϕ the field index k should vary with the scattering angle θ_s to satisfy the focussing condition. Here, the variation of the field index implies the simultaneous variation of both the factors k_r and k_z at the same time since $k_r = (2 - k_z^2)^{1/2}$ from eqs. (3-14) and (3-17). In order to keep the constant angular resolution for differential cross-section measurements, the field index $k = -1$ ($k_r = 2^{1/2}$ and $k_z = 0$) was chosen, corresponding to the condition for no axial focussing: the plane of the entrance angle α_z is to be the same as the scattering plane.

Using the equations from eq. (3-21) to (3-25), the deflection angle ϕ for given values of the magnification $M_r = 1$ and factors $k_r = 2^{1/2}$ and $k_z = 0$ is obtained in the form

$$\phi = 2^{-1/2} \cos^{-1} \left\{ \frac{1 - \frac{1}{2}(r_o/L_r)^2}{1 + \frac{1}{2}(r_o/L_r)^2} \right\} \tag{3-37}$$

where the object distance L_r between the object and the entrance field boundary is assumed to be the same as the image distance L_r' between the image and the exit field boundary. Equation (3-37) gives a deflection angle of $\phi = \pi/2^{1/2}$ radians when $L_r = 0$.

The idealized $\phi = \pi/2^{1/2}$ and $k = -1$ electric field distribution is assumed throughout the charge free space between an inner cylinder of radius r_a and an outer cylinder of radius r_b. The potential of the inner cylinder is V_a, while the potential of the outer cylinder is V_b. It is assumed that the cylinders are sufficiently long and wide to neglect the end effects of the electrodes, so that the poten-tails are independent of both θ and z in the cylindrical coordinates (r, θ, z). For the symmetrical potentials of $|+V_b| = |-V_a|$ on the two cylindrical walls, the mean potential V_o can be found to be zero at the electrical mean value of the radius r_o given by

$$r_o = (r_a r_b)^{\frac{1}{2}} \tag{3-38}$$

and the radial field strength $E_o(r_o, z = 0)$ is then given by

$$E_o(r_o) = \frac{\delta V}{\ln(r_b/r_a)} \frac{1}{r_o} \tag{3-39}$$

where $\delta V = V_b - V_a$. Denoting $W_o(r_o, z = 0)$ as the mean energy possessed by a particle which moves along the optic axis concentric with the cylindrical walls, an equation for this energy is given by

$$W_o = ne\ \delta V \ /[2 \ln(r_b/r_a)] \tag{3-40}$$

where n is the ionization degree of the particle, and e is the electronic charge. Denoting $\delta r = r_b - r_a$ as the electrode spacing, the ratio $\delta r/r$ for finding the design parameters is expressed:

$$\frac{\delta r}{r_o} = \left\{ \frac{r_b}{r_a} + \frac{r_a}{r_b} - 2 \right\}^{\frac{1}{2}} \tag{3-41}$$

Setting $M_r = 1$ and $k_r = 2^{\frac{1}{2}}$, eq. (3-32) substituted by eq. (3-38) gives an energy resolution for a $\emptyset = \ /2^{\frac{1}{2}}$ electrostatic analyzer:

$$(\delta W/W_o)_{FWHM} = (b_r + b_r')/r_o + 4\alpha_r^2/3 \tag{3-42}$$

where b_r and b'_r represent the half widths of the object and image slits of the electrostatic analyzer, respectively. Eq. (3-19) shows that the axial heights of the two trajectories are the same as the object slit width: $z = b_r$, when the incident beam trajectory is parallel to the optic axis of the electrostatic analyzer with a field index $k = -1$ ($k_r = 2^{1/2}$, $k_z = 0$) so as to be $\alpha_z = 0$. Here, the electrode heights should be large enough to eliminate the field distortion due to the finite ratio z/b_z. Eqs. (3-37), (3-38), (3-40), (3-41) and (3-42) determine the design parameters of a cylindrical electrostatic analyzer.

B Design and Construction

The design was determined by:

i). a maximum deflection voltage $\delta V = 20$ kV from two identical and highly stable power supplies (FLUKE, Model 410B),

ii). the 150 kV maximum voltage on the accelerator, and

iii). an energy resolution of $(\delta W/W_o)_{FWHM} = 1 \times 10^{-4}$.

The following basic conditions were chosen for the design of the present electrostatic analyzer.

The ratio of a particle mean energy to the deflection voltage:

$$W_o(\text{eV})/\ V(\text{volts}) = 10.0368e$$

The mean radius of optic axis: $r_o = 25.39$ cm

The object and image distances: $L_i = 2.74$ cm

$$(L_r = L'_r = L_z = L'_z = L_i)$$

so that eq. (3-37) and the combined equations of (3-38), (3-40) and (3-42) give the following basic dimensions chosen for the design of the cylindrical electrodes.

The deflection angle:	$\phi = 115.00^{\circ}$
The radius of the inner electrode:	$r_a = 24.76$ cm
The radius of the outer electrode:	$r_b = 26.03$ cm
The electrode spacing:	$\delta r = r_b - r_a = 1.27$ cm
The electrode height in the axial dimension:	$z = 6.98$ cm

where the same height z for the two electrodes was chosen to be large enough to eliminate the field distortion due to the finite ratio z/b_z of the electrode height to the height b_z of the object slit, and the others were calculated by using the first-order theory. To obtain an energy resolution, $(\delta W/W_o)_{FWHM} = 1 \times 10^{-4}$, for the electrostatic analyzer itself, the full radial-widths of the object and image slits are estimated to be $2b_r = 2b_r' = 2.54 \times 10^{-3}$ mm by using eq. (3-42) with $\alpha_r << 1$. But, the present designated slit sizes for the total charge-changing cross-section measurements were made intentionally to be larger than the estimated value.

As shown in the photograph of fig. 3-5, the electrodes with tolerances of less than ±0.005% from the cylindrical shape and less than ±0.01% variation in the spacing between them were made from solid aluminum blocks, and were mounted on a thick aluminum plate. As shown in the cross-sectional view of fig. 3-6, the electrode base and cover plates were symmetrically grounded and separated by a distance 6.4 mm from the electrodes. To keep short the fringing field regions at the entrance and exit of the analyzer, the shielding aluminum plates (13A and 13B shown in fig. 3-5) with 1.5 mm and 5 mm radius holes respectively were also symmetrically grounded and separated by a distance 6.4 mm from

Fig.3-5 (A)

Photograph of $\pi/2^{\frac{1}{2}}$ deflection-25.4 cm radius electrostatic analyzer. The labelled components are identified as follows:

12A & 12 B = Aluminum electrodes having a spacing of 0.4980"

13A & 13B=Field terminators

14 = See Fig.3-6 (Stainless bolt)

15 = Aluminum electrode base plate

15A, 15B,& 15C= Supports of the electrodes mounted on the base plate(15), which is also the devices for adjusting the position of the entire electrodes in the alignment of the system from the target chamber to the electrostatic analyzer.

16 = Optical translation stage

17 = Support to the image slit

18 = A Bendix Model 4010 channeltron used in preliminary tests of the present beam transportation system. We replaced this particle detector with an Amperex Model B312BL channeltron with a 10 mm x 3 mm rectangular aperture- a closed end-output for the present cross section measurements.

19 = A short coaxial-cable connected between the channeltron in vacuum and the preamplifier just outside the vacuum box

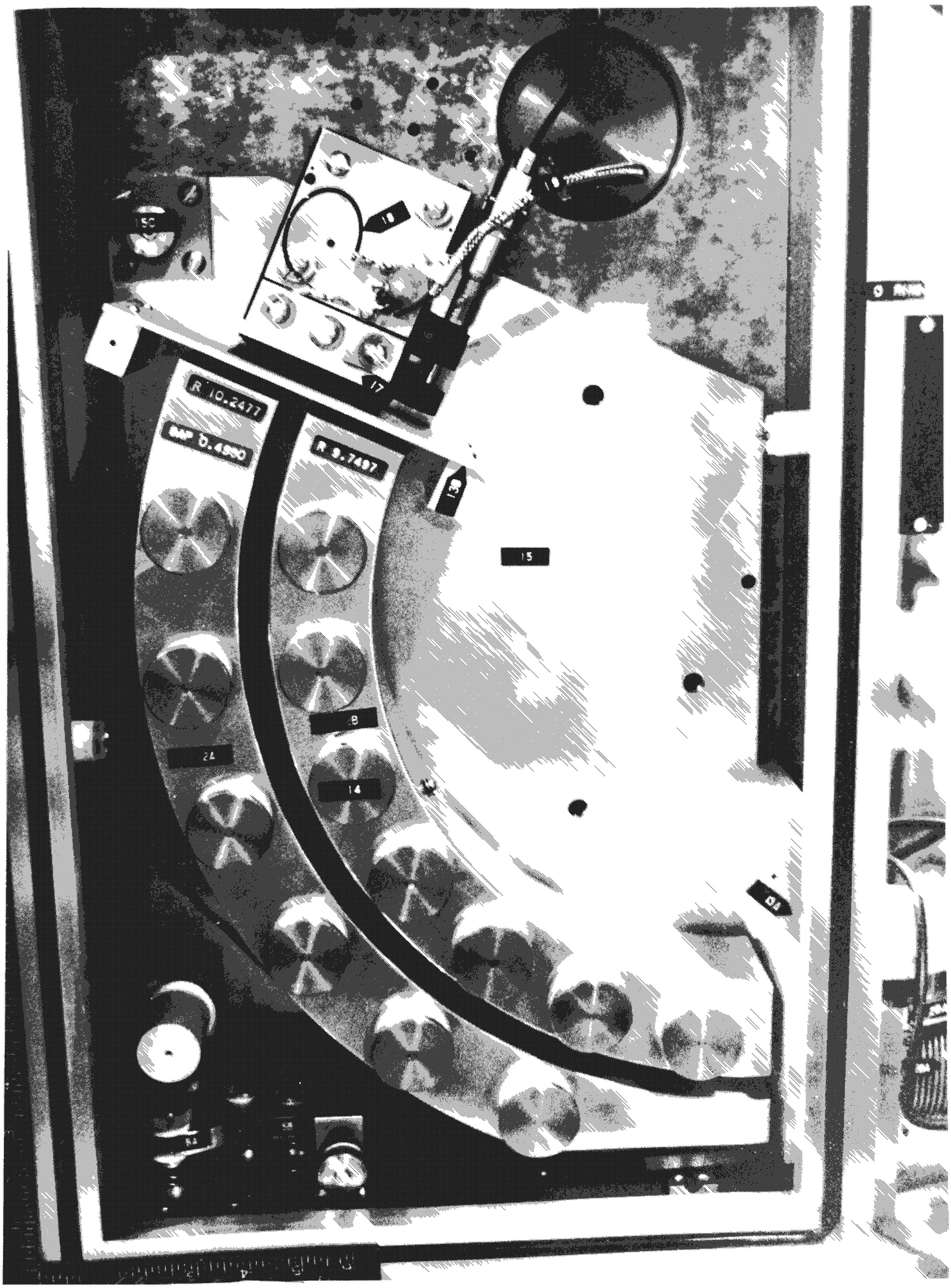
R 10.2477
R 9.7497
15
14
17

Fig.3-5(B)

Photograph of the system which consists of the target chamber and electrostatic analyzer supported on a floor mounted structure.

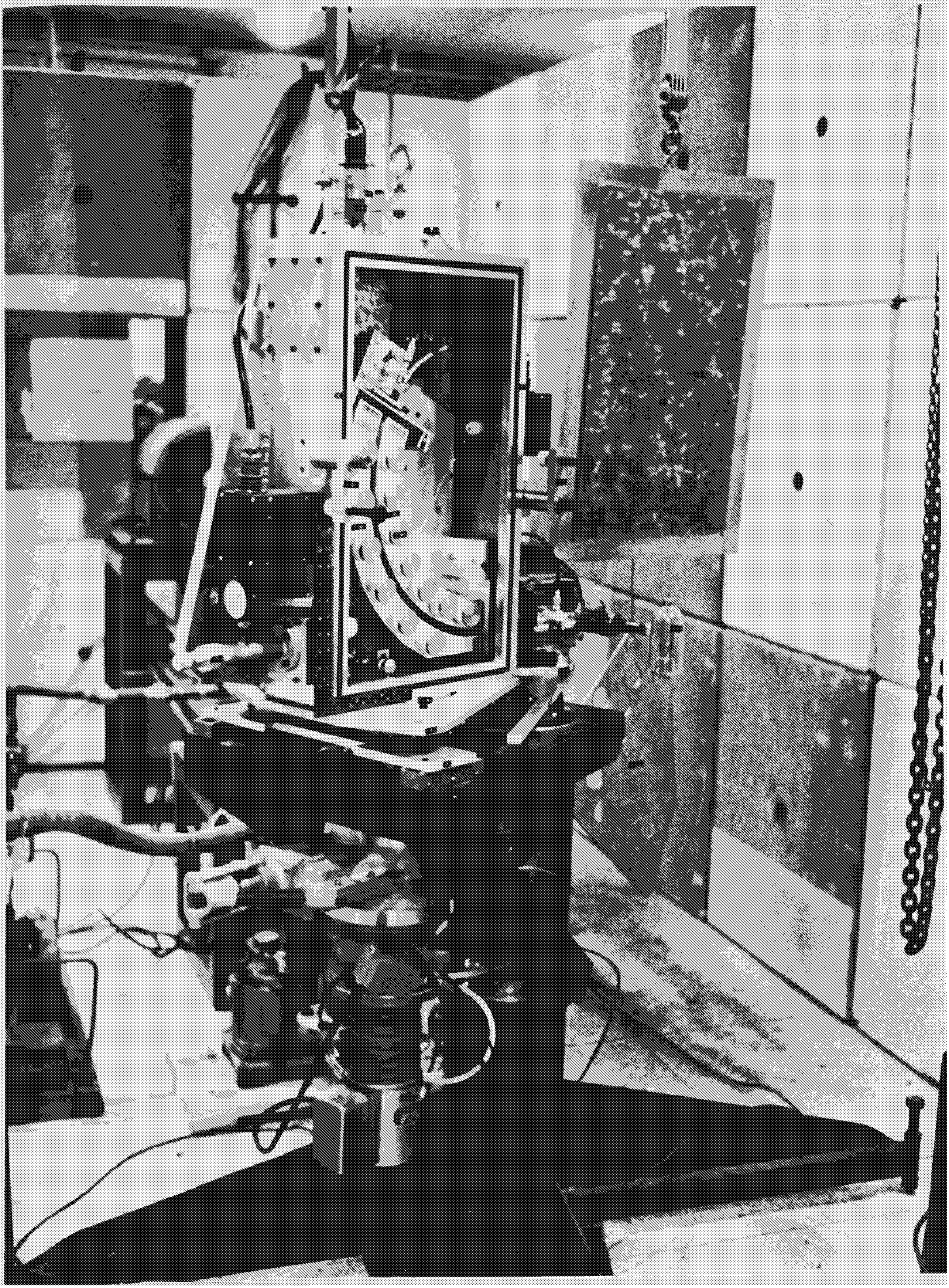

Fig.3-6

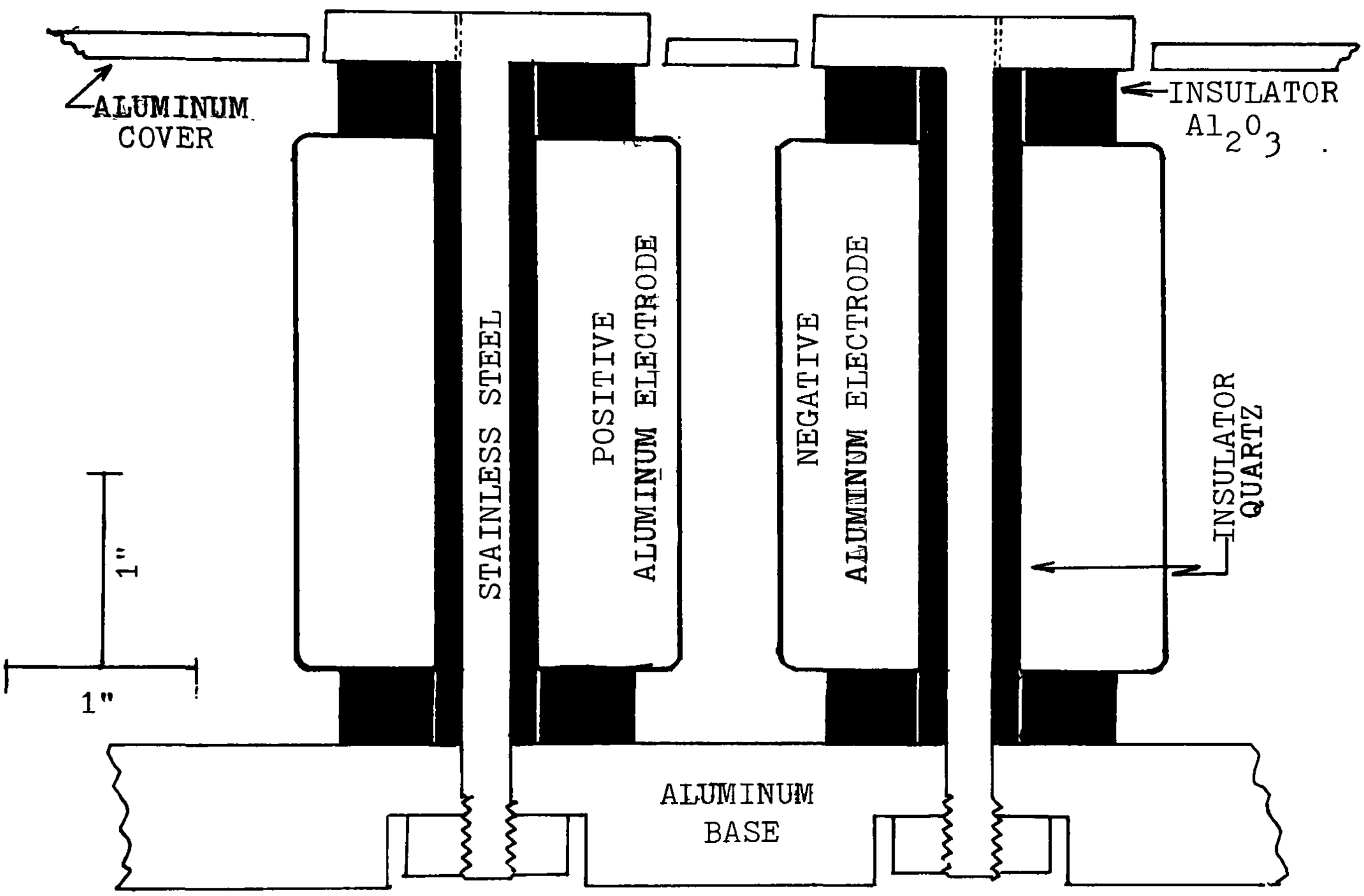

Cross sectional view of electrode mounting the entrance and exit faces of the electrodes.

The electrodes were insulated initially by using high dielectric strength and low loss alumina Al_2O_3 disks (Alsimag 753, Dielectric strength = 7.9 kV/mm) and plastic tubes (Lexan, Dielectric strength = 15.75 kV/mm), as shown in fig. 3-6. By gradually raising the inner and outer electrode voltages respectively up to -10 kV and +10 kV for a test operation of the electrostatic analyzer in a vacuum of about 10^{-6} Torr, it was found that discharges occurred in the system, which produced a surface carbon layer along the line of contact between the disk and the tube. The modification was therefore made to the initial insulation by replacing the plastic tubes with quartz tubes and by making a small hole through each of the heads of the stainless pins to evacuate the residual gas within the spaces between the insulators and the electrodes. No discharges were then found during the operation of the system with the present maximum voltages of -10 kV and +10 kV on the respective electrodes. The voltages were applied by means of high voltage coaxial cables from the two power supplies to the ceramic high-vacuum seals on the aluminum box of the analyzer and bare copper-wires from the seals to the electrodes within the vacuum box. In symmetrically charged parallel-plates, the electrostatic attractive force F on one plate of area A is given by $F = \frac{1}{2}\varepsilon E^2 A = \frac{1}{2}\varepsilon (dV/dr)^2 A$, where ε is the dielectric constant, E is the field strength, and dV/dr is the potential gradient, which is approximately equal to $\delta V/\delta r$ where δV and δr are the potential difference and the spacing, respectively, between the charged plates. For δV = 20 kV between the cylindrical plates of the present electrodes in the vacuum, the force on the one plate is estimated to be less than 2 newtons which is negligibly small compared with the strength of the mechanical mounting in the present analyzer.

The object b_r and entrance angle α_r were defined by the slit size of the present target chamber just in front of the electrostatic analyzer, as shown in fig. 3-7. In the mechanical structure of fig. 3-7, one of the two identical thick brass frames F_1 and F_2 was made to be rotated, with respect to the other, about a common axis of the accurately machined pins P_1 and P_2. The entrance C_1 and exit C_2 brass collimators were mounted in the accurately machined holes in the frames F_1 and F_2, respectively. The target chamber itself consisted of a flexible bellows connecting F_1 to F_2. The frame F_1 was connected to the end of the beam line, so that the axis of the entrance beam collimator C_1 was on the axis of the beam line from the 90^o magnetic analyzer. The other F_2 was fixed to the electrostatic analyzer box, so that the entire electrostatic analyzer with its object collimator C_2 could be rotated about the common axis of the center pins with respect to the fixed frame F_1. The collimator C_1 supported the entrance slits S_1 and S_2 which had the rectangular orifice sizes of 0.22 mm horizontal and 2.40 mm vertical width and were separated by a distance 210.0 mm, so that the incident direction of the beam was defined to ±3.6 minutes of arc in the horizontal direction. Here, the "horizontal" and "vertical" directions or widths become respectively the "axial" and "radial" field directions in the electrostatic analyzer. The second slit S_2 also acted as the rectangular orifice for the differentially pumped gas target. In the beam exit region from the gas target, the collimator C_2 supporting the two slits S_3

Fig.3-7

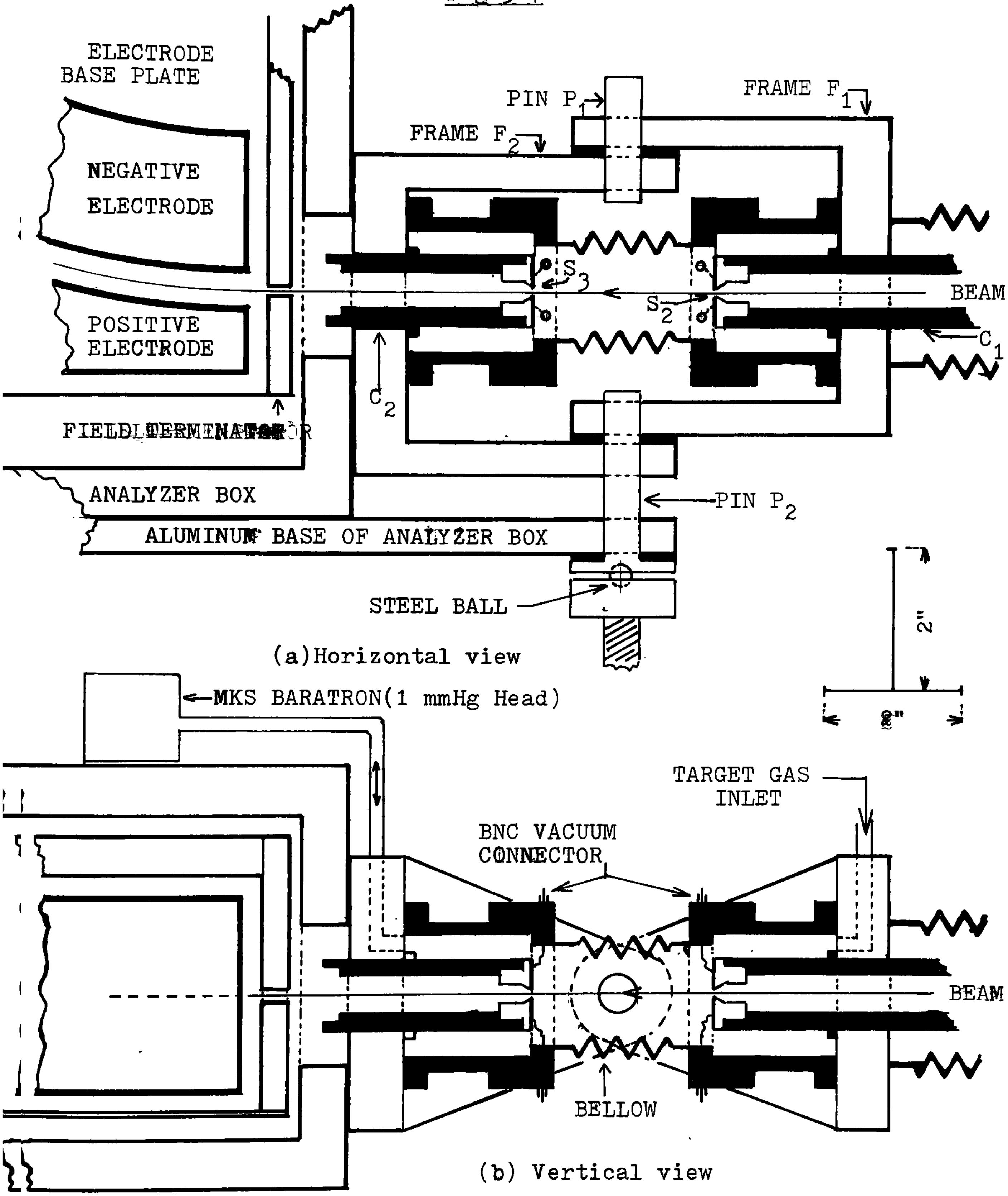

(a)Horizontal view

(b) Vertical view

Geometrical arrangement in the object region of the $\pi/2^{\frac{1}{2}}$ electrostatic analyzer with gas target chamber. The schematic diagram of the collimator C and the slit S is shown in Fig.3-8 and S_4 in the original design was made similar to the collimator C_1. The slit S_3 acted to define the beam exit aperture as well as the differentially pumped gas target. Several 9.5 mm diameter holes were made in the sides of the collimator tubes C_1 and C_2 to ensure that the pressure within each collimator between the slits was much lower than the pressure within the gas target chamber. The slit S_4 at a distance of 2.74 cm from the face of the entrance boundary of the analyzer electrodes was originally designed to be the object slit of the analyzer, but was removed to allow all the ions emerging from the exit slit S_3 of the target chamber into the analyzer during the present cross-section measurements. This was one of the design changes to increase the angle of acceptance of the ions from the chamber to the electrostatic analyzer when measuring angle integrated cross-sections instead of measuring the differential cross-sections. So, the slit S_3 of 2.40 mm horizontal and 0.06 mm vertical widths defined both the down-steam end of the gas target and the beam position and size at the object of the analyzer for the focussing properties of the analyzer.

The gas target length is defined geometrically as the distance between the slits S_2 and S_3, which measured accurately as 63.20 ± 0.005 mm in the present electron loss cross-section measurements. For the later measurements of the present electron capture cross-sections, the gas target length was reduced from 63.20 cm to 27.40 ± 0.005 mm, so that a higher gas pressure could be used without producing too many multiple collisions. The axis of rotation of the frames F_1 and F_2 passed through the mid-point of the target length.

Since the horizontal width of the slit S_3 was much greater than that of the slit S_1 or S_2, the axial (horizontal) entrance angle α_z of the beam into the analyzer was limited by the ±3.6' of arc in the horizontal (axial) direction of the beam which passed through the slits S_1 and S_2.

A micrometer depth gauge resting on the side of the electrostatic analyzer was used to measure the rotation of the analyzer about a vertical axis through the mid-point of the target length. The angle of the rotation was measured with both an accuracy and a reproducibility of $\pm 0.005^{\circ}$ with respect to the mean direction of the incident beam so as to obtain angular profiles and to permit accurate alignment of the system along the beam line up to the image region of the electrostatic analyzer. The accuracy of $\pm 0.005^{\circ}$ represents about ±0.06 mm horizontal (axial) position error in the image region of the electrostatic analyzer. In the vertical (radial) direction, the divergence of the beam which passed through the slits S_1, S_2, and S_3 was defined to be less than $\pm 0.03^{\circ}$ of arc, which is to be compared with a maximum acceptance angle fo $\pm 1.45^{\circ}$ determined by the 2.74 cm electrode spacing and 25.38 cm radius of curvature in the electrostatic analyzer having a design magnificiation $M_r = M_z = 1$, so that it limited the beam entrance angle α_r of the analyzer. In terms of the 25.39 cm mean radius of the analyzer, the angle $(\alpha_z^+ + \alpha_z^-) = 7.2'$, corresponds to an image spread of $2b_z' = 1.34$ mm at the detector entrance, which is to be compared with the 7.8 mm image slit width in the axial direction of the electrostatic field. In the radial direction, the angle $(\alpha_r^+ + \alpha_r^-) = 0.60^{\circ}$ corresponds to an image spread of $2b_r' = 0.50$ mm at the detector entrance where the end effects and the second order angular aberrations in the electrostatic analyzer are both small enough to be neglected, when compared with the 0.95 mm image slit width of the present analyzer. Any ions which passed through the slits S_1, S_2 and S_3 would therefore reach the detector without striking the electrodes. The geometrical layout of the image region of the electrostatic analyzer is explained in section III-3 of this chapter.

As shown in fig. 3-8, each of the above brass slits consisted of two semicircular thin plates mounted on machined alumina Al_2O_3 to individually insulate each side of the slit from the collimator. The slits S_1 and S_2 also acted as a Faraday cup for the horizontal setting of the incident beam direction, and the slit S_3 was used for the vertical setting. Since the vertical height of the slit S_3 was much smaller than that of the slit S_1 or S_2, some of the beam after passing through the gas target struck the slit S_3, and was integrated to normalize the counting rates of the detector mounted immediately after the image slit of the electrostatic analyzer.

During a preliminary test in which the entire electrostatic analyzer was set and optimized to the incident beam in the horizontal (axial) direction, it was found that some of the beam was reflected somewhere on the inner surface of the outer electrode of the analyzer and then reached the detector, when the deflecting voltage δV_e of the analyzer was lower by a few hundred volts than the correct voltage, as shown in the energy profile of fig. 3-9, which indicates about 2.2% voltage difference between the two voltages. This reflected beam was detected by moving the position of the image slit along the optic axis. Different deflection voltages were required as the image slit position

Fig.3-8

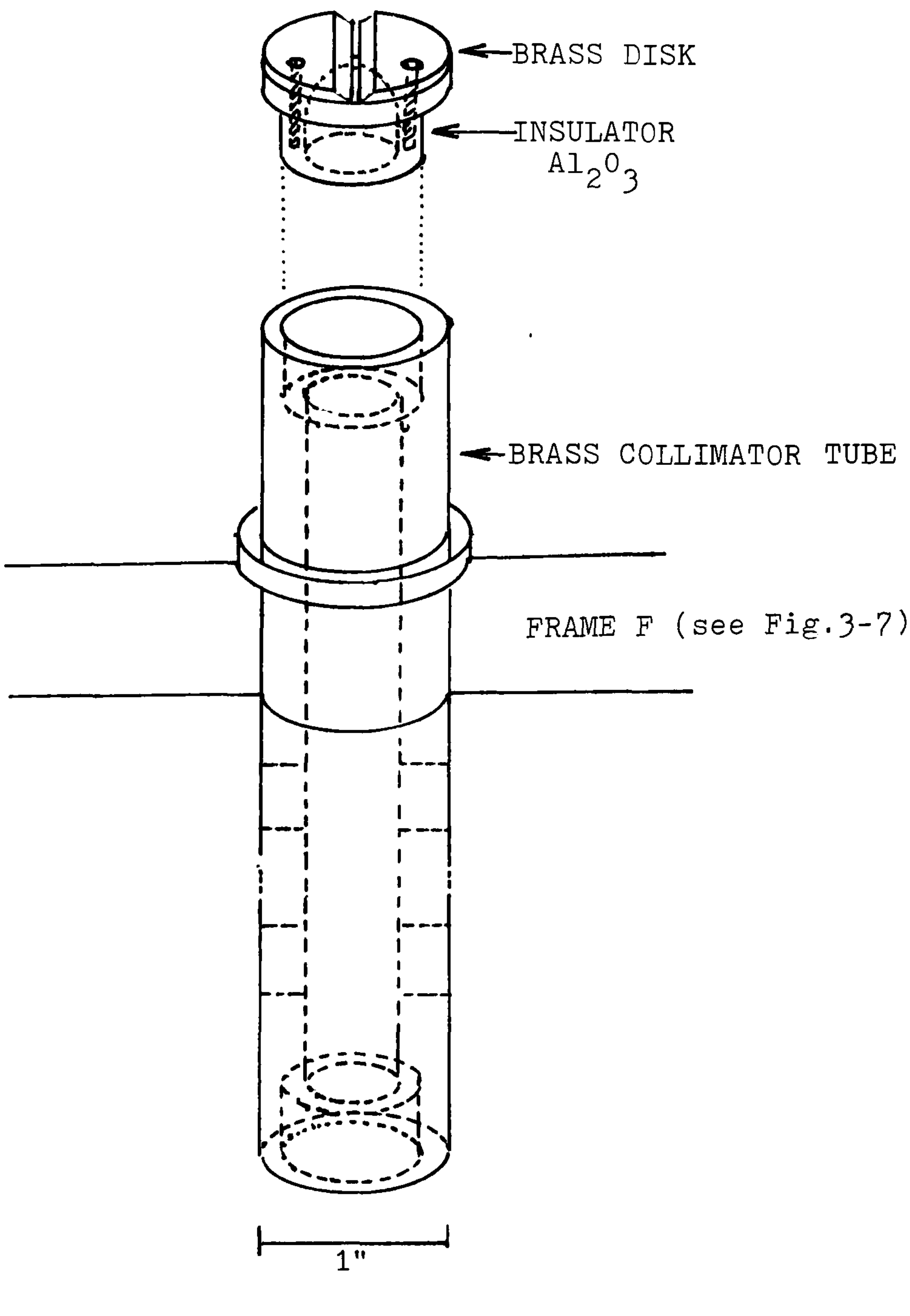

Schematic diagram of the slit and collimator system

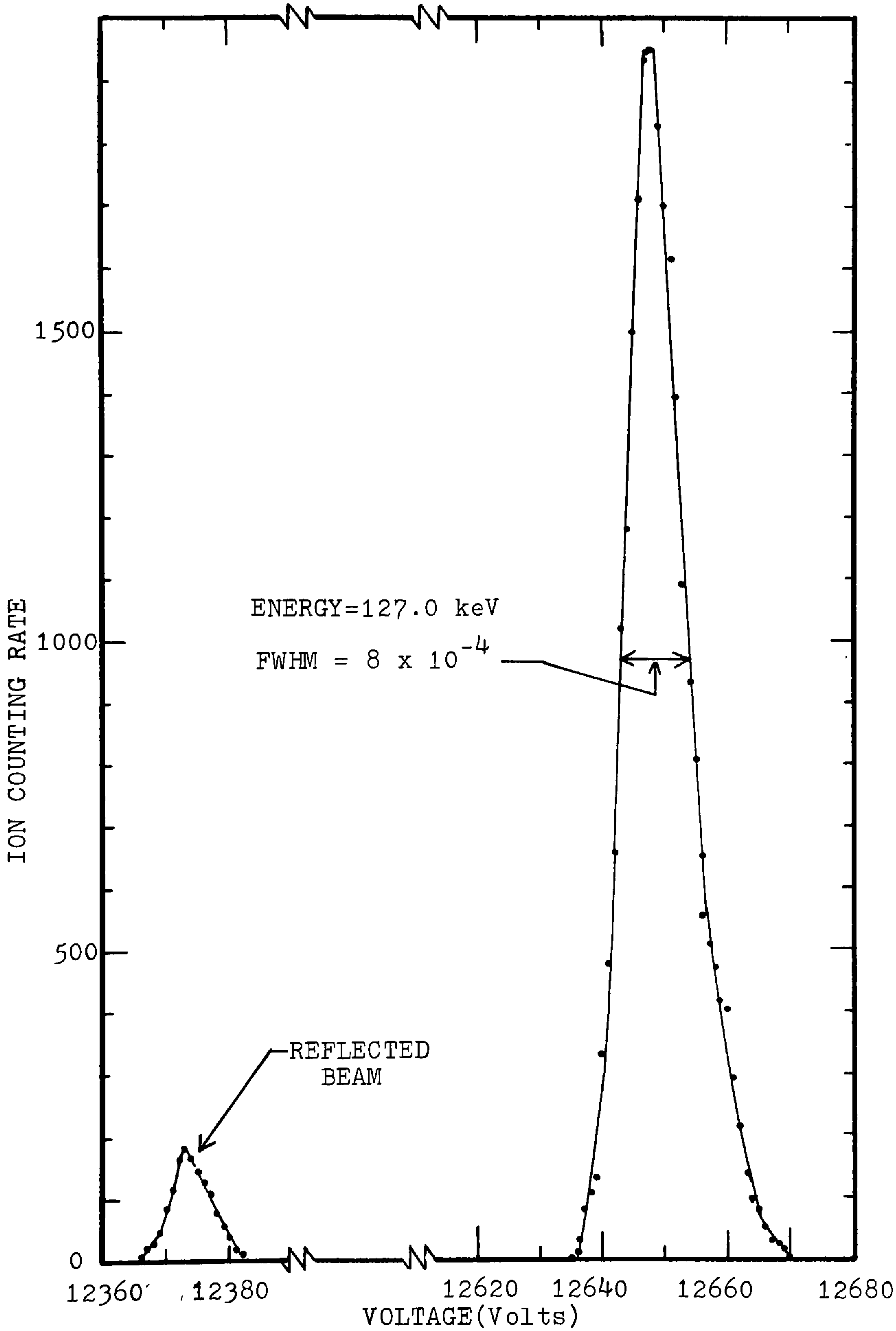

Fig.3-9 The energy profile of the incident Ar^+ ions which was obtained by variation of the electrostatic analyzer voltage. The combined system of the accelerator, the 90^o magnet and the electrostatic analyzer is known to have an energy resolution of better than $(\delta W/W)_{FWHM}=1\times10^{-3}$ with long term stability from preliminary tests with a narrow slit system in the target chamber and electrostatic analyzer.

was changed for the reflected beam, but not for the direct beam which was not reflected from the surface, showing that only the latter was directed along the optic axis.

C Deviations of the Analyzer from its Idealized Design

In the above description, the theoretical analysis of the electrostatic analyzer gives the design parameters based on a purely radial field in a charge-free space. The following deviations of the electrostatic analyzer from its idealized design may occur, and the estimation of the experimental errors for the performance of the analyzer are required.

Since the mean value $r_o = (r_a r_b)^{\frac{1}{2}}$ of the optic axis was assumed in the design, errors arise from misaligning the entrance and exit slit positions, but can be eliminated by means of the small adjustment of electrode voltages away from the symmetric values. The present system was estimated to have less than 0.03% deviation from the mean radius.

When the degree of accuracy required of r_a and r_b is known, the accuracy of a chosen energy calibration from eq. (3-40) can be estimated geometrically by

$$\frac{\delta(\delta V_e/W_o)}{\delta V_e/W_o} = \frac{\ln(r_b/r_a) - \ln\,(r_b \pm \delta_b)/(r_a \pm \delta_a)}{\ln(r_b/r_a)}$$

$$= (\pm\delta_a/r_a) - (\mp\,\delta_b/r_b)\;/\ln(r_b/r_a) \qquad (3\text{-}43)$$

for $\delta_a \ll r_a$ and $\delta_b \ll r_b$. This equation gives $\delta(\delta V_e/W_o)/(\delta V_e/W_o) =$

$\pm 5.0 \times 10^{-6}$ for the electrodes with a tolerance of $\pm 0.005\%$ from the cylindrical shape. However, in the power supply, the accuracy of the voltage calibration, which is quoted from the manufactor, was of the error $\pm 0.25\%$ with a stability of $\pm 0.02\%$ per day, so that the error of the energy calibration is estimated to be less than $\pm 0.5\%$.

The fringing fields of a sector-shaped electrostatic analyzer cause the deviations of the focussing properties from the ideal case. The correction of the fringing field effects on the instrument calibration has been made usually by changing the electrode voltages away from the symmetrical values, or by adjusting the image distance. Herzog[32] and Wollnik[33] obtained approximate solutions for fringing fields in the general case of a toroidal sector, and plotted the distance of the ideal field boundary from the pole face and electrode boundary respectively as functions of the dimensions of the shielding diaphragms which reduce the fringing field regions. The theory of Wollnik[33] predicts for the present electostatic analyzer that the deflection angle ϕ_{eff} between the two effective radial-field boundaries in the beam entrance and exit regions is equal to $\phi_{eff} = 116.0^{\circ}$. This angle $\phi_{eff} = 116.0^{\circ}$ is slightly large compared with the design deflection angle $\phi = 115.0^{\circ}$, but is still smaller than the idealized deflection angle $\phi_{opt} = 127^{\circ}17'$. The design radial-parameters are therefore valid for the real analyzer having the fringing field effects. For the given axial dimensions of the present analyzer, the theory of Wollnik[33] also predicts the effective axial field range to be sufficiently large compared with the design axial-height of the two electrodes, so that the field distortion due to the finite ratio of the electrode height to the slit height (in the axial dimension) can be assumed not to arise at least within the range of z = ±5 mm from the mid-point (r_o, z = 0) of the geometrical electrodes. In fact, the distortion would be increased by the electrode base and cover plates. These plates are likely to be of far less influence on the beam trajectories than the shielding diaphragms for reducing the fringing radial-field regions, since the distortion at each extremity cancels to the first-order near the slit center and can usually be minimzed by extending the ratio of the electrode height to the slit height (in the axial dimension) so that the distortions arise at coordinates remote from the slits.

III-3 Particle Detector[2] and Pulse Counting System

As shown in fig. 3-10, a channeltron (Amperex Electronics Corporation , type B313BL) was placed immediately after the image slit of the electrostatic analyzer to detect the ions in the present cross-section measurements. The channeltron is a windowless particle detector with a 10 mm x 3 mm rectangular aperture and with a closed-end output. Both the channeltron and the analyzer image slit could be moved along the optic axis of the analyzer on a translation stage. The channeltron gain and efficiency[2] are separately described in Appendix II since they were specially investigated in terms of their variations with the point of impact on the channeltron entrance aperture.

Fig.3-10

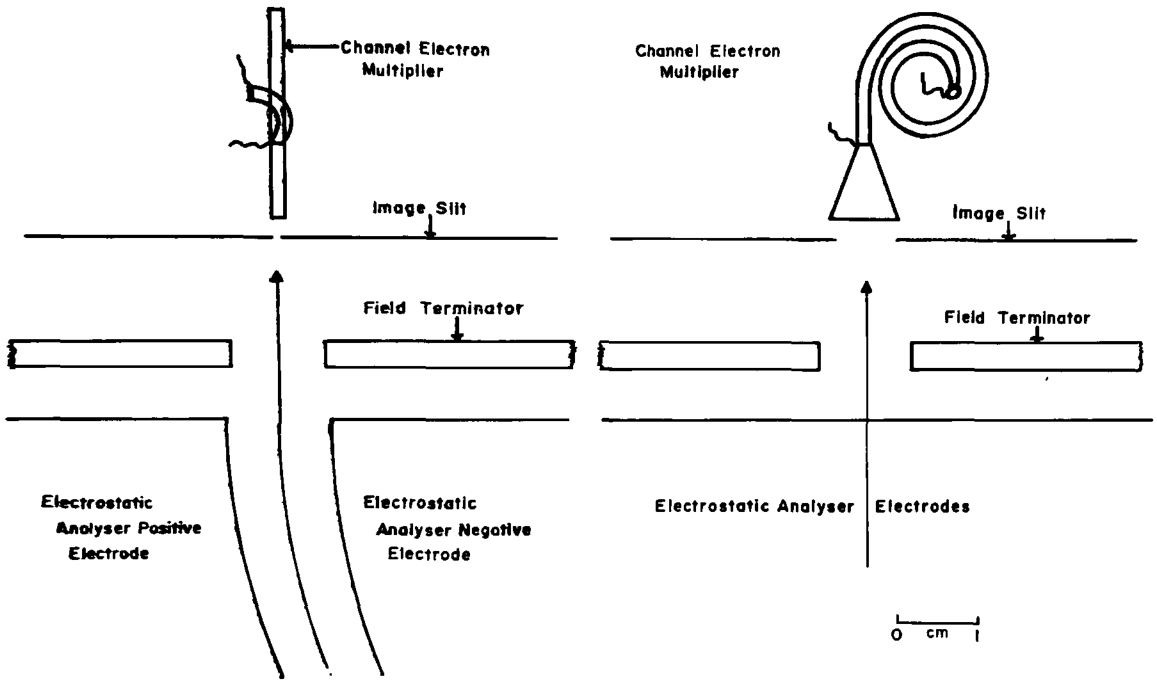

The geometrical arrangement in the image region of the $\pi/2^{\frac{1}{2}}$ electrostatic analyzer. On the left, where the diagram represents the plane of deflection of the ions, the image slit width is 0.95 mm. On the right, where the diagram represents a plane which is perpendicular to the electric field, the image slit length is 7.8 mm. The channel electron multiplier was supported immediately behind the image slit so that its entrance aperture just covered the image slit completely.

A The Pulse Counting Apparatus and Their Settings

As shown in figs. 3-11 and 3-12, the pulses from the channeltron were fed into a conventional pulse amplifier apparatus consisting of an emitter-follower-preamplifier and a main amplifier having a rise time of 0.5 micro-sec, which in turn fed the amplified pulses from the prompt output of the main amplifier to a single channel analyzer-scaler counting system, or from the delay output of the main amplifier through a linear gate to the analog-to-digital converter of a multichannel analyzer whose output was printed out by a teletype.

The normalization of the channeltron counting rates was made in terms of the beam charge which traversed the gas target and struck the upper and lower parts of the horizontal exit slit of the target chamber, where the arrangement of the current integration is shown also in fig. 3-12. The beam transmitted from the exit slit into the electrostatic analyzer was geometrically estimated to be about less than 1.6% of the total population of the beam arrived at the inside face of the exit slit to the target chamber. Since only the ratio of charges collected in consecutive measurements on the incident ions and on the charge changed ions was required, no attempt was made to determine the absolute charges collected by the slit, and neither secondary emission suppression nor gas pressure corrections were made. For a counting rate of a few thousand per sec of the incident beam in the channeltron, it was found that a current of about 10^{-13} Amps was required on the exit slit. This current was amplified in a picoampmeter (Keithley Instruments, Inc., Type 410A) and then integrated in an accurate beam integrator (BNI, Model 1000), so that the channeltron counts independent of the integrated beam current could be obtained for a constant beam charge through the target.

It was first observed that the normalized counting rate had a minimum when the ion beam crossed the entrance aperture of the channeltron. The minimum value occurred when the beam struck the channel surface far inside near the center line of the channeltron[2], as explained in Appendix II. It was found that this minimum could be removed by setting the scaler-discriminator threshold to a lower level. The discriminator threshold was next set at the lowest level which was safely above the system noise, corresponding to a channeltron output integrated current pulse of about 5×10^{-13}C. The channeltron counting rates were then found to have no significant variations with position across the entire channeltron aperture to the edges in the horizontal and vertical directions when careful measurements of the counting rates were made along the image slit of the electrostatic analyzer, as shown in an angular profile of fig. 3-13.

It was found helpful to bias the image slit of the electrostatic analyzer to eliminate secondary electron, and the results shown in fig. 3-13 were obtained with a positive bias of 70 V. Without this bias, it was found that, inside the electrostatic analyzer, secondary electrons generated on the electrodes near the field terminator in the image region or on the image slit, produced a counting rate which for some electrostatic voltages could be several percent of the true ion counting rate. Also, it was found for the present positive ions not only that a positive bias voltage is more effective than a negative bias voltage in reducing secondary electron emission background, but

Fig.3-11

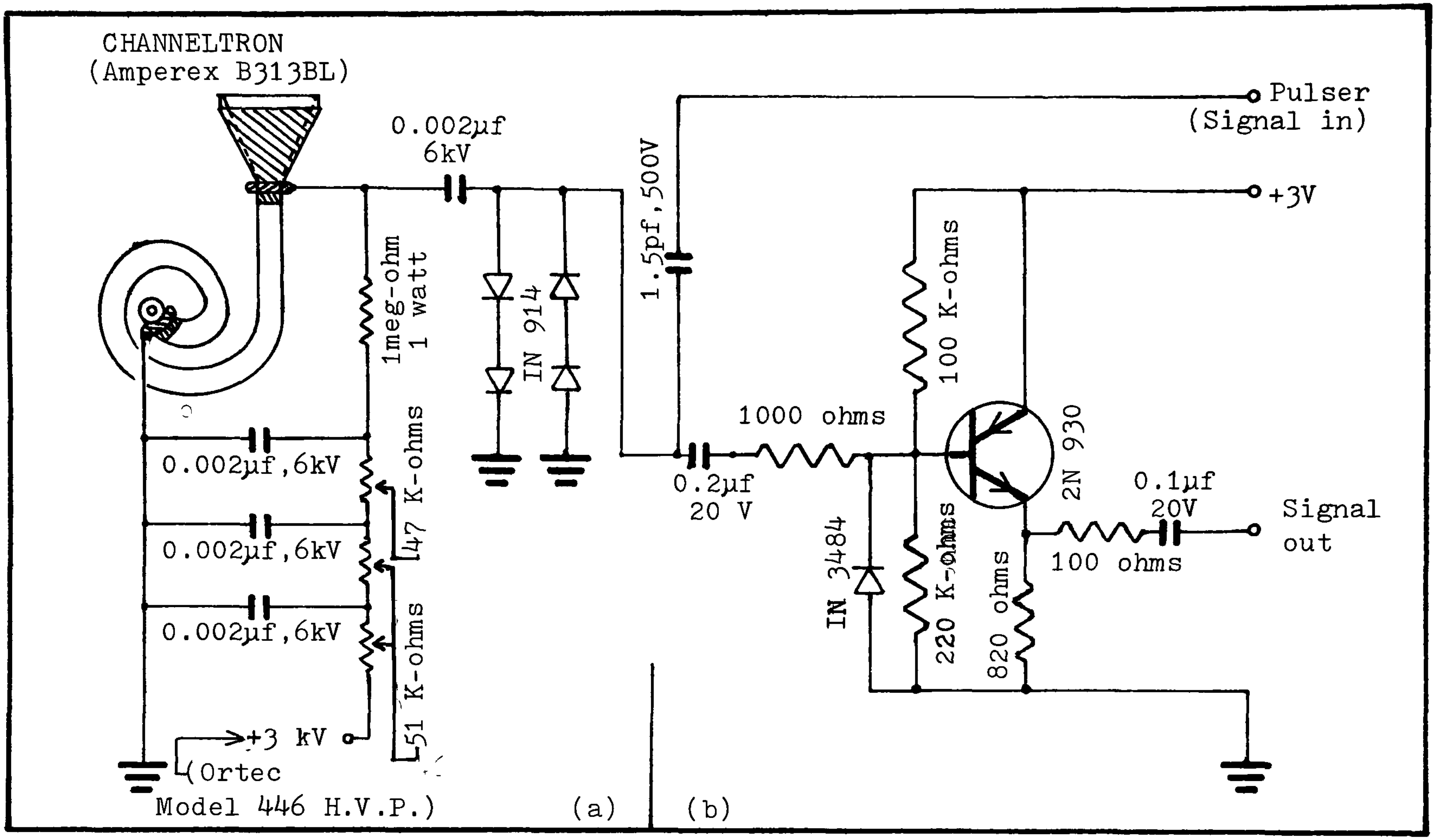

(a) Electrical connections for pulse counting

(b) Schematic of Emitter-Follower

Fig.3-12

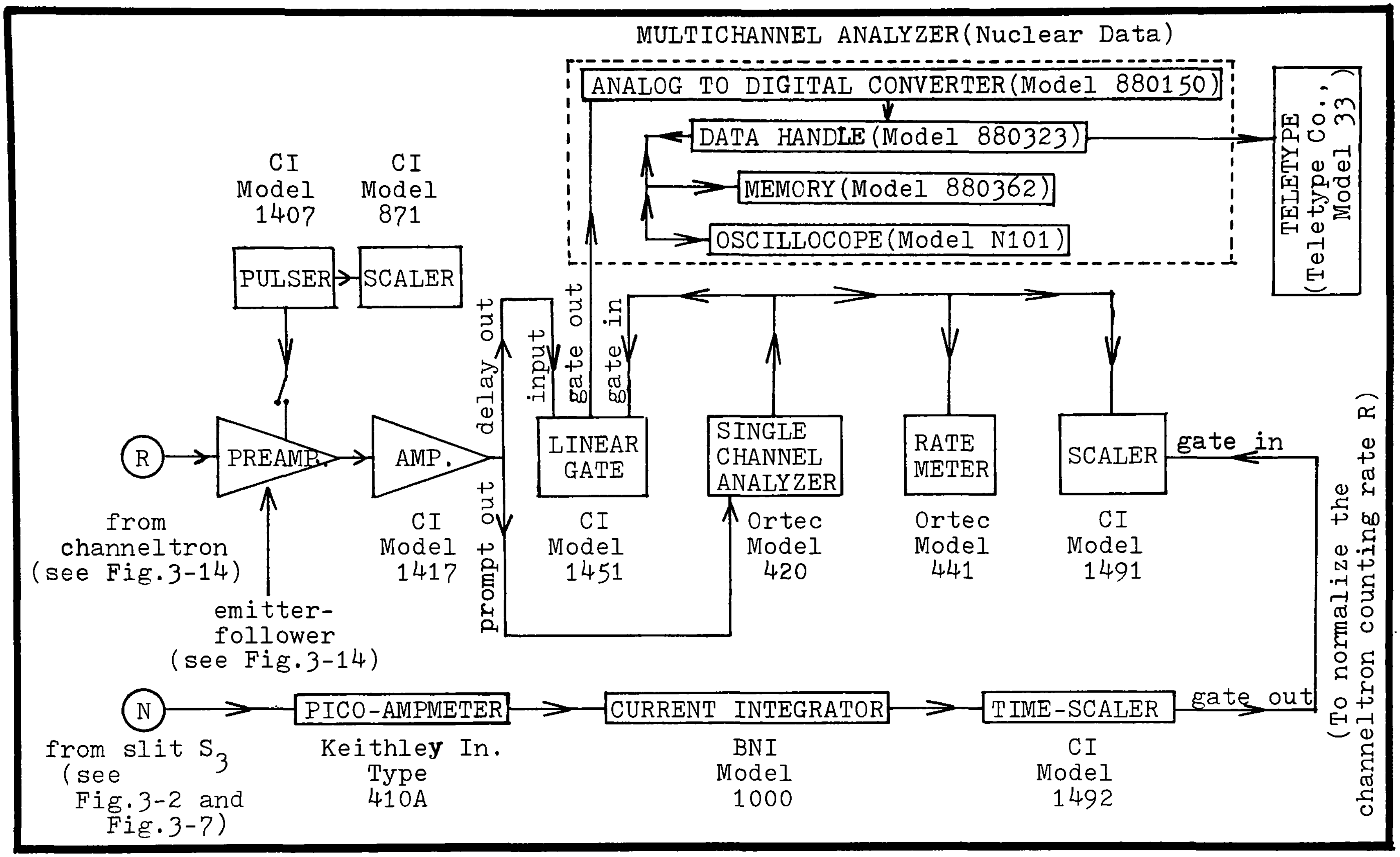

Digital readout instrumentation for pulse counting

Fig.3-13

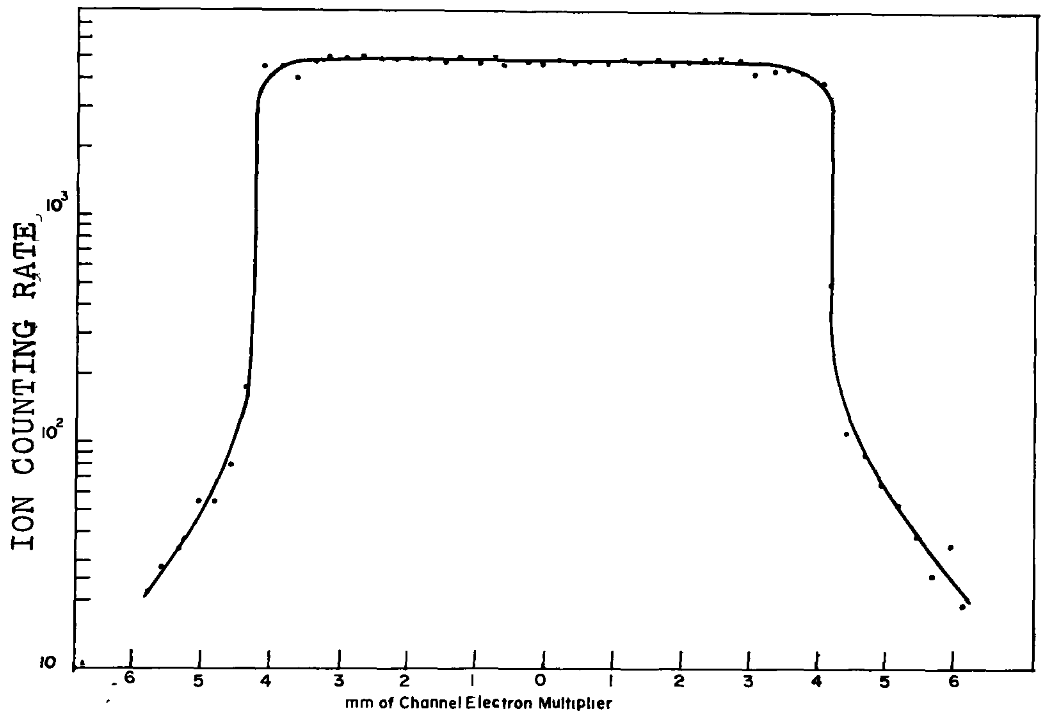

The channel electron multiplier counting rate as a function of the point of impact of the 100 keV N_1^+ ions. The ions were kept to the approximate center of the 0.95 mm image slit width and were traversed along the image slit length. The zero of the length scale is arbitary.

also that the active lengths and positions of angle and energy profile for a given ion-energy were not influenced by the bias voltages. No influence on the channeltron counting rates in the flat-top region of each profile of the angle and the energy was found for changes in the bias voltages. However, it was possible that the bias voltage might have effects on secondary electrons from the channeltron cone, so that some variation in the channeltron current gain could be measured in terms of the bias voltage as described in Appendix II.

B. Measurement of the Dead Time in the Counting System

One simple method for measuring the dead time of the whole counting system from the preamplifier to the scaler was to compare the response of the counting apparatus to the pulses produced by two independent pulse generators, taken separately and then taken simultaneously. In an experimental arrangement shown in fig. 3-14, the two outputs of the regular pulse generators with definite frequencies f_a and f_b could be added. It was important that there was no feedback from one generator frequency to the other. The pulse shapes and amplitudes for these two frequency pulses were approximately the same as the pulses for which the counting system was designed.

When the two given constant frequency pulses were separately passed through the counting system, there are no dead time counting losses because the time separation between neighbouring pulses was greater than the dead time t of the counting system, i.e. $1/f_a > t$ and $1/f_b > t$. Since there were no counting losses due to the dead time, the observed counting rates n_a and n_b through the counting system measured directly f_a and f_b.

A measurement of both the two frequency simultaneously through the counting system will produce the dead time counting losses between the two frequency pulses. We consider f_b as being the dead time loss generator, and f_a as being the sensor of these losses. In one second there are f_b pulses. The system is dead for $(f_b t)$ seconds per second. During the time $(f_b t)$, the pulser "a" will produce $(f_b t) f_a$ pulses per second. These pulses are lost, when we assume that the dead time t is a constant. Notice that this is not a first-order approximation to an exponential as with randomly spaced pulses. There is symmetry in f_a and f_b, so the above logic could be obtained with f_a and f_b interchanged. A measurement of n_{a+b} gives a counting rate $n_{a+b} = f_a + f_b - f_a f_b t = n_a + n_b - n_a n_b t$, so that all of these quantities are observables except the dead time t which is therefore calculable

$$t = (n_a + n_b - n_a n_b t)/n_a n_b \qquad (3\text{-}44)$$

To avoid errors due to fluctuations in frequencies when measuring the small difference between two large counts, it is better to measure n_a, n_b, and n_{a+b} all at the same time. We consider that the counting rate n_b is much greater than the counting rate n_a. The error in n_a will be much smaller than that in n_b if the frequencies are about equally stable. If the stability of n_a is such that $(n_a + n_b - n_{a+b})$ is comparable or greater than the error in n_a, then n_a need not be measured each time. It is sufficient to measure n_b and n_{a+b} simultaneously over the same time interval. The measured value of t will be subject to random errors in so far as $(n_a + n_b - n_{a+b})$ involves the time overlap of

Fig.3-14
Instrumentation for measurement of dead time in the counting system

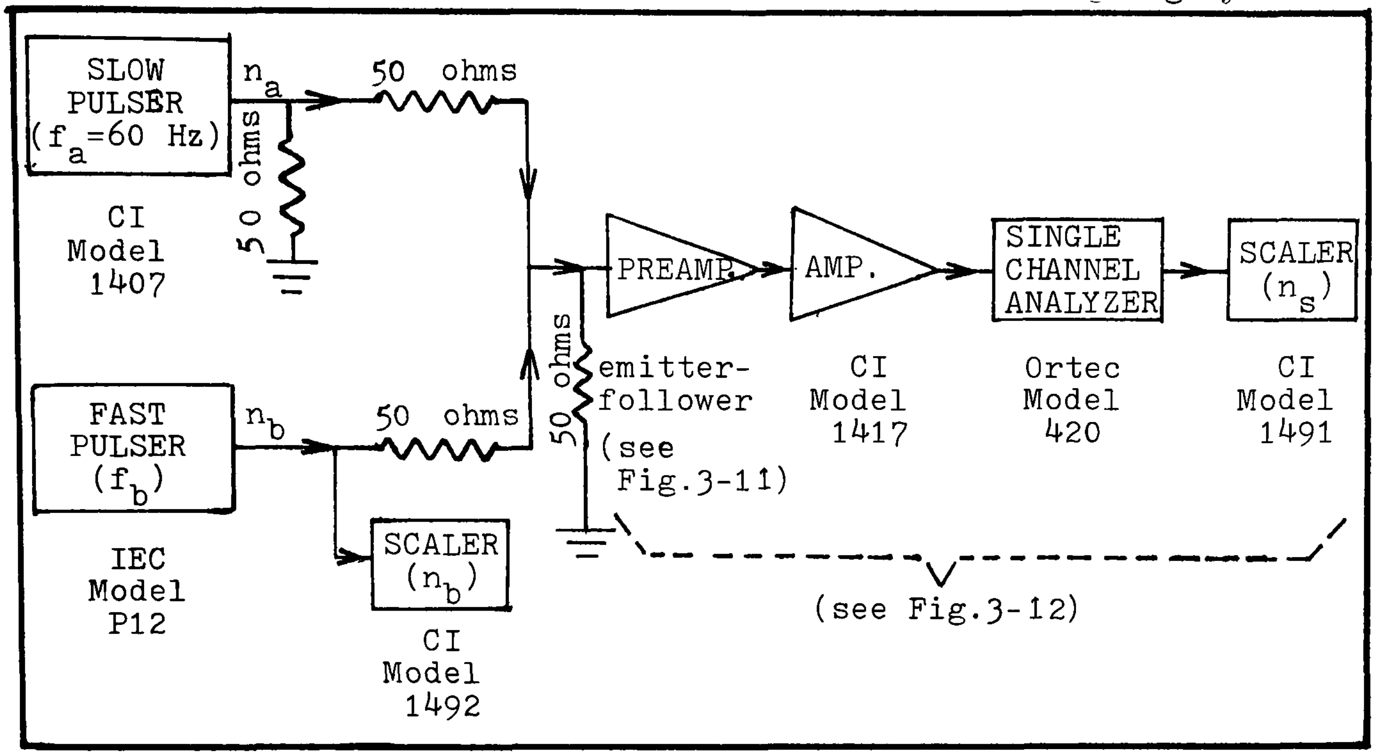

Fig.3-15
The counting loss $(n_a+n_b-n_s)$ as a function of the observed counting rate n_b. The fractional counting loss for n_s=6.8 kHz is estimated to be about 0.02 %, and the dead time of the counting system is then 2.5 micro-seconds.

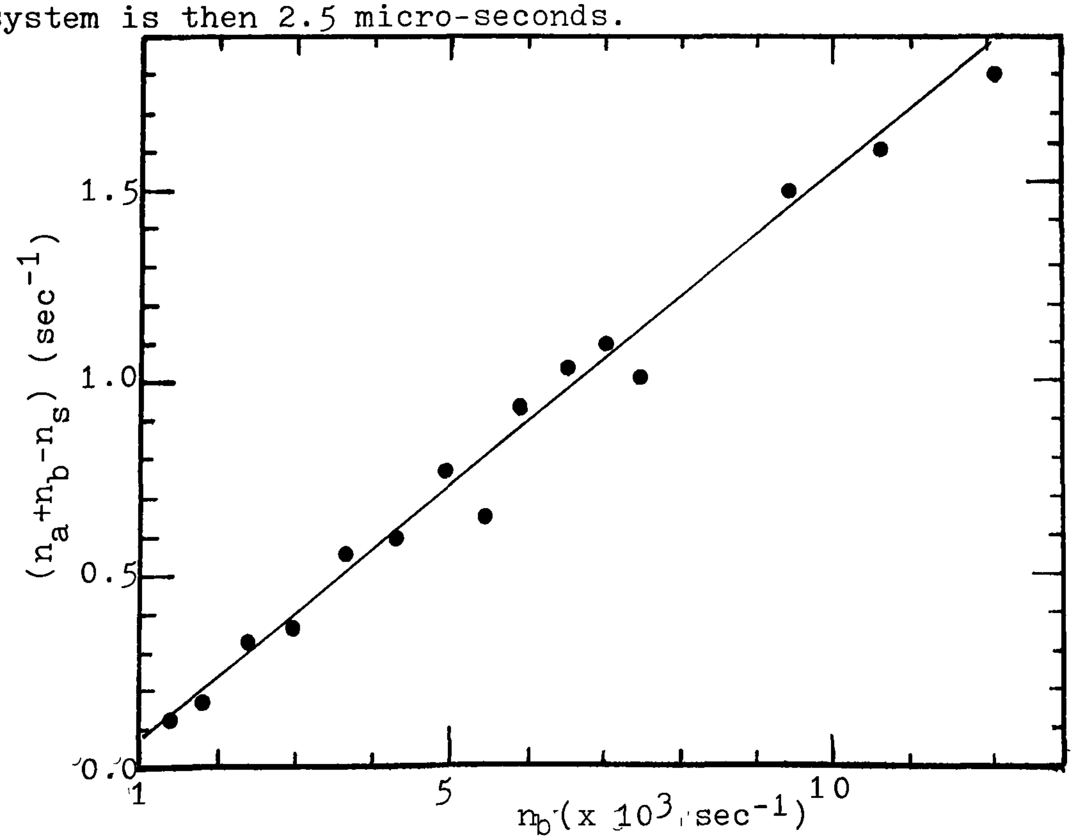

the two regular but independent pulse sources.

A graphical plot of $(n_a + n_b - n_{a+b})$ against n_b should have a slope $(n_a t)$. If n_a is kept constant, this should be a straight line. By fitting a best straight line to the data points which is shown in fig. 3-15, the dead time of the counting system was estimated to about 2.5 micro-seconds, and the fraction loss for the counting rate n_{a+b} of less than 6.8 kHz is less than 0.02%. In order to keep the pile-up and dead time problems in the counting system to an acceptable level, the channeltron counting rates were always kept below 6 kHz in all the present measurements.

III-4 Operative Relation between the Accelerator and the Magnetic and Electrostatic Analyzer, and Test of the Whole System

The magnet field B required to focus ions of energy W is given by

$$B = (2mW)^{\frac{1}{2}}/ner \tag{3-45}$$

where ne and m are the charge and mass of the ions, respectively, and r is the radius of curvature. On the other hand, the voltage δV_a required to accelerate this can be

$$\delta V_a = W/ne \tag{3-46}$$

Combining the equations, we have

$$B = (2n\ \delta V_a/ne)^{\frac{1}{2}}/r$$

or

$$\frac{m\ \delta V_a}{n} = \tfrac{1}{2}er^2B^2 \tag{3-47}$$

Thus a universal curve should be found when the quantity ($m\ \delta V_a/n$) is plotted against $(I_B)^2$. When the magnet current I_B is proportional to the magnetic field B, and the saturation effects are small; this curve should be nearly linear as shown in fig. 3-16. From this figure, the desired magnet current I_B was, in practice, read off when a search was to be made for a certain ion of some chosen energy. Emerging from the gas target chamber, the incident or charge changed particles were deflected in the electrostatic analyzer whose voltage δV_e (which was estimated to be less than ±0.5% from the manufacture's voltage calibration) was calculated to be $(\delta V_e)_i = [2\ln(r_b/r_a]\delta V_a =$ 0.0996 δV_a for deflecting the incident ions and therefore to be $(\delta V_e)_f = (n_i/n_f)(\delta V_e)_i$ for deflecting the charge-changing ions from the incident ions during their passage through the gas target, where the subscripts i and f are referred to as the incident and charge-changed particles, respectively.

In a preliminary test of the whole beam transport system the slits mounted on the entrance and exit collimators of the target chamber were much narrower than those used in the cross-section measurements, and the object and image slit of the electrostatic analyzer were also much narrower and were placed at their original designated positions. The test indicated an energy resolution of better than $(\delta W/W)_{FWHM} = 8 \times 10^{-4}$ as shown in fig. 3-9, where for each of the values δV_e, the symmetrical electrode voltages of $|+V_b| = |-V_a|$ were applied to the respective electrodes. This resolution represents the combined effects of the energy spread of the incident beam from the 90^{o} magnetic analyzer and the resolution $(\delta W/W_o)_{FWHM}$ of the electrostatic analyzer itself.

Fig.3-16

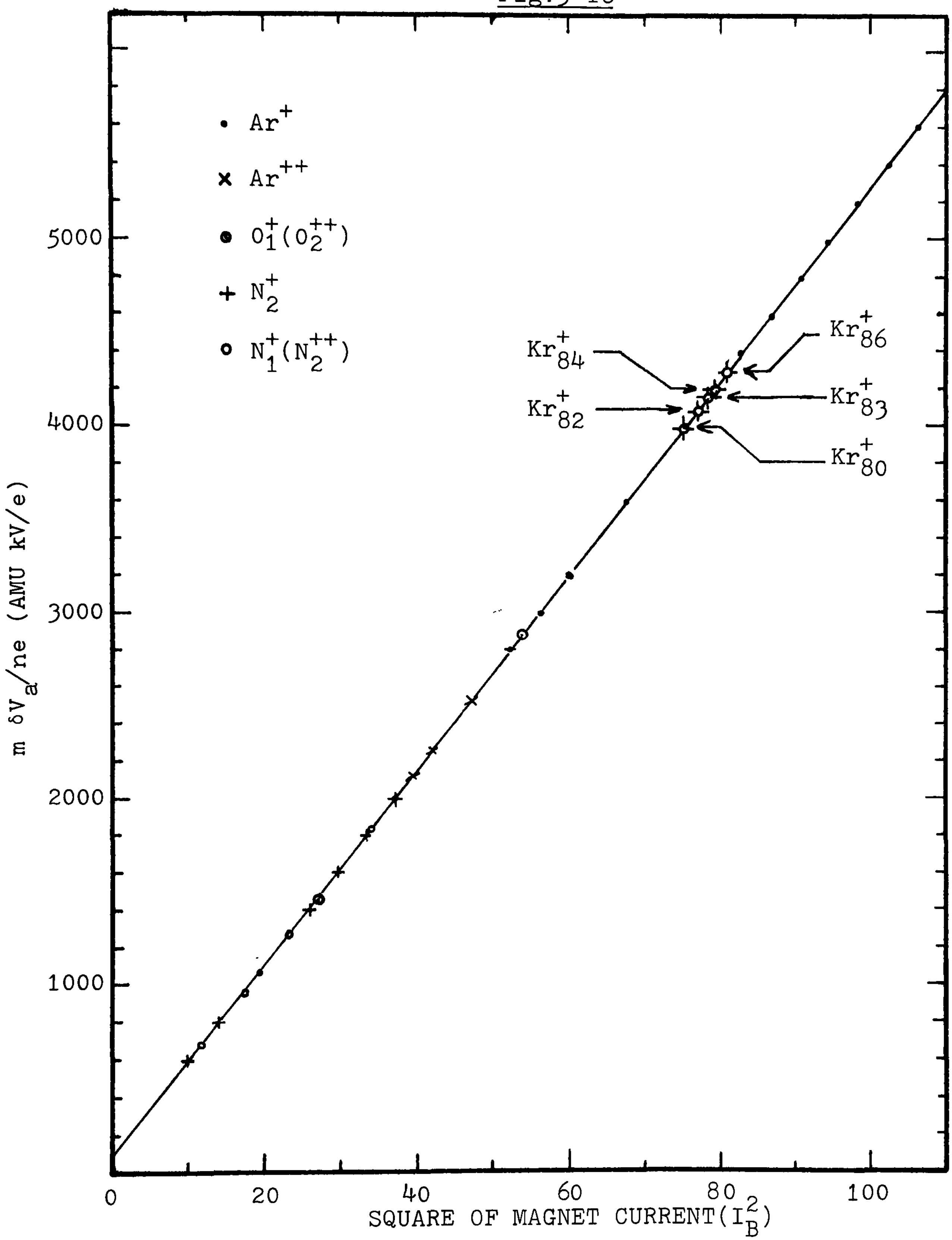

Accelerator voltage δV_a as a function of the magnetic current I_B. The voltage δV_a is in units of kV. The magnet current I_B, which is proportional to the magnet field approximately by B(Gauss)=42.0 I_B, is in arbitary units.

The long term stability was found to be at least of the same order as the resolution.

In terms of the wide slits used for the cross-section measurements, this resolution represents an image spread of 0.2 mm at the detector entrance, which is to be compared with the 0.95 mm image slit width. The energy profile of the system when using this large slit width therefore appears flat topped, and all the measurements which we present here were made with a deflection voltage corresponding to the center of the energy profile, where the ions presumably are centered in the middle of the 0.95 mm image aperture width.

In order to test the influence of fringing fields on the real beam trajectory in the electrostatic analyzer, the shape and position of the image (energy) profile as a function of V were observed while changing the electrode voltages away from the symmetric voltages of $|+V_b| = |-V_a|$, i.e., while raising the magnitude of one electrode voltage and reducing the magnitude of the other so that no change in the value of $\delta V_e = V_b - V_a$ was made. No significant change in the resolution as a function of δV_e was observed. This suggests that the fringing fields are adequately negligible on the ion beam which moves in the vicinity of the optic axis of the electrostatic analyzer.

In the test with the N_1^+ ion beam, it was possible that the N_1^+ ion beam also could include N_2^{++} ions. Since both N_1^+ and N_2^{++} ions have the same charge to mass ratio, they have the same deflections in all electric and magnetic fields. In principle, the incident ions N_1^+ and N_2^{++} may be distinguished by the charge-changing processes during their passage through a gas target. The only charge-changing process which will produce ions requiring twice the deflection voltage in the electrostatic analyzer is $N_2^{++} \rightarrow N_2^+$, which has no equivalent for the N_1^+ beam. During measurements with the nitrogen beam it was found that counting rates for the twice voltage setting (N_2^+) were less than the half voltage setting (N_1^{++}). The σ_{21} cross-sections for the molecular ions are presumably much larger than the electron loss cross-sections σ_{12} for the atomic ions in the present ion energy range, so that the contamination of N_2^{++} ions in the N_1^+ ion beam was concluded to be negligible.

This analysis neglects the presence of N_2^{++} ions which are indistinguishable from N_1^{2+} in the analyzer. It is very unlikely that the significant numbers of these ions would be produced because of the very small charge exchange cross-sections involved. In constrast to this measurement, the presence of considerable O_2^{++} ions was found experimentally in the O_1^+ ion beam.

III-5 Control and Measurement of Gas Target Thickness.

Using the target gases for charge-changing atomic collisions, the number π of target particles per unit cross-sectional area has to be measured as $\pi = Xn$ where X is an effective length of target thickness in the direction of incident beam passing through a gas target chamber having the beam entrance and exit slit orifices.

In the effective target length X due to the differential gas pumping through the orifices, Toburen et al.[35] suggested that a molecular flow theory gives $X = X_g + 2(r_1 + r_a)$ where X_g denotes the geometrical target length between the orifices, and r_1 and r_2 are the radii of the orifices respectively. However a kinetic theory of gas flow through an orifice by Patterson[36] predicts a density distribution such that the density in the plane of the slit is the average of the internal and external gas densities. For negligible external gas pressure, the density distribution at the center of the slit orifice is therefore half of the distribution far inside the target chamber. The kinetic theory also predicts the variation of the density distribution on either side of the slit. For a wide range of thin slit shapes, it predicts that there is a symmetry in the distribution as a function of the distance x along the axis which is perpendicular to the orifice plane and starts from the orifice center, so that $n^- = 1 - n^+$ where n^- and n^+ are the relative density distributions in the upsteam and downstream regions, respectively, as shown in fig. 3-17 for the present slits. With such a symmetry, it is easy to show that the effective length X for ions which traverse the entrance and exit slits is the same as the physical target length X_g which was used in this experiment, so that there is no length correction due to the slit sizes through the differentially pumped target gas, when the pressure inside reaches a reasonable uniform value.

From the equation of state in the limit of low pressure within the gas target chamber, the number n of target particles per unit volume is given in the form for monatomic gases

$$n = P/(1.0351 \times 10^{-19}\ T)\ \text{atoms/cm}^3 \qquad (3\text{-}48)$$

where P is the pressure in Torr, T is the absolute temperature in ^oK, and $R = 1.0351 \times 10^{-19}$ cm^3 Torr/(atoms ^oK) is the Boltzmann constant

Fig.3-17

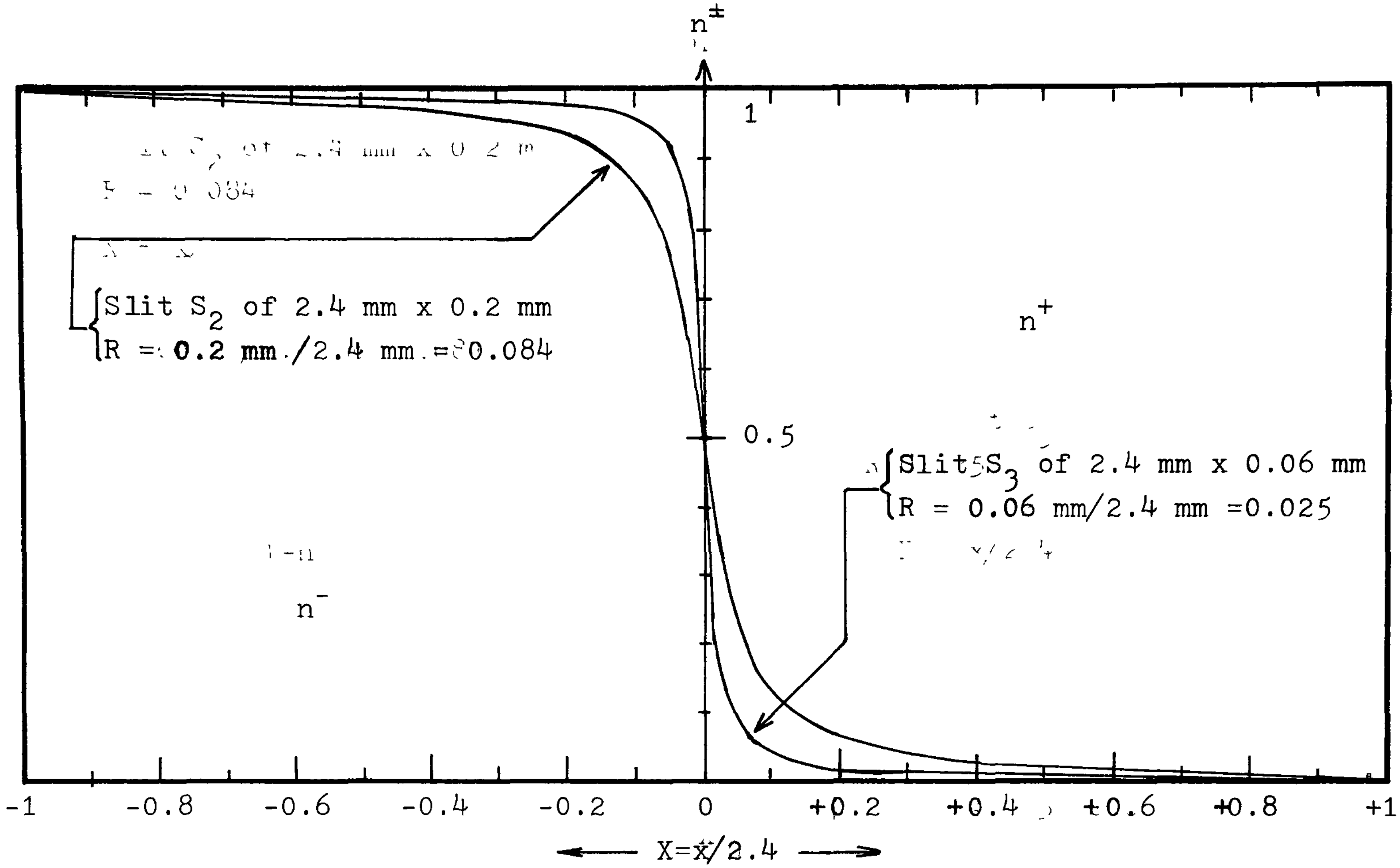

A kinetic theory of gas flow through an orifice by Patterson[36] predicts that there a symmetry in a density distribution as a function of the distance x along the axis which is perpendicular to the orifice plane and starts from the orifice center, so that $n^-=1-n^+$ where n^- and $n^+=\pi^{-1}\tan^{-1}[\frac{1}{4}(R/X)(X^2+\frac{1}{4}(1+R^2))^{-\frac{1}{2}}]$ are the relative density distributions in the upstream and downstream regions, respectively. Here, the ratios R=b/a and X=x/a are for rectangular slit size of a mm x b mm.

For a given temperature T ^{o}K, the volume density n atoms/cm^3 is determined from the measurement of the target gas pressure P in Torr.

In the present experiment of the charge-changing atomic collisions of N_1^+ and Ar^{++} ions with the Ne, Ar, and Kr targets, the target gases used were specified as having a purity of 99.999%. Before each measurement of the cross-sections, the residual gases within the target chamber were evacuated for several hours, usually by opening the vacuum valve between the target chamber and the beam line.

The target pressure was controlled by a thermal-mechanical leak (Ortec Model 341) in the range between 10^{-4} Torr and 10^{-3} Torr. A constant temperature was maintained with a variation of less than 1^{o}C during each measurement of the cross-sections. Care was taken that all the surfaces of the target chamber which were in contact with the target gas were kept at a constant temperature. The pressure was allowed to stabilize after each change in the thermal mechanical lea-setting.

The target pressure was measured with a capacitance manometer (MKS Instruments, Type 145 BHS-1: 1 mmHg Head Baratron) which was connected through a short length of a copper tube (i.d. = ¼ inches) to the target chamber in a region well away from the gas inlet port and from the gas flow through the slit orifices. In spite of being thermostatically controlled by a proportional heater circuit, the gauge was found to be sensitive to short term ambient temperature variations. The stability was much improved by enclosing the gauge within a polystyrene foam lined box, so that the drifts were reduced to be less than 10^{-5} Torr per day. A simple test for the zero set and linearity of the gauge was made with an ionization gauge (Veeco Instruments Inc., Model IG-2000-K Head with Model RG-83 Control Unit) which was not calibrated accurately. The result of the test showed that there was a disagreement of about 16% between the two gauges, but the zero setting and linearity were very good. The manufacture's calibration of the capacitance manometer used in this experiment was given with an error of less than 0.2%, so that the instrumental error of the capacitance manometer was assumed to be negligibly small in the present cross-section measurements.

CHAPTER IV EXPERIMENTAL METHOD AND PROCEDURE

The experimental method and procedure for measuring total charge-changing cross-sections on atomic or molecular ions passing through a "thin-static" gaseous target under the so-called "single collision conditions" are well known. But, the approximation of single collision conditions is inexact in experiment, so the theory has been modified in order to determine the absolute cross-sections taking account of the few percent of the ions which made more than one collision during their passage through the gas target.

IV-1 Equations for Charge-Changing Processes

When an ion of charge i collides with atoms of a target gas, the ion may lose or capture one or more electron on each encounter. The probabilities for these processes are described by cross-sections σ_{if}, and i and f denote the charges which the ion carries before and after a single charge-changing collision. The cross-section σ_{if} is given in units of cm^2/atom.

The capture or loss of more than one electron in the collisions is almost always small compared with that for a single electron, and will be neglected in the following analysis.

The variation of the charge composition of an ion beam penetrating through a gaseous target is described by a system of differential equations

$$\frac{dY^f}{d\pi} = \sum_{i \neq f} \sigma_{if} Y^i - \sum_{f \neq i} \sigma_{fi} Y^f \qquad (4\text{-}1)$$

where Y^i and Y^f are the fractions of the ions which carry charges i and f, respectively, and the target thickness $\pi = nX$, where X = effective target length, is the number of atoms/cm^2 in the path of the ions. In principle, i and f may vary in the range from -1 to Z, where Z is the atomic number of the ion; however, if no negative ion exists, the lower limit of the indices must, of course, be replaced by zero. In the practical situation of cross-section measurements, it is sufficient to retain a number of charge states which, depending on Z, lie within a few different charge states. Eq. (4-1) is a theoretical differential equation for obtaining the exact solution. The desired solution can be mathematically represented in a power series form

$$Y^f = A_f + B_f\pi + C_f\pi^2 + D_f\pi^3 + \ldots. \tag{4-2}$$

where A_f, B_f, C_f, and D_f are the coefficients of each power of π. For the target thickness $\pi = 0$ and only one incident charge state i, all coefficients A_f must be zero, whereas $A_i = 1$. Substituting eq. (4-2) into eq. (4-1), and differentiating eq. (4-2), we have

$$\frac{dY^f}{d\pi} = \Big(\sum_{i\neq f}\sigma_{if}A_i - \sum_{f\neq i}\sigma_{fi}A_f\Big) + \Big(\sum_{i\neq f}\sigma_{if}B_i - \sum_{f\neq i}\sigma_{fi}B_f\Big)\pi$$

$$+ \Big(\sum_{i\neq f}\sigma_{if}C_i - \sum_{f\neq i}\sigma_{fi}C_f\Big)\pi^2 + \ldots.$$

$$= B_f + 2C_f\pi + 3D_f\pi^2 + \ldots \tag{4-3}$$

which must be valid over a range of values of π, so that the coefficients of each power of π must be equal

$$B_f = \sum_{i \neq f} \sigma_{if} A_i - \sum_{f \neq i} \sigma_{fi} A_f$$

$$2C_f = \sum_{i \neq f} \sigma_{if} B_i - \sum_{f \neq i} \sigma_{fi} B_f$$

$$3D_f = \sum_{i \neq f} \sigma_{if} C_i - \sum_{f \neq i} \sigma_{fi} C_f \qquad (4\text{-}4)$$

....

The coefficients can be successively determined starting from A_i and A_f.

Even though the purely mathematical derivation of the equations from eq. (4-1) to eq. (4-4) is straight forward and needs no more explanation, it is important to point out some restrictions on their use. The above equations take into account only those collisions in which the charge of the ion is really changed, and they do not include elastic collisions or encounters which lead only to excitation of the ions. It is further assumed that the gas target is sufficiently dilute so that the ions, possibly excited in collisions, always have enough time to return to their ground states before any subsequent collision occurs. Then, all cross sections σ_{if} and σ_{fi} in the above equations are strictly associated with the ground states of ions with charges i and f. In addition, it is necessary that the target be so thin that the average momentum loss per ion in the target is negligible. Finally, it is assumed that the product beam in the target is observed essentially in the forward direction to integrate the beam emerging from the target.

When only a few charge states are important, simple analytical solutions of eq. (4-1) can be found to the above power series representation. According to the present experimental evidence, the present single electron loss and capture cross-sections σ_{12} and σ_{21} can be represented adequately by a four-charge-component system in which the cross-sections for changes of two or more electrons in a single collision are neglected:

$$\frac{dY^{o}}{d\pi} = -\sigma_{01} Y^{0} + \sigma_{10} Y^{1+}$$

$$\frac{dY^{1+}}{d\pi} = +\sigma_{01} Y^{0} - (\sigma_{10} + \sigma_{12}) Y^{1+} + \sigma_{21} Y^{2+}$$

$$\frac{dY^{2+}}{d\pi} = + \sigma_{12} Y^{1+} + (\sigma_{21} + \sigma_{23}) Y^{2+} + \sigma_{32} Y^{3+} \qquad (4\text{-}5)$$

$$\frac{dY^{3+}}{d\pi} = + \sigma_{23} Y^{2+} - \sigma_{32} Y^{3+}$$

The solution of each of these differential equations can be given in a power series similar to eq. (4-2) and their coefficients are derived using eq. (4-4), so that, for a pure incident charge state $1+$ (at $\pi = 0$, $A_{1+} = 1$ and $A_{0} = A_{2+} = A_{3+} = 0$ in the power series solutions), the fractions Y^{1+} and Y^{2+} for obtaining the single electron loss cross-section σ_{12} are given by

$$Y^{1+} = 1 - (\sigma_{10} + \sigma_{12})\pi + \tfrac{1}{2}[\sigma_{01}\sigma_{10} + (\sigma_{10} + \sigma_{12})^{2} + \sigma_{21}\sigma_{12}]\pi^{2}$$

$$- (1/6)\{ \sigma_{01}\sigma_{10} (\sigma_{01} + \sigma_{10} + \sigma_{12}) + (\sigma_{10} + \sigma_{12})$$

$$[\sigma_{01}\sigma_{10} + (\sigma_{10} + \sigma_{12})^{2} + \sigma_{21}\sigma_{12}] + [\sigma_{21}\sigma_{12}$$

$$(\sigma_{10} + \sigma_{12} + \sigma_{21} + \sigma_{23})] \} \pi^{3} + \ldots\ldots \qquad (4\text{-}6a)$$

$$Y^{2+} = \sigma_{12}\,\pi\,\{1 - \tfrac{1}{2}(\sigma_{10} + \sigma_{12} + \sigma_{21} + \sigma_{23})\pi$$

$$+ (1/6)[\sigma_{01}\sigma_{10} + (\sigma_{10} + \sigma_{12})^2 + \sigma_{21}\sigma_{12}$$

$$+ (\sigma_{21} + \sigma_{23})\,(\sigma_{10} + \sigma_{12} + \sigma_{21} + \sigma_{23})$$

$$+ \sigma_{32}\sigma_{23}]\,\pi^2 + \ldots.\} \qquad (4\text{-}6b)$$

For a thin target where $\sigma_{if}\pi \ll 1$, the solutions of eqs. (4-6a,b) reduce to

$$\sigma_{12} = (Y^{2+}/Y^{1+})/\pi = Y_{12}/\pi \qquad (4\text{-}7)$$

under the single collision conditions. In experimental measurements, the variation of the fractional ratio $Y_{12} = Y^{2+}/Y^{1+}$ is obtained over a range of π values. In principle, there are two methods for producing the range of π values where $\pi = nX$ as described in the section III-5 of Chapter III: (1), varying the length of the gas target chamber at constant target density n which is determined from the measurement of the gas pressure P, and (2), varying the density n within the gas target chamber of constant length X. As is done in this experiment, the second method has been used usually, so that a linear relation between the ratio Y_{12} and the target gas pressure P has been conventionally used as evidence of the validity of eq. (4-7) and, therefore, of single collision conditions. The cross-section σ_{12} is conventionally determined from the slope of the linear part of the relation. However, if the target thickness used in the measurements was such that a few percent of the ions made more than one collision during their passage through the gas target, the σ_{12} cross-section formula becomes

$$\sigma_{12} = Y_{12} C_{12}/\pi \tag{4-8}$$

where the target thickness correction factor C_{12} with respect to the single collision cross-section formula of eq. (4-7) is given by

$$\begin{aligned} C_{12} = (1 + \tfrac{1}{2}Y_{12})^{-1} \{ 1 - \tfrac{1}{2}(\sigma_{10} - \sigma_{21} - \sigma_{23})\pi \\ + \frac{1}{12} [4(\sigma_{01}\sigma_{10} + \sigma_{21}\sigma_{12}) + (\sigma_{10} + \sigma_{12} - \sigma_{21} - \sigma_{23})^2 \\ - 2\sigma_{23}\sigma_{32}]\pi^2 + \ldots\ldots. \} \end{aligned} \tag{4-9}$$

Deriving in a similar way from equations (4-6) to (4-9) the results of the σ_{21} cross-section formulation for a pure incident charge state 2+ are given under the single collision conditions

$$\sigma_{21} = Y_{21}/\pi \tag{4-10}$$

and with a few percent multiple collisions

$$\sigma_{21} = Y_{21} C_{21}/\pi \tag{4-11}$$

where the target thickness correction factor C_{21} is given by

$$C_{21} = (1 + \tfrac{1}{2}Y_{21})^{-1} \{1 - \tfrac{1}{2}(\sigma_{23} - \sigma_{10} - \sigma_{12})\pi$$

$$+ \frac{1}{12}[4(\sigma_{12}\sigma_{21} + \sigma_{32}\sigma_{23}) + (\sigma_{21} + \sigma_{23} - \sigma_{10} - \sigma_{12})^2$$

$$- 2\sigma_{01}\sigma_{10}]\pi^2 + \ldots \} \qquad (4\text{-}12)$$

According to experimental evidence[27,28], the electron loss cross-sections for the ions of a given charge i are generally smaller than the electron capture cross-sections by a factor between 10 and 100 in the present ion energy range, though , in some exceptional cases, Lockwood[39] observed that the σ_{12} cross-sections are larger than the σ_{10} cross-sections have been observed.

IV-2 The measurement of the Y_{if} ratio variation with pressure

In this experiment, the fractions Y^i and Y^f of the ions emerging from the target chamber were not determined absolutely, but normalized counting rates R^i and R^f associated with them were measured as described in section III-3 of Chapter III, so that the counting rate ratio $R_{if} = R^f/R^i$ represents the fractional ratio Y_{if}.

Taking account of the effect of the angular spread in the charge-changing processes, the counting rates R^i and R^f were interpretated as being proportional to the areas under the angle and energy profiles of the electrostatic analyzer rather than just as the optimized counting rates R_o^i and R_o^f, as will be described in the following procedure for each of the cross-section measurements. At the lowest target pressure, the energy and angle counting rate profiles of the initial charge state i and final charge state f ions were first measured. The energy profile $R(V, \bar{\theta})$ was obtained by plotting the ion counting rate versus the deflection voltage V which is the potential difference between the analyzer electrodes. The angle profile $R(\bar{V},\theta)$ was obtained by mechanical rotation of the analyzer about the midpoint of the target as described in section III-2 of Chapter III. Figures 4-1 and 4-2 show examples of the energy and angle profiles on the electron loss and capture processes, respectively. From these measurements, the optimum voltages $\bar{V}^i$ and $\bar{V}^f$ were read off in the central plateau regions of the respective profiles. Here, $\bar{\theta}$ was always found to be the same for both the initial charge state i and final charge state f ions, but there were systematically a few volts difference between $2\bar{V}^{2+}$ and $\bar{V}^{1+}$ voltages due to the small errors in the linearities of the two power supplies of the electrostatic analyzer. The optimum counting rate ratio, R_o^f/R_o^i, variation with the target gas pressure P was then obtained by measuring the ratio first at the lowest pressure and then for the target gas pressures which were increased step by step. The two counting rates were measured alternately more than ten times in short runs under stable conditions of the beam and target gas, in order to minimize the effects of beam energy drifts. The totals of the counts of each type of ions used in the ratio calculation, and the error of this ratio was estimated by the n-1 weight of the fluctuations between the ratios which were calculated for each pair of the two counting rates, rather than by using the square root standard deviations of the totals of the counts of each type of ions. Figures 4-3 and 4-4 show the variation of the optimum counting rate ratio R_o^f/R_o^i with the target gas pressure P.

During the optimum ratio measurements, the energy profiles of both the types of the ions were made at an intermediate point in the pressure range to detect any shift in the beam energy due to an accidental defect or failing of any the beam transport apparatus. After the optimum ratio measurements, both the energy profile $R(V,\bar{\theta})$ and the angle profile $R(\bar{V},\theta)$, which had been measured at the lowest pressure, was remeasured at the highest pressure.

The ratio of the integrated counting rate under the area of the angle profile to the optimum angle counting rate in the profile gives the angle correction factor.

$$C_a = \frac{\int R^f(\bar{V}^f,\theta)\ d\theta}{R^f(\bar{V}^f,\bar{\theta})} \div \frac{\int R^i(\bar{V}^i,\theta)\ d\theta}{R^i(\bar{V}^i,\ \bar{\theta})} \qquad (4\text{-}13a)$$

and a similar correction factor for the energy profile was obtained from

$$C_v = \frac{f \int R^f(V^f,\ \bar{\theta})\ dV}{R^f(\bar{V}^f,\bar{\theta})} \div \frac{i \int R^i(V^i,\ \bar{\theta})\ dV}{R^i(\bar{V}^i,\ \bar{\theta})} \qquad (4.13b)$$

For no change of either the angle or energy of the ions during their charge-changing processes, both C_a and C_v would be unity. The values for the electron loss cross-section measurements were found experimentally to be slightly above unity, which represents the loss of stripped particles by scattering beyond the acceptance solid angle of the electrostatic analyzer which was set at its optimized configuration $(\bar{V},\ \bar{\theta})$.

For these correction factors near to unity, a linear interpolation between the correction factors obtained at the extreme pressures could be made to correct the optimum counting rate ratios measured at between the extreme pressures. The error of the integrated counting rate of each type of the ions was taken to be that from the root square standard deviation. The error of the optimum counting rate of each type of the ions was estimated by the n-1 weight of the counting fluctuations in the central plateau region of the profile.

A least squares fit was made to obtain the slope of the best linear relation of the ratio R_{12} against pressure P, where the R_{12} ratio, which represents the fractional ratio Y_{12}, is given in this experiment by

$$R_{12} = (R_o^{2+} / R_o^{1+}) C_a \, C_v = Y_{12} \tag{4-14}$$

For the electron capture cross-section measurements, the above correction factors were found experimentally to be very close to unity as expected, so that the effects of angular and energy spreads during the charge-changing processes of the ions could be neglected. The counting rate ratio R_{21} was then simply

$$R_{21} = (R_o^{1+}/R_o^{2+}) = Y_{21} \tag{4-15}$$

Fig.4-1a

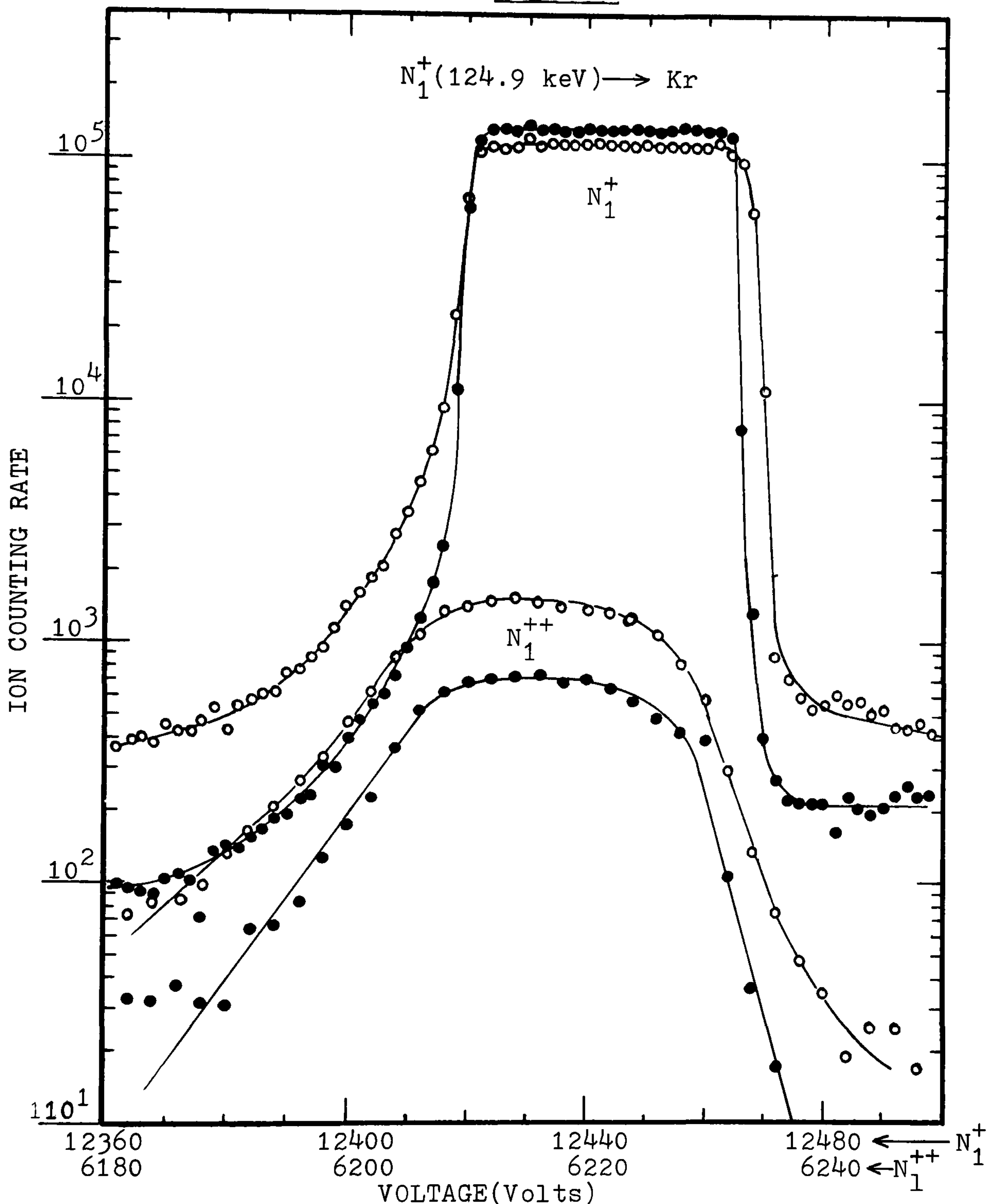

The energy profile of the incident N_1^+ ions and of the charge changed N_1^{++} ions which were obtained by variation of the electrostatic analyzer voltage. The solid cricles were obtained with a target pressure of 1.8×10^{-4} Torr. The open circles were obtained with a target pressure of 9.8×10^{-4} Torr.

Fig.4-1b

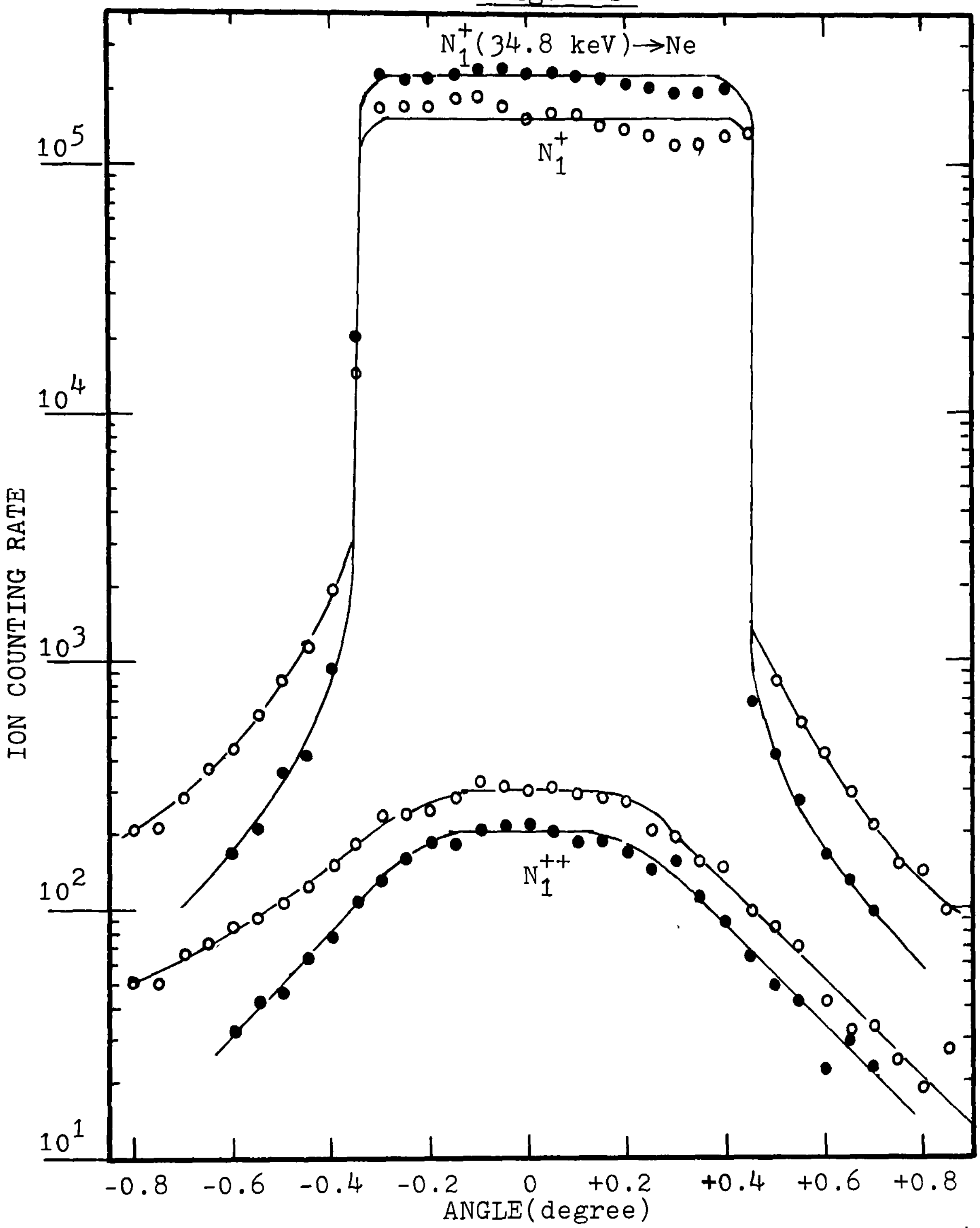

The angle profile of the incident N_1^+ ions and of the charged N_1^{++} ions which were obtained by mechanical rotation of the electrostatic analyzer about the center of the gas target. The solid circles were obtained with a target pressure of 2.8×10^{-4} Torr. The open circles were obtained with a target pressure of 8.6×10^{-4} Torr.

Fig.4-2a

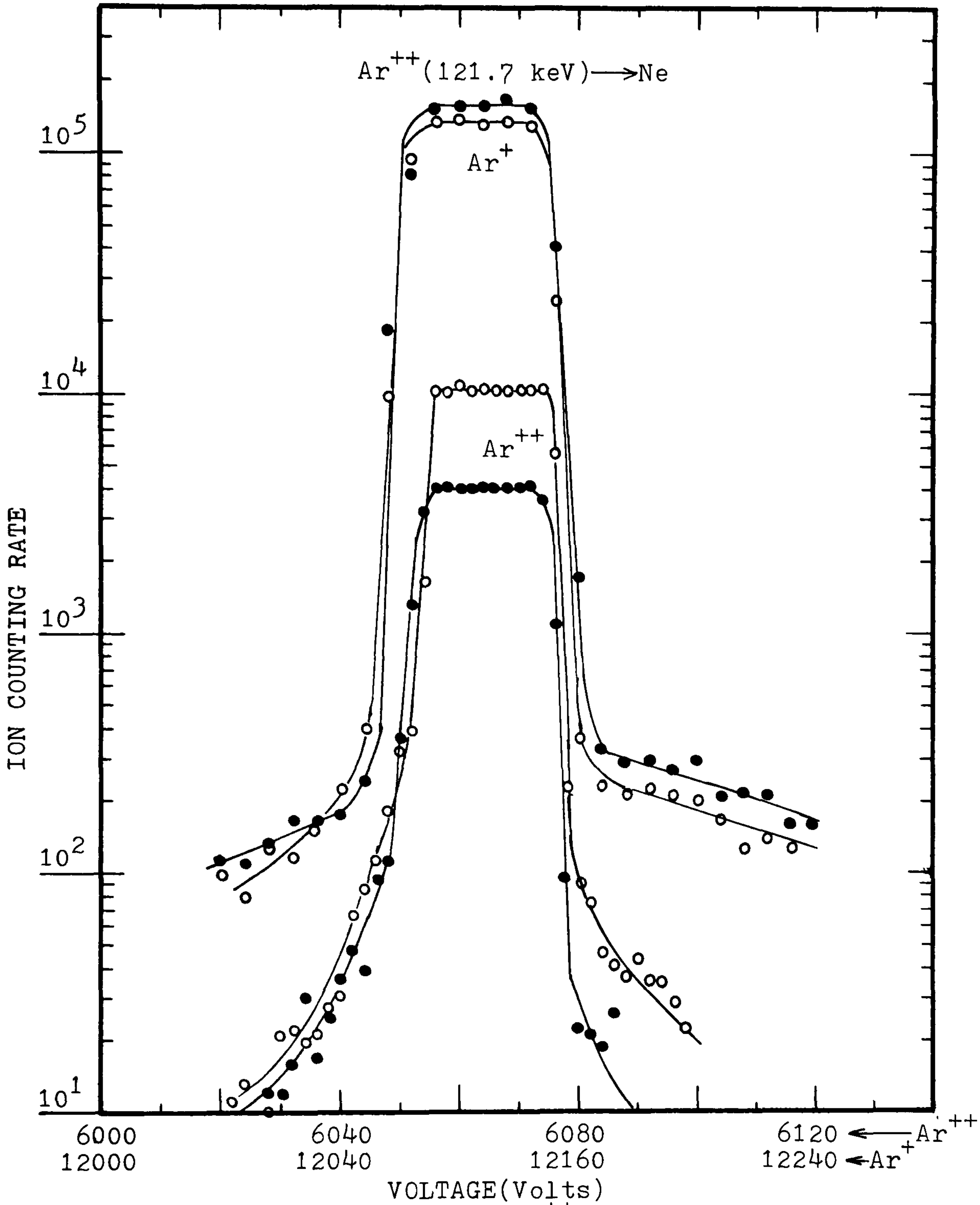

The energy profile of the incident Ar^{++} ions and of the charge changed Ar^{+} ions. The solid circles were obtained with a target pressure of 2.9×10^{-4} Torr. The open circles were obtained with a target pressure of 7.6×10^{-4} Torr.

Fig.4-2b

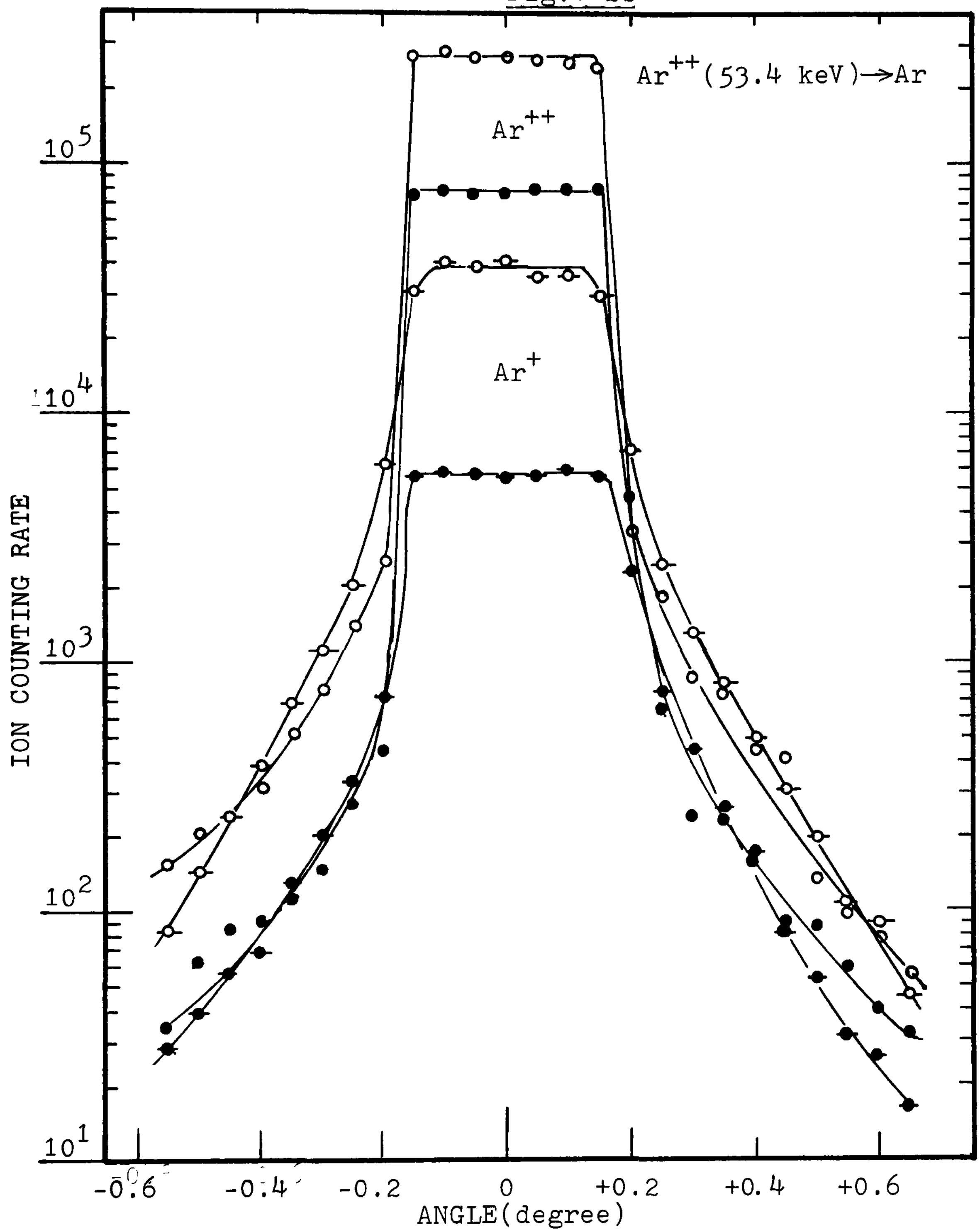

The angle profile of the incident Ar^{++} ions and of the charge changed Ar^{+} ions. The solid circles were obtained with a target pressure of 2.4×10^{-4} Torr. The open circles were obtained with a target pressure of 8.1×10^{-4} Torr.

Fig.4-3

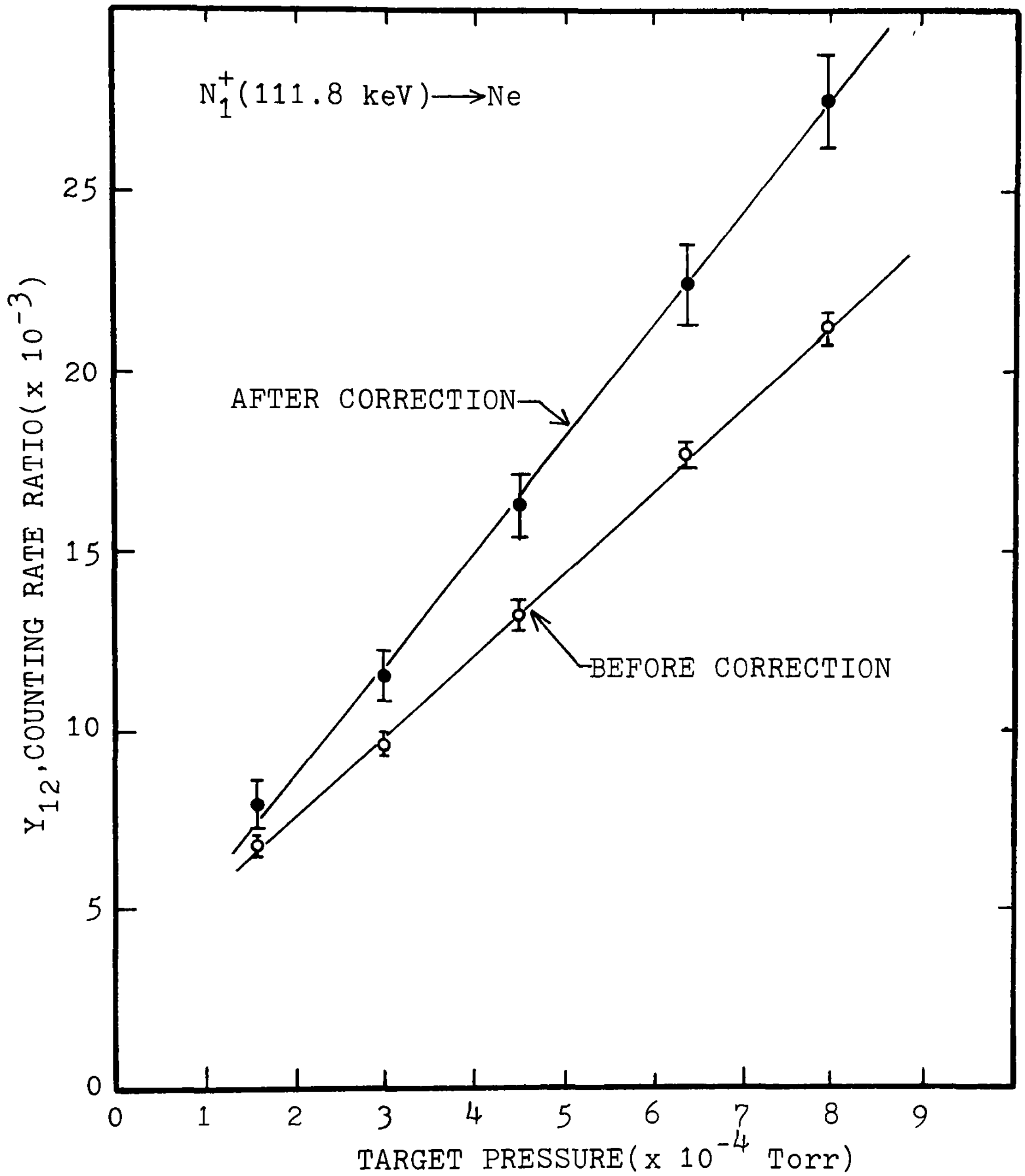

The ratio of charge changed N_1^{++} ions to N_1^+ ions which passed through the gas target, plotted as a function of the target pressure. The ratio after correction for target thickness effects is given by Eq.(5-9).

Fig.4-4

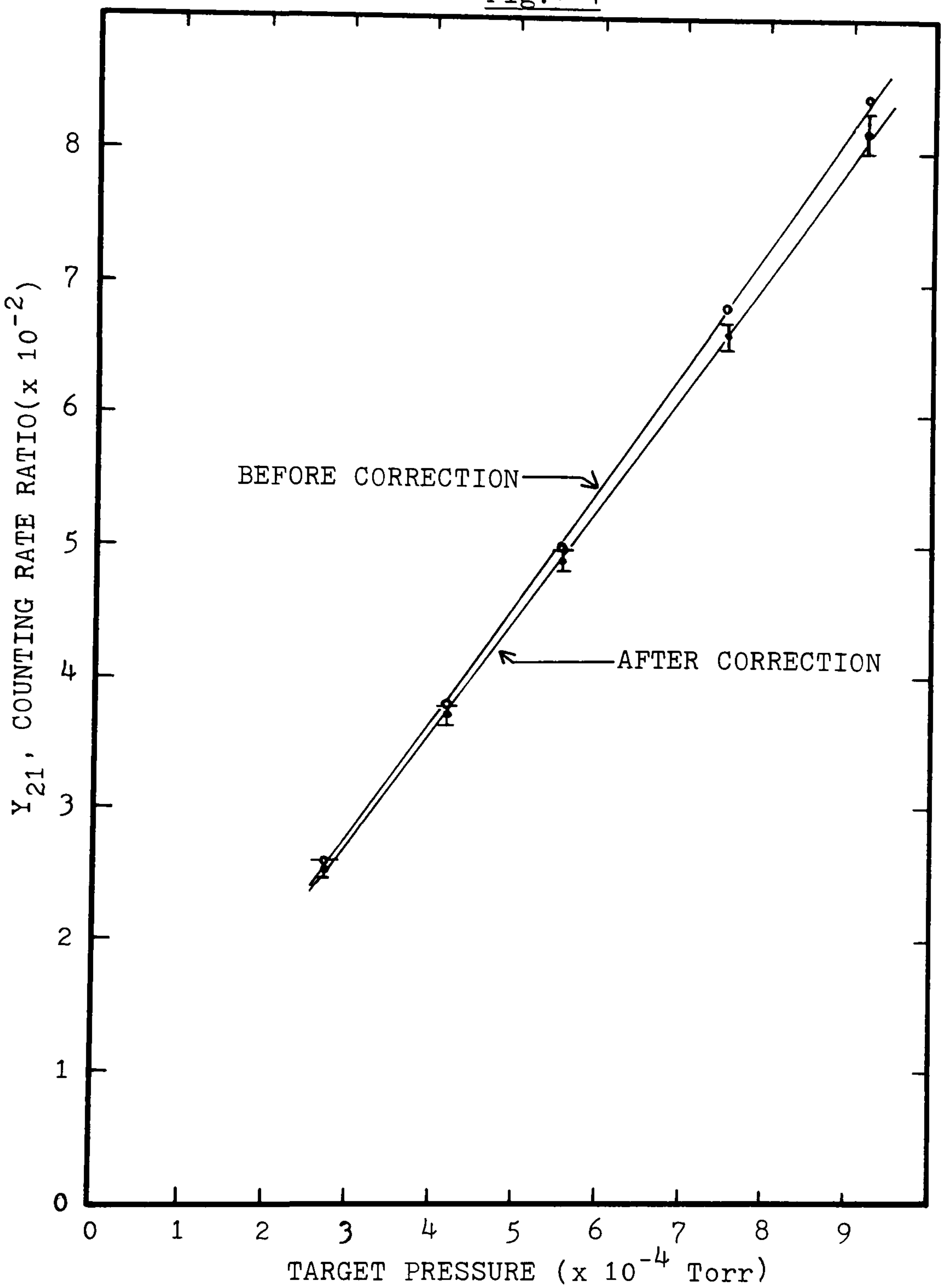

The ratio of charge changed Ar^{+} ions to Ar^{++} ions which passed through the target gas, plotted as a function of the target gas pressure. The ratio after correction for target thickness effects is given by Eq.(5-12).

IV-3 Data analysis and deduction of cross-sections

In the present σ_{12} cross-section measurements, the target thickness π of all the targets of Ne, Ar, and Kr gases was varied in a range of 10^{13} atoms/cm^2 to 10^{14} atoms/cm^2, and the target thicknes π in the present σ_{21} cross-section measurements between 1.3×10^{13} atoms/cm^2 and 7.1×10^{13} atoms/cm^2.

The 6m of the beam line between the 90^o magnetic analyzer and the gas target chamber was kept at a pressure of about 1×10^{-7} Torr. The thickness of residual gas in this beam line was therefore 2×10^{12} atoms/cm^2 which is about 10 times smaller than the lowest target thickness, so that it is a small end effect and is not taken into account even though some charge-changing processes of the ions occurred in the beam line.

The incident beams, consisting of mostly ground state ions, might contain a small proportion of metastable state ions, so that the cross-sections obtained with these ions might be influenced by the presence of metastable state ions in the incident beam. To complicate the situation, no experiment has been made to measure the content of metastable ions in the incident beam. But, no obvious relation between the counting rate ratio in the cross-section measurements and the operating conditions of the ion source was found, so that any long-lived excited ions in the incident beams may be small enough to be neglected, or may be unimportant in the charge-changing cross-section measurements.

The electron loss cross-section σ_{23} in the second-order term in the target thickness π of equation (4-9) is smaller than the others as described in the previous section IV-1, so that the term becomes $-\frac{1}{2}(\sigma_{10} - \sigma_{21})\pi$. The third term is of the second order in π and contains σ_{12} and σ_{23} which are smaller than the others, and the term itself is of quite small value compared with the second term, so that the cross-section σ_{12} and σ_{23} in this third term could be neglected. This third term becomes $1/12\ [4\sigma_{01}\sigma_{10} + (\sigma_{10} - \sigma_{21})^2]\ \pi^2$. For the above target thickness, the terms of the third and higher orders in π could be safely neglected in this experiment, so that the counting rate at each pressure was given by

$$Y_{12}(1 + \tfrac{1}{2}Y_{12})^{-1}\ \{1 - \tfrac{1}{2}(\sigma_{10} - \sigma_{21})\pi + \frac{1}{12}\ [4\sigma_{01}\sigma_{10} + (\sigma_{10} - \sigma_{21})^2]\pi^2\}$$

which was plotted against the target gas pressure, as shown in fig. 4-3, where Y_{12} was experimentally determined using eq. (4-14). The target thickness was determined from the gas pressure measurement, and the cross-sections in the correction terms were taken from the known data listed in Table 4-1.

For the σ_{21} cross-section measurements with the incident Ar^{++} ion beam, the terms of the second and higher order in π of the target thickness correction factor C_{21} given in eq. (4-12) could be safely neglected for the present σ_{21} cross-section measurements. Both the σ_{23} and σ_{12} values in the second term of the first order in π are smaller than the σ_{10} value, so that those values were also neglected. The counting rate ratio at each pressure in the σ_{21} cross-section measurements was given by $Y_{21}(1 + \frac{1}{2}Y_{21})^{-1}\ (1 + \frac{1}{2}\sigma_{10}\pi)$ which was plotted against the given target gas pressure, as shown in fig. 4-4.

Table 4-1

Published cross sections which were used to make the target thickness corrections C_{12}

Incident ion beam energy (keV)	$N_1^+ \longrightarrow Ne$ Cross-sections (x 10^{-15} cm^2)			$N_1^+ \longrightarrow Ar$ Cross-sections (x 10^{-15} cm^2)		
	σ_{01}	σ_{10}	σ_{21}	σ_{01}	σ_{10}	σ_{21}
34.8	0.31	0.24	1.8	0.31	1.5	1.1
49.7	0.32	0.35	1.8	0.33	1.4	1.2
65.0	0.34	0.40	1.8	0.36	1.3	1.2
79.4	0.38	0.45	1.8	0.39	1.2	1.2
94.8	0.40	0.45	1.8	0.42	1.2	1.2
111.8	0.41	0.43	1.8	0.44	1.1	1.2
125.2	0.42	0.43	1.8	0.46	1.0	1.2
139.5	0.43	0.43	1.8	0.48	0.9	1.2

The values of σ_{01} and σ_{10} were obtained by interpolation from the graphical data of Brackmann and Fite[3], using the review article of Lo and Fite[27] where the graphs contain slightly more detail.

The values of σ_{21} were obtained by interpolation from the graphs of Fedorenko[7].

Table 4-2

Published cross sections which were used to make the target thickness corrections C_{21}

Incident io ion beam energy (keV)	$Ar^{++} \longrightarrow Ne$ Cross-section σ_{10} ($\times 10^{-16}$ cm^2)	$Ar^{++} \longrightarrow Ar$ Cross-section σ_{10} ($\times 10^{-16}$ cm^2)	$Ar^{++} \longrightarrow Kr$ Cross-sections σ_{10} ($\times 10^{-16}$ cm^2)
53	1.3	11.0	13.0
70	1.5	10.0	12.0
92	1.7	8.6	11.2
112	1.9	7.3	10.8
132	2.1	6.4	10.0
152	2.1	6.0	9.0
171	2.0	5.4	8.0
192	1.8	5.2	7.0

The values of σ_{21} were obtained by interpolation from the graphs of Wittkower and Gilbody[38].

Table 4-2 shows the σ_{10} cross-sections which were used to make the target thickness correction C_{21}. The σ_{21} cross section was obtained also by the weighted least squares fitting to the data points.

The error of the present experimental cross-section represents the standard deviation which was determined by the method described in the following section V-4. The error of each point on those corrected lines takes account of only the statistical random error of the ratio. No account was taken of the error of the pressure.

V-4 A weighted least squares fitting of a straight line

A method is given for computing the best straight line and its error by least squares when there are statistical random errors in one of two coordinates. In the present measurements, one coordinate is subjected only to the statistical random error of the counting rate ratio. The other may be subjected to the systematic error from the pressure gauge, but this error was not taken into account.

The experimental data are considered as pairs of points (x_i, y_i) where i runs from 1 to m and the measurements have only one variance $\mathrm{Var}(y_i) = \sigma_i^2$, whereas the corresponding value x_i is assumed to be known precisely. Assuming that the measurement of y locates it within a small interval of extend δy, the probability of observing the value y_1 is

$$P(y_1) = \sigma_1^{-1} \quad (2\pi)^{-1} \quad \exp[\, -(y_1 - A - Bx_1)^2/2\sigma_1^2]$$

from the normal distribution. Similarly, the expression holds for $P(y_2), \ldots\ldots, P(y_m)$, where m is the number of data points or observations. The total probability, P_t, of all the values of y_i occurring simultaneously is proportional to

$$\exp\left[- \sum_{i=1}^{m} (y_i - A - Bx_i)^2 / 2\sigma_i^2 \right]$$

and the maximum probability will occur when A and B are chosen to minimize the sum of squares:

$$S = \sum_{i=1}^{m} (y_i - A - Bx_i)^2 / (2\sigma_i^2) \tag{4-16}$$

For S to be a minimum, dS/dA = 0, and also dS/dB = 0, which give

$$\sum_{i=1}^{m} w_i (y_i - A - Bx_i) = 0 \tag{4-17}$$

$$\sum_{i=1}^{m} w_i (y_i - A - Bx_i) x_i = 0 \tag{4-18}$$

where $w_i = \sigma_i^{-2}$. From these two equations, one can obtain the slope B in the form

$$B = \sum_{i=1}^{m} w_i x_i' y_i' / (\sum_{i=1}^{m} w_i x_i'^2) \tag{4-19}$$

where the new coordinates x_i' and y_i' are defined:

$$x_i' = x_i - \overline{x} \tag{4-20}$$

$$y_i' = y_i - \overline{y} \tag{4-21}$$

with

$$\overline{x} = \sum_{i=1}^{m} w_i x_i / \sum_{i=1}^{m} w_i \tag{4-22}$$

$$\overline{y} = \sum_{i=1}^{m} w_i y_i / \sum_{i=1}^{m} w_i \tag{4-23}$$

Since the variance of y_i' in the above equations has also the variance σ_i^2 and the slope B of eq. (4-19) it is expressable as a sum of terms in σ_i, the standard formula for error propagation in a sum can be used:

$$B \pm \sigma_B = \frac{\sum_{i=1}^{m} w_i x_i' y_i'}{\sum_{i=1}^{m} w_i x_i'^2} \pm \left\{ \frac{(w_1 x_1' \sigma_1)^2}{(\sum_{i=1}^{m} w_i x_i'^2)^2} + \ldots + \frac{(w_m x_m' \sigma_m)^2}{(\sum_{i=1}^{m} w_i x_i'^2)^2} \right\}^{\frac{1}{2}} \tag{4-24}$$

so that the variance σ_B^2 of the slope B is given by

$$\sigma_B^2 = \sum_{i=1}^{m} (w_i x_i' \sigma_i)^2 / (\sum_{i=1}^{m} w_i x_i'^2)^2 = (\sum_{i=1}^{m} w_i x_i'^2)^{-1} \tag{4.25}$$

A convenient form of the fractional error can be made by substituting eq. (4-25) into eq. (4-19) as

$$\sigma_B / B = [(\sum_{i=1}^{m} w_i x_i^2) / (\sum_{i=1}^{m} w_i x_i' y_i')^2]^{\frac{1}{2}} \tag{4-26}$$

By similar considerations to the above, the intercept A and its variance σ_A are given by

$$A = \bar{y} - B\bar{x} \tag{4-27}$$

and

$$\sigma_A^2 = (\sum_{i=1}^{m} w_i)^{-1} + \bar{x}^2 \sigma_B^2 \tag{4-28}$$

CHAPTER V RESULTS AND DISCUSSION

V-1 Experimental Results

In the present study, the electron loss cross-sections σ_{12} for the N_1^+ ions on the gas targets of Ne, Ar, and Kr in the ion energy from 30 keV to 150 keV are presented in Table 5-1 and figs. 5-1, 5-2, and 5-3, respectively. The single electron capture cross-sections σ_{21} for the Ar^{++} ions on the above targets in the ion energy range between 50 keV and 200 keV are presented in Table 5-2 and figs. 5-4, 5-5, and 5-6, respectively. In the figures, the data from other investigators is also shown where it exists.

V-1A The single electron loss cross-sections[1]

A-1 The σ_{12} cross-section of N_1^+ in Ne.

The σ_{12} cross-section data for the $N_1^+ \rightarrow$ Ne collisions, as a function of the ion energy, are listed in Table 5-1 and shown in fig. 5-1. The total correction of the angular and energy spreads, which gradually decreases with increasing ion-energy, was about 5% at the lowest energy and about 1% at the highest energy. The target thickness correction was about 12% at the lowest energy, and decreased slightly to about 11% at the highest energy, so that the target thickness corrections for the collision in the present ion energy range are more important than both the corrections of the angular and energy spreads.

The previous measurements by Brackmann and Fite[3] are shown also in fig. 5-1, where their cross-section at the lowest energy appears to be slightly small compared with that of the present measurements, but their data above 70 keV are about half those of the present data. The present data provide a better extrapolation to the data by Pivovar et al[4] at 350 keV and higher energies of the ions.

A-2 The σ_{12} cross-section of N_1^+ in Ar

Table 5-1 and fig. 5-2 show the present data of σ_{12} for the collisions between N_1^+ ions and Ne gas, as a function of the ion energy. The total corrections of the angular and energy spreads were about 14% at the lowest energy and about 4% at the highest energy. As shown in Table 4-1 of Chapter IV, the cross-section σ_{01}, which was used to make the target thickness corrections in the σ_{12} cross-section measurements, gradually increases with increasing ion-energy, where the cross-section σ_{10} gradually decreases with increasing energy. The change in the σ_{12} cross-section due to these opposite sign corrections of target thickness was then about -5% at the lowest energy and about 4% at the highest energy, so that the target thickness correction was about zero near 80 keV.

Fig. 5-2 shows also the previous data of Brackamnn and Fite[3]. Their data at the low energies appear to be slightly large compared with that of the present measurements, but their data at 120 keV is about 1.5 times smaller than the present data. Here, it is noted that the energy at which the target thickness correction passes through zero is also the energy at which the present data would provide an interpolation between the data of Brackmann and Fite[3]. As was found in the $N_1^+ \rightarrow$ Ne collisions, the present data for this Ar target provide a better extrapolation to the data of Pivovar et al[4].

A-3 <u>The σ_{12} cross-section of N_1^+ in Kr</u>

In the present ion energy range, the data on the single electron loss cross-sections for the $N_1^+ \rightarrow$ Kr collisions are shown as a function of the ion energy in fig. 5-3 and also in Table 5-1. No other measurements on the cross-sections σ_{10}, σ_{01}, or σ_{21} for the target thickness corrections exist, so that the corrections of the first and higher orders in the target thickness could not be made. Over most of the ion energy range, these corrections in the σ_{12} measurements amount to approximately $-4.4(\sigma_{10} - \sigma_{21}) \times 10^{14}$ where the cross-sections σ_{10} and σ_{21} are in units of cm^2. Taking into account the experimentally measurable quantities, about 0.1% of the incident ion beam over the ion energy range lost an electron in passing through the target. The total corrections of the angular and energy spreads were about 11% at the lowest energy and about 5% at the highest energy, so that the correction decreased with increasing ion energy.

No other measurements exist to directly compare with the present data. The present data can be linearly extrapolated to agree with the data of Pivovar et al[4] above 250 keV.

For all the collisions of N_1^+ ions with the above three targets, it is confirmed that the cross-sections monotonically rise with increasing ion energy. In the relative ordering of the σ_{12} cross-sections for the one species of N_1^+ ions in the different targets of Ne, Ar, and Kr at a given ion energy, the cross-section for the Ne target is larger than that for the other targets. The cross-section for the Ar target lies somewhere between the other two data, so that σ_{12} cross-sections are found to increase as the target mass or atomic number decreases. The slight inflection, which is seen in the Ne target at the highest energies, is not statistically significant. The $N_1^+ \rightarrow$ Ne collision cross-section, which is much larger than the other two at the lowest energies, increase only 2.5 times through the present ion energy range, whereas the other two cross-sections increase proportionately by more than twice this ratio. There is some qualitative indication from the angle correction factors that the mean scattering angle in the σ_{12} cross-sections for the Ne target decreases more rapidly with increasing ion energy than that for either the Ar or Kr target.

Discrepancies are found in the previous data from the different groups[3,4,5]. These discrepancies may be explainable in terms of the angular spread of the ions. The angular spread in the present measurements is significant even at the highest ion energies, where several percent of the ions are scattered beyond the angle of 0.7^{o}, so that the data from the present measurements are large compared with those from Brackmann and Fite[3]. The data from Pivovar et al[4] who measured the integrated cross-sections above 350 keV are also larger than the data from Brackmann and Fite[3] or from Dimitriev et al[5]. The other main source of error in the previous data may be the failure of the single collision approximation, probably because no account has been taken of multiple collisions. The presence of N_2^{++} in the N_1^+

Table 5-1

Single electron loss cross sections σ_{12} for N_1^+ ions

$N_1^+ \longrightarrow Ne$			$N_1^+ \longrightarrow Ar$			$N_1^+ \longrightarrow Kr$		
Incident ion beam		Cross-section σ_{12} ($\times 10^{-17} cm^2$)	Incident ion beam		Cross-section σ_{12} ($\times 10^{-17} cm^2$)	Incident ion beam		Cross-section σ_{12} ($\times 10^{-17} cm^2$)
Energy (keV)	FWHM (keV)		Energy (keV)	FWHM (keV)		Energy (keV)	FWHM (keV)	
34.8	0.14	6.17 ± 0.58	34.8	0.16	1.33 ± 0.28	32.9	0.12	0.89 ± 0.32
49.9	0.12	7.42 ± 0.56	50.0	0.21	2.70 ± 0.42	48.9	0.20	1.89 ± 0.34
64.9	0.26	10.83 ± 0.85	64.5	0.25	3.12 ± 0.47	66.8	0.32	2.43 ± 0.31
79.4	0.36	11.40 ± 1.20	82.2	0.32	5.73 ± 1.08	79.4	0.34	2.74 ± 0.46
94.8	0.40	12.80 ± 1.36	96.6	0.46	6.92 ± 0.97	96.7	0.38	3.49 ± 0.51
111.8	0.46	14.96 ± 0.88	111.1	0.44	8.82 ± 0.79	111.9	0.48	4.33 ± 0.58
125.2	0.52	14.53 ± 1.04	127.0	0.52	9.53 ± 0.60	124.9	0.48	5.40 ± 0.54
139.3	0.53	15.47 ± 2.17	139.9	0.56	10.70 ± 0.87	139.9	0.56	5.78 ± 0.48

Fig. 5-1

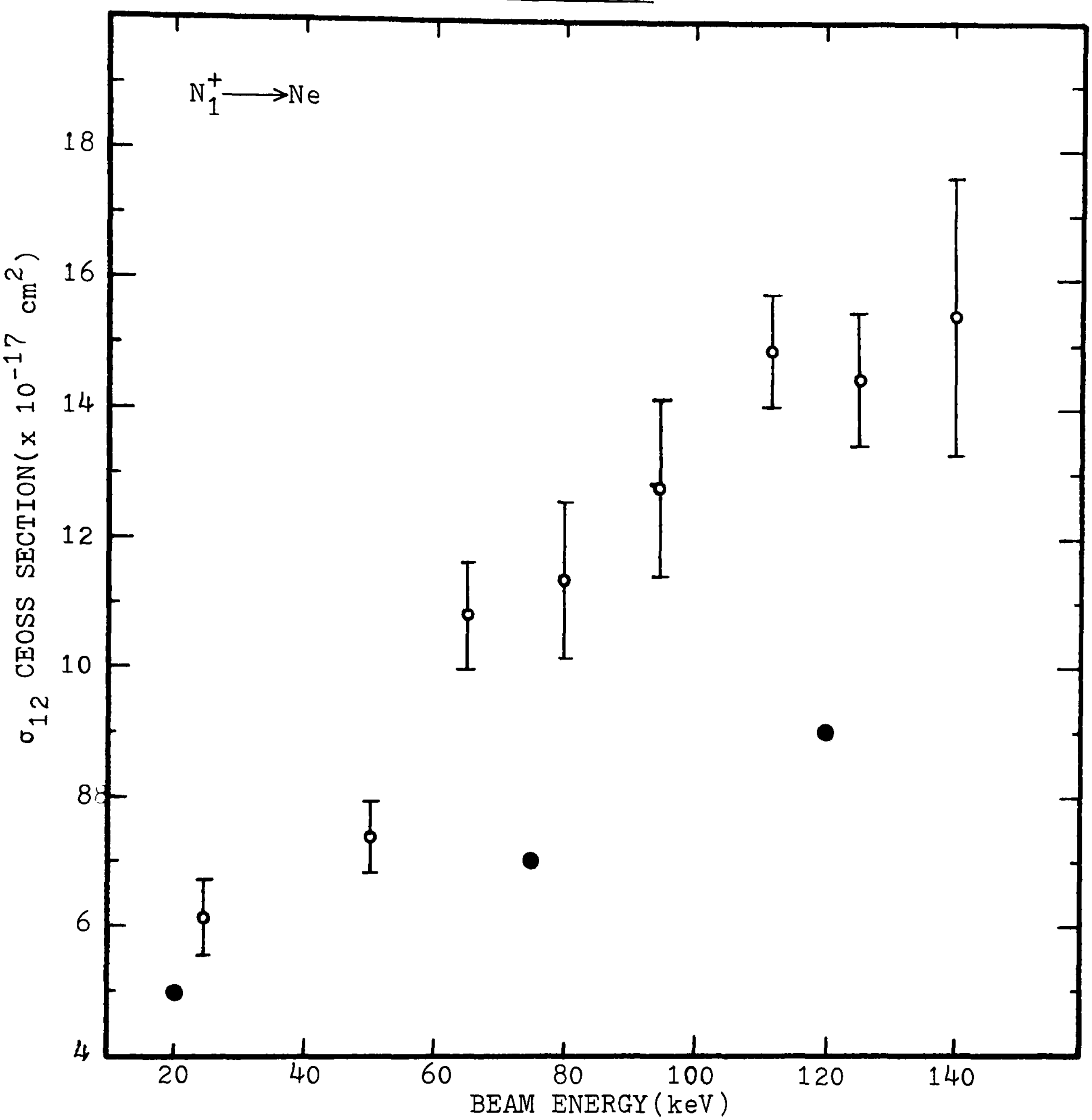

The single electron loss cross section for N_1^+ ions in Ne. The solid cricles are the data of Brackmann and Fite[3].

Fig.5-2

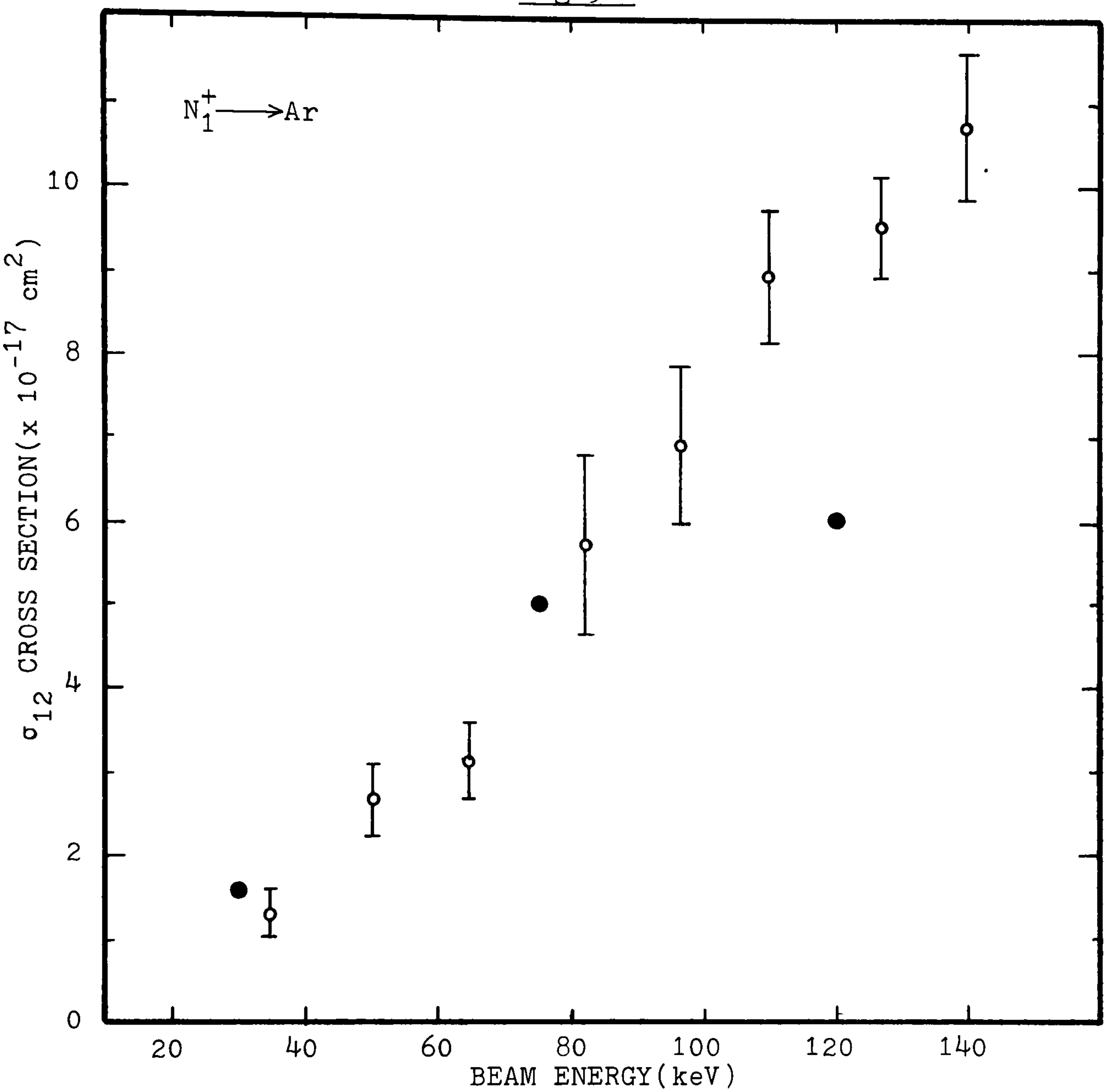

The single electron loss cross section for N_1^+ ions in Ar. The solid circles are the data of Brackmann and Fite[3].

Fig.5-3

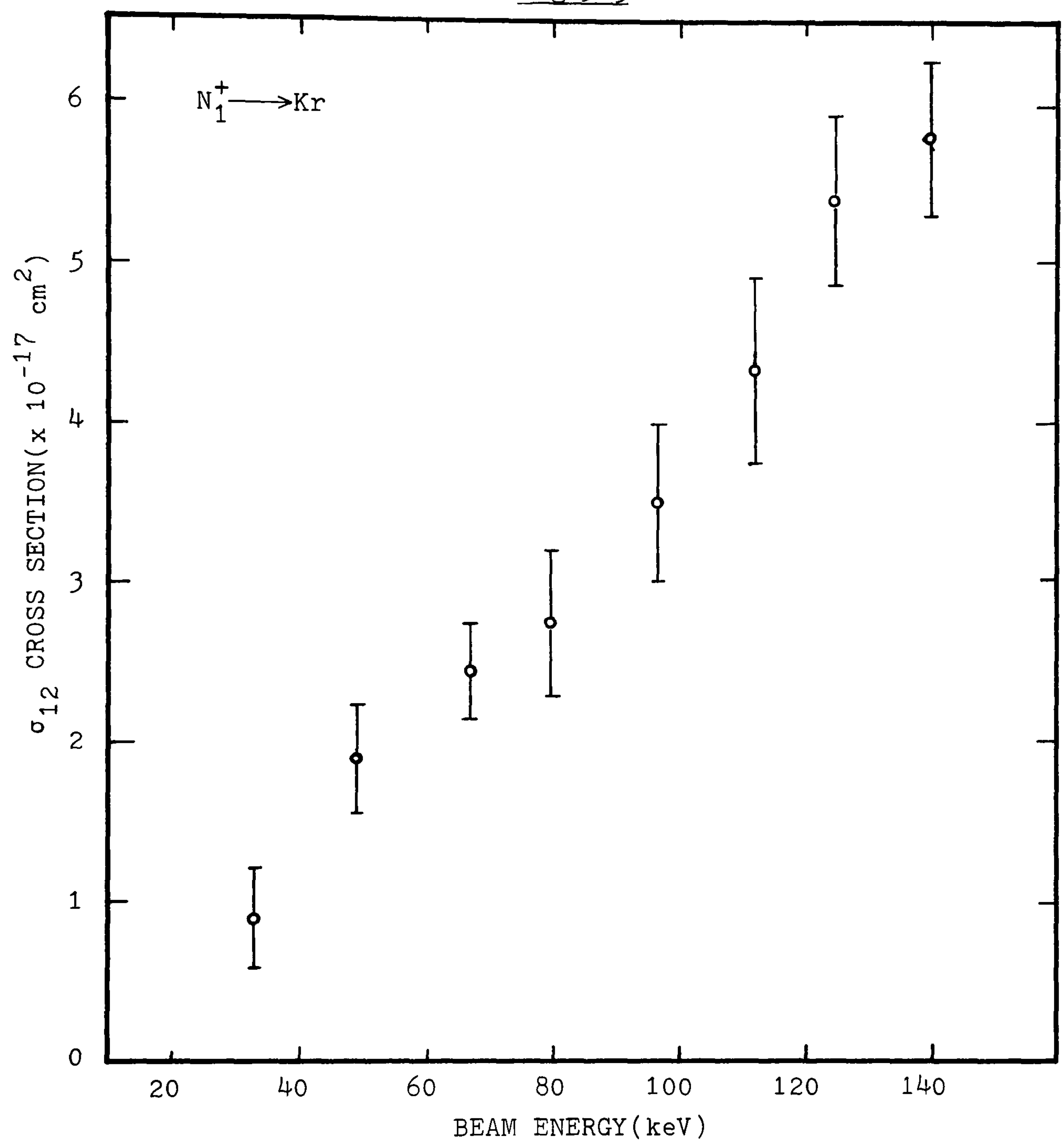

The single electron loss cross section for N_1^+ ions in Kr.

ion beam may cause experimental error, but no mention has been made of the N_2^{++} impurity in the previous measurements.

V-1B The single electron capture cross-sections

B-1 <u>The σ_{21} cross-section of Ar^{++} in Ne</u>

The results of the σ_{21} cross-section measurements on the $Ar^{++} \rightarrow$ Ne collisions, as a function of the ion energy, are shown in fig. 5-4 and listed in Table 5-2. The target thickness corrections were quite small; less than 1% over the energy range.

At the present lowest ion energies, Flaks and Solov'ev[6] and Fedorenko[7] had measured the σ_{21} cross-sections shown in fig. 5-4. The data of Flaks and Solov'ev[6] are much larger by a factor of about 40% than the present data. The data of Fedorenko[7] have slightly larger absolute magnitudes compared with the present data, but there is agreement within experimental error.

B-2 <u>The σ_{21} cross-section of Ar^{++} in Ar</u>

The σ_{21} cross-section data of Ar^{++} in Ar, as a function of the ion energy, are shown in fig. 5-5 and listed in Table 5-2. The target thickness corrections were less than 2% over the ion energy range.

The data of both Flaks and Solov'ev[6] and Fedorenko[7] are also shown in fig. 5-5, which at the present lowest energies are smaller by a factor of 35% than the present data. The present data provide a good extrapolation to the data of Klinger et al[8] who measured with thinner targets of the order of some 10^{10} atoms/cm^2 to 10^{12} atoms/cm^2 over the ion energy range between 10 keV and 40 keV.

B-3 The σ_{21} cross-section of Ar^{++} in Kr

Figure 5-6 and Table 5-2 show the experimental results of the σ_{21} cross-section measurements of Ar^{++} in Kr, as a function of the ion energy. The target thickness corrections were slightly greater than 1% over the ion energy range.

Figure 5-6 also shows the data of Fedorenko[7] which are smaller by a factor of about 10% than the present data at the lowest energies.

The σ_{21} cross-section for each of the collisions with the three targets is found to pass through a maximum which is 1.33×10^{-15} cm^2 at 95 keV for the Ne target, 1.46×10^{-15} cm^2 at 170 keV for the Ar target, and 1.65×10^{-15} cm^2 at 170 keV for the Kr target. In the $Ar^{++} \rightarrow$ Ne collisions the variation of the cross-section with the ion energy is large compared with that for the other two targets. The σ_{21} cross-sections for the Kr target are found to be slightly larger than those for the Ar target over the ion energy range, but the general trend in the energy dependence of the cross-sections is the same for the two targets. No obvious quantitative relation between the cross-section and the atomic number or target mass is found in either the energies of the cross-section maxima or the relative ordering of the cross-sections between the three targets at a given ion energy.

No angular or energy spread correction was found to be necessary in any of the present capture cross-section measurements. Effectively, all the ions could be detected within the angle spread of about 1^{o} arc. In all the cross-section measurements, the target thickness corrections did not exceed 2%.

Table 5-2

Single electron capture cross sections σ_{21} for Ar^{++} ions

$Ar^{++} \longrightarrow Ne$			$Ar^{++} \longrightarrow Ar$			$Ar^{++} \longrightarrow Kr$		
Incident ion beam		Cross-section σ_{21} ($\times 10^{-16} cm^2$)	Incident ion beam		Cross-section σ_{21} ($\times 10^{-16} cm^2$)	Incident ion beam		Cross-section σ_{21} ($\times 10^{-16} cm^2$)
Energy (keV)	FWHM (keV)		Energy (keV)	FWHM (keV)		Energy (keV)	FWHM (keV)	
54.0	0.36	9.93 ± 0.37	53.4	0.22	7.49 ± 0.47	52.2	0.16	7.80 ± 0.11
66.7	0.44	10.34 ± 0.16	72.7	0.30	10.33 ± 0.57	72.2	0.28	11.01 ± 0.27
80.2	0.36	11.71 ± 0.32	93.7	0.38	11.30 ± 0.88	92.5	0.48	11.24 ± 0.19
96.3	0.40	13.25 ± 0.42	113.3	0.46	13.27 ± 0.37	112.8	0.44	12.69 ± 0.34
100.2	0.40	12.59 ± 0.42	132.1	0.56	13.96 ± 0.16	132.7	0.52	13.39 ± 0.48
121.7	0.52	9.90 ± 0.24	152.2	0.60	14.54 ± 0.38	153.2	0.58	15.85 ± 0.29
147.4	0.68	9.61 ± 0.34	172.4	0.76	14.35 ± 0.46	171.5	0.66	16.44 ± 0.81
168.9	0.73	10.77 ± 0.30	192.1	0.80	14.03 ± 0.56	193.0	0.73	15.86 ± 0.41
190.4	0.82	9.42 ± 0.68						

Fig.5-4

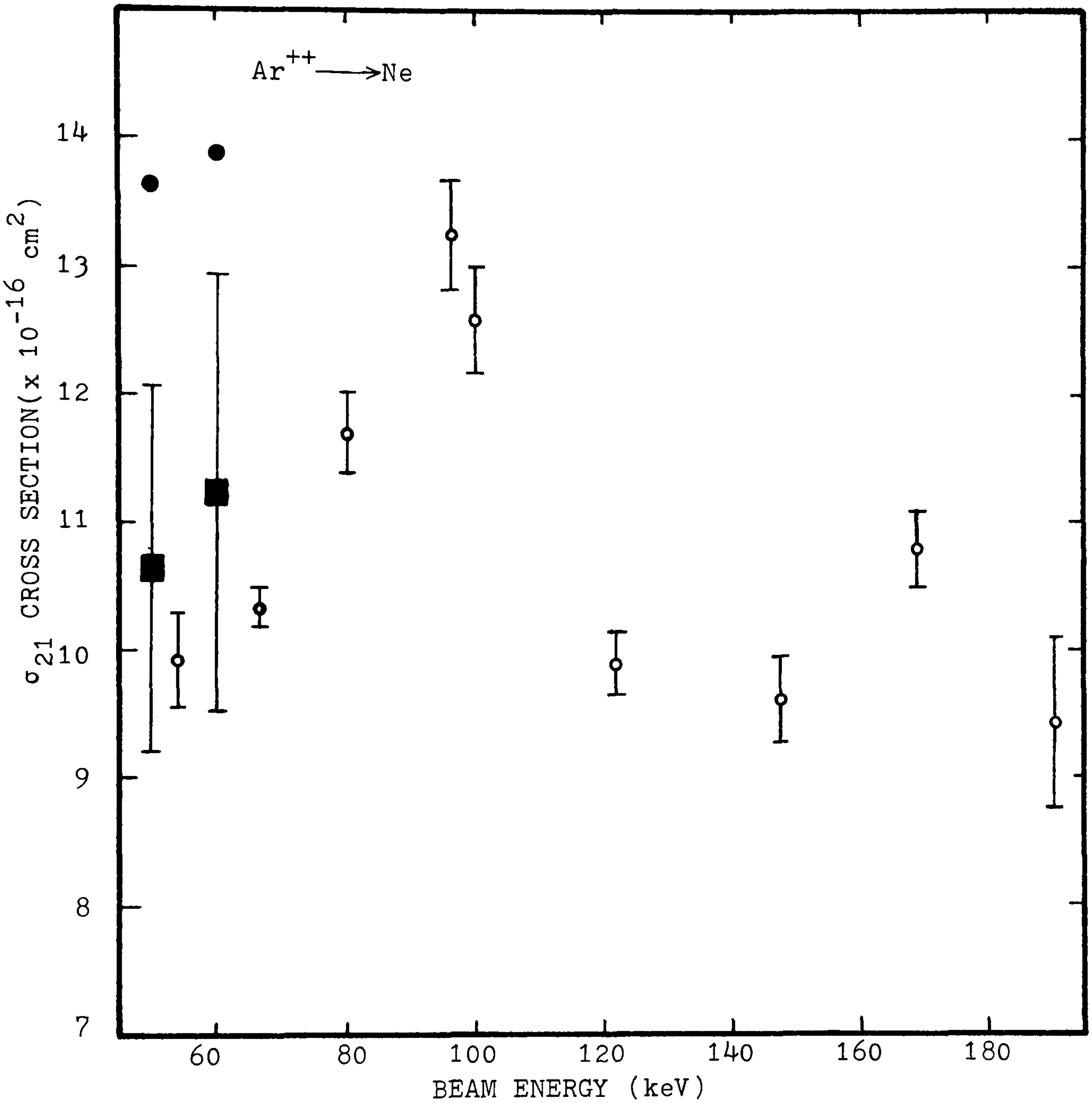

The single electron capture cross section for Ar^{++} ions in Ne.
The solid circles are the data of Flaks and Solov'ev[6].
The solid squares are the data of Fedorenko[7].

Fig. 5-5

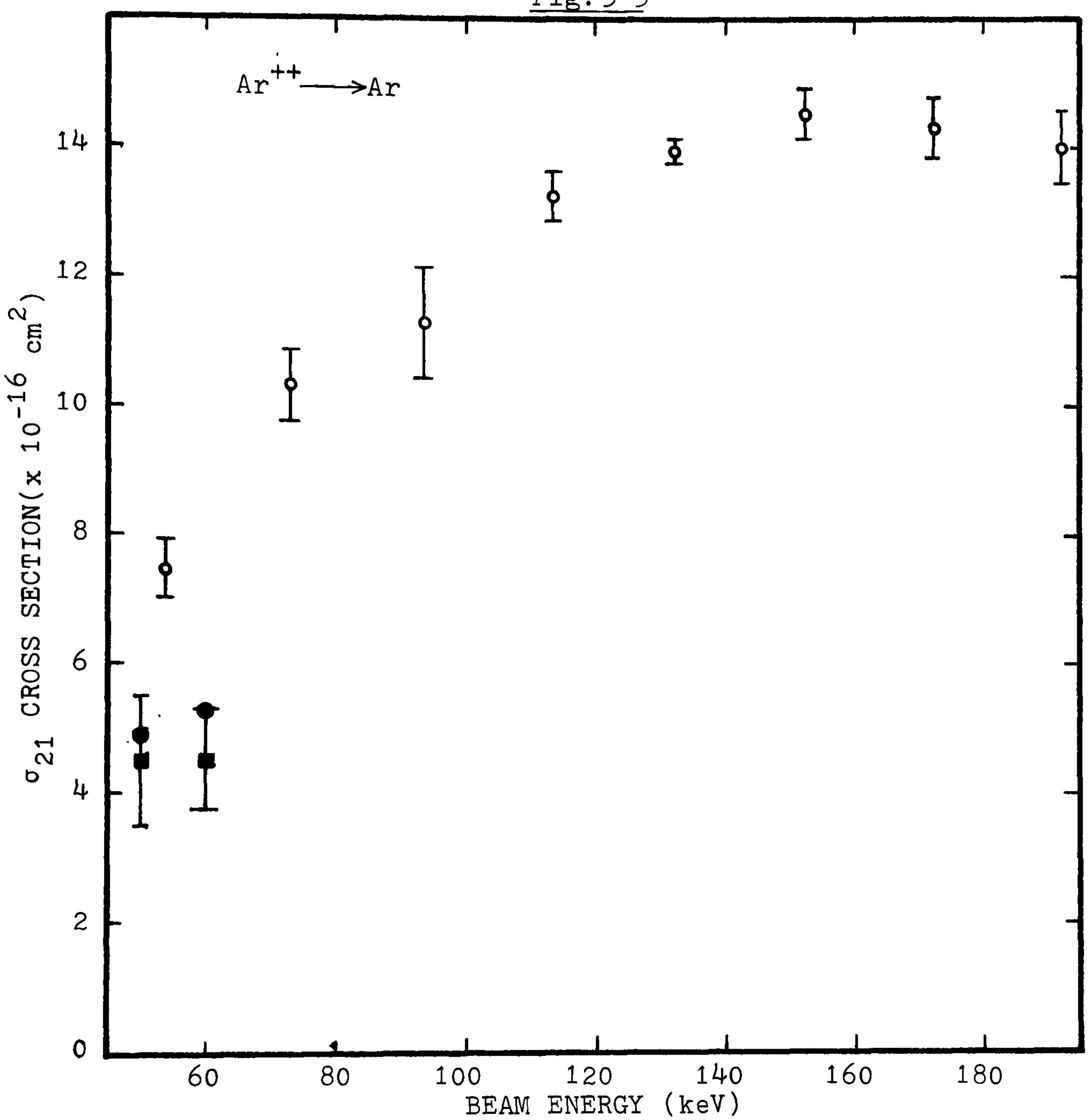

The single electron capture cross section for Ar^{++} ions in Ar.
The solid circles are the data of Flaks and Solov'ev[6].
The solid squares are the data of Fedorenko[7].

Fig. 5-6

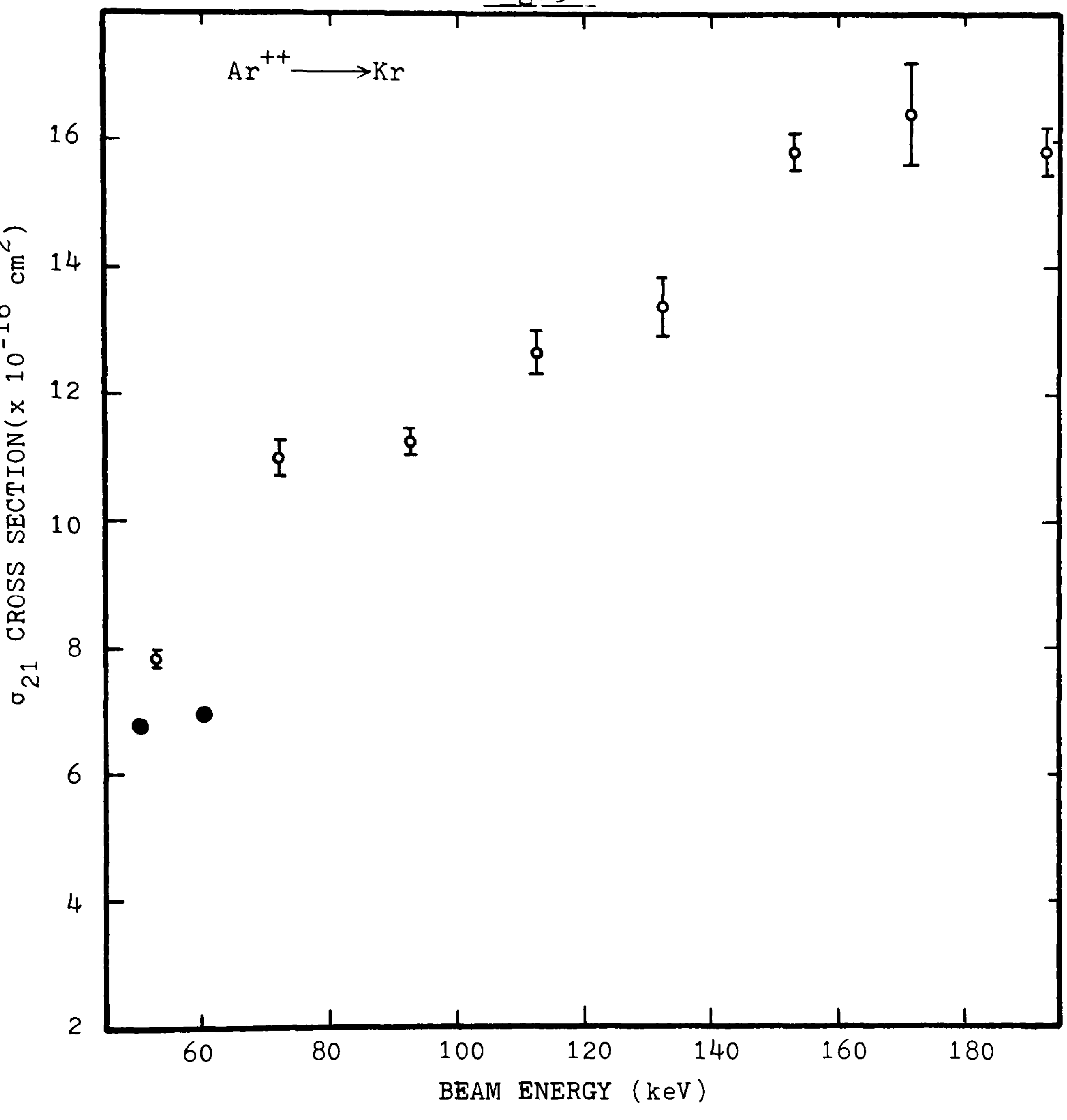

The single electron capture cross section for Ar^{++} ions in Kr.
The solid circles are the data of Flaks and Solov'ev[6].

In general, the early data of both Flaks and Solov'ev[6] and Fedorenko[7] are found to disagree considerably with the present data and with the data of Klinger et al.[8].

V-11 Comparison with theory

The present asymmetric charge transfer cross-sections $\sigma_{12}(N_1^+)$ and $\sigma_{21}(Ar^{++})$ were compared with the predictions of the two-state theory[9-12], assuming that only the ground states of the reactant and product particles were involved.

The energy defects Q for the present σ_{12} single electron loss collisions are listed in Table 5-3. The possibility of excited state ions including the initial and final metastable ions was ignored because, in the endothermic collisions, low excitations are favoured for the final states. The Q_∞ values were therefore determined from the ionization potential 29.6 eV of N_1^+, and the recoil atoms of the Ne, Ar, and Kr rare gases were assumed to have the transferred electrons which were slightly unbound or bound by the small electron affinity if the negative ions exist. The two products are both charged, so that the corrected energy defects Q_c can be estimated by subtracting the Coulomb attraction energy in the final states from Q_∞. The σ_{12} collisions are therefore less endothermic due to the Coulomb effects.

The present σ_{21} electron capture collisions all have Q_∞ energy defects which are exothermic. They are also listed in Table 5-3. Both the product particles are again charged, but for these collisions the Coulomb energies are repulsive and it has the effect of reducing

Table 5-3*

Energy defects Q_∞ and Q_c for the impact of N_1^+ ion on a target B in the process of $N_1^+(^3P)+B(^1S) \longrightarrow N_1^{++}(^2P)+B^-(?)$, and for the impact of Ar^{++} ion on a target B in the process of $Ar^{++}(^3P)+B(^1S) \longrightarrow Ar(^2P)+B(^2P)$, where B=Ne, Ar, or Kr.

Q(eV)	B(Target) / Projectile	Ne	Ar	Kr
Q_∞	N_1^+	-29.6	-29.6	-29.6
Q_c		-11.3	-13.5	-15.9
Q_∞	Ar^{++}	+6.1	+11.9	+13.1
Q_c		-1.7	+4.8	+6.9

* All the reactants and products are assumed to be in their ground states.

The electron affinity of B^- was assumed to be zero.

"-" and "+" signs refer to the endothermic and exothermic collisions, respectively.

All data were estimated by using C. E. Moore, Atomic Energy Levels, Circular of the National Bureau of Standards 467, (1952) the Q_c corrected energy defects in the $Ar^{++} \rightarrow Ar$ and $Ar^{++} \rightarrow Kr$ collisions. In the $Ar \rightarrow Ne$ collision the Coulomb correction is large enough to make the corrected energy defect Q_c endothermic.

The predictions of the Hasted and Lee empirical abiabatic maximum rule[12], $X_a(\mathring{A}) = 0.5745\ [E_{max}(ev)/M(amu)]^{\frac{1}{2}}\ /\ Q(eV)$, for the laboratory energy E_{max} of a projectile with mass M at which the cross-section passes through a maximum are shown in Table 5-4, using the energy defects of Table 5-3. It appears that the energies of the σ_{12} cross-section maxima are beyond the present ion energy range, and so they can not be compared with the present data. Previous experimental data[27] has established these maxima at about 500 keV for the Ne target, about 1000 keV for the Ar target, and about 1500 keV for the Kr target, which confirm the theoretical energy ordering, but are significantly higher energies than predicted. Also the rule[12] agrees well with the relative energy ordering of the σ_{21} experimental cross-section maxima between the three targets. Using the observed energies of the σ_{21} cross-section maxima in this experiment, the adiabatic parameter X_a is estimated as $X_a = 16.4\ \mathring{A}$ for the Ne target, $X_a = 7.4\ \mathring{A}$ for the Ar target, and $X_a = 5.5\ \mathring{A}$ for the Kr target. The latter two values of X_a are quite close to the $X_a = 7\ \mathring{A}$ per unit transferred electron of Hasted and Lee[12].

The two-state asymmetric charge exchange cross-section theory was used in the approximation of eq. (2-40) of Chapter II, developed by Rapp and Francis[9], so that $\sigma_a(b, v) = s\frac{1}{2}\pi\, b_1^2\, \Phi(u_1)$, where the definition of Lee and Hasted[10] for b_1 was used.

The statistical weighting factor s is unity for all the present

Table 5-4

Energies of Cross-section Maxima (Adiabatic Maximum Rule)

Method	Q	Energy(keV)					
		$\sigma_{12}(N_1^+ \rightarrow Ne)$	$\sigma_{12}(N_1^+ \rightarrow Ar)$	$\sigma_{12}(N_1^+ \rightarrow Kr)$	$\sigma_{21}(Ar^{++} \rightarrow Ne)$	$\sigma_{21}(Ar^{++} \rightarrow Ar)$	$\sigma_{21}(Ar^{++} \rightarrow Kr)$
Hasted & Lee[12]	Q_∞	1748	1748	1748	218	835	1013
	Q_c	226	376	527	17	135	280
Rapp & Francis[9]	Q_c	280	340	390	45	205	335
Experimental Data	-	≈550*	≈1000*	≈1500*	≈95**	≈150**	≈170**

* The energies were obtained from the reference[27].

**The energies were obtained from the present results.

σ_{12} collisions if it can be assumed that final molecular states are available with the possible $^3\Sigma^-$ and $^3\pi$ states of the initial $[N_1^+(^3P_o)B(^1S_o)]$ system. The binding of the transferred electron to the target atom has been neglected in the calculations, so that the uncorrected energy defects Q_∞ listed in Table 5-3 and the mean ionization potentials in this theory are the same for the different targets of Ne, Ar, and Kr. This simple theory is therefore unable to account for the considerable differences in the experimental cross-sections σ_{12} between the three targets, when using the uncorrected energy defects Q_∞. Using the corrected energy defects Q_c listed in Table 5-3, the theoretical cross-sections σ_{12} were computed as shown in fig. 5-7. A measure of the quality of the theoretical fit may be obtained by calculating $(\sigma_{th}/\sigma_{exp})_{max}$ and $(\sigma_{th}/\sigma_{exp})_{min}$ which are the maximum and the minimum of the ratios of the theoretical cross-section σ_{th} to the experimental cross-section σ_{exp} over the whole energy range of the σ_{12} experimental data. For the Ne target these are about unity at the highest energies and about 0.6 at the lowest energies, respectively, so that the experimental data are slightly less than the σ_{th} values at the lowest energies. The ratios $(\sigma_{th}/\sigma_{exp})_{max}$ and $(\sigma_{th}/\sigma_{exp})_{min}$ for the Ar target are about 1.2 at the lowest energies and about 1.1 at the highest energies, respectively, and those for the Kr target are about 2 at the lowest energies and for about unity at the highest energies, respectively, so that the experimental data for the two targets, except the data for the Kr target at the lowest energies, are smaller than the theoretical values over the ion energy range. The theoretical cross-section formula fits well with both the absolute magnitudes and

<u>Fig.5-7</u>

Comparison of the experimental cross-sections σ_{12} for N_1^+ ions in Ne, Ar, and Kr with the σ_{12} theoretical solid curves from Eq.(2-40) of the two-state theory[9,10]. The average ionization potential used for all the collisions is 14.8 eV. The energy defects Q used are listed in Table 5-3.

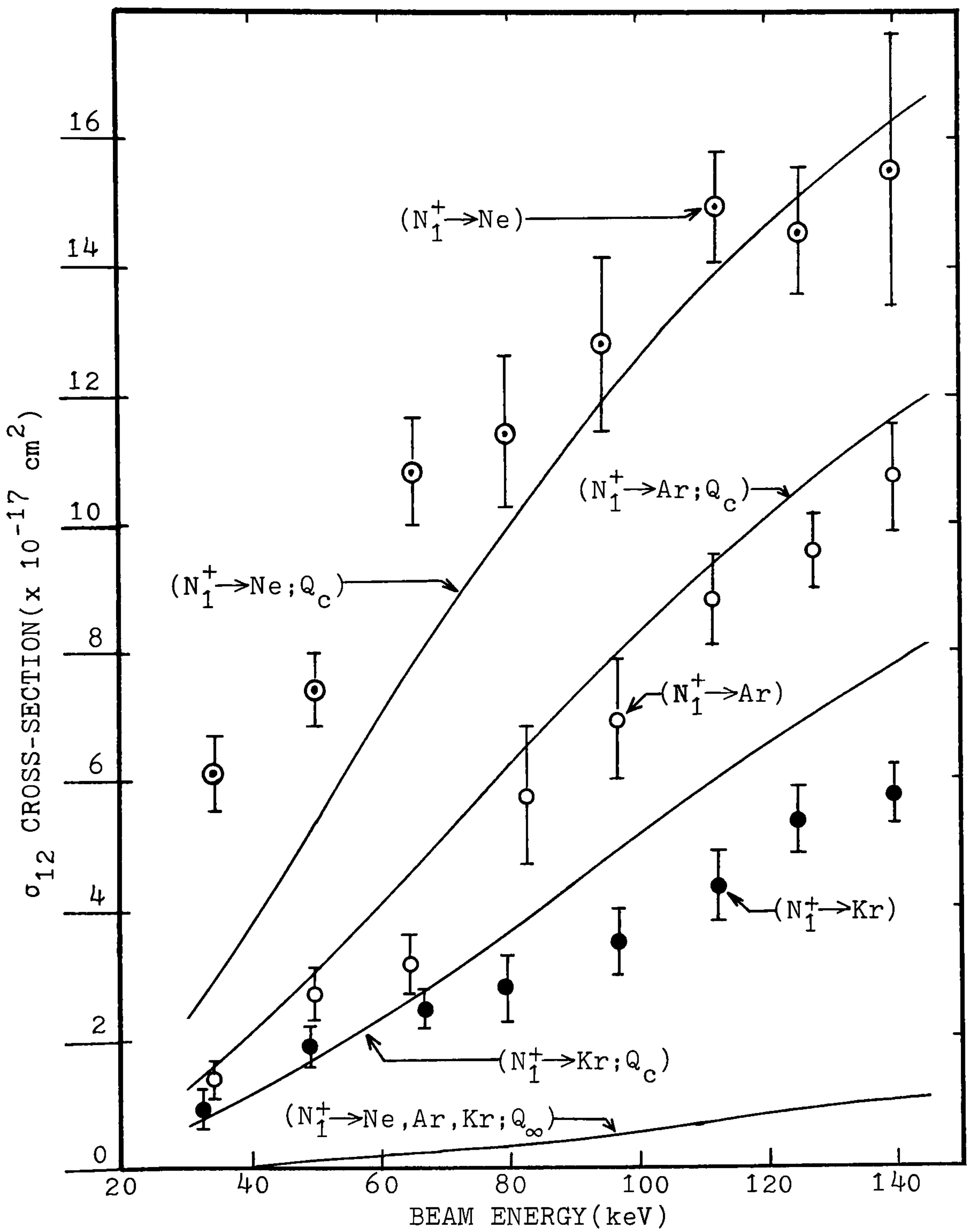

the energy variations of the σ_{12} cross-sections, considering the crudity and the many approximations used in its derivation.

The theoretical asymmetric charge exchange cross-sections σ_{21} for the present electron capture collisions, computed using the same formulation are shown in fig. 5-8, where we used the statistical weighting factor s = 1 for all the collisions because the possible initial molecular $^3\Sigma^-$ and $^3\pi$ states are available among the states of the $(^2P + ^2P)$ final system. The function $\Phi(u_1)$ was not rapidly dependent on the ionization potential so that the choice of I was not critical whether one uses the $I(Ar^+)$, $I(B)$, or the average ionization potential $\frac{1}{2}[I(Ar^+)+I(B)]$. When used with the Q_∞ values, the absolute magnitudes of the cross-sections σ_{21} for the Ne target are predicted small by a factor of about two, and the general trend in the theoretical energy dependence of the cross-sections is unable to account for the cross-section maximum at about 95 keV. For the Ar and Kr targets, the theory predicts fairly well the general trends but predicts much smaller cross-section magnitudes by a factor of between 10 and a few hundred than the experimental data. When used with the corrected energy defects Q_c, the predictions of the theory are much improved since the average ratio of the theoretical and experimental results over the present ion energy range is about 0.4 for the Ne target, about 0.2 for the Ar target, and about 0.1 for the Kr target. As an empirical observation, it was found that the absolute cross-section magnitudes and their energy variations agree well with the experimental data when the theoretical cross-sections $\sigma_{21}(b_1, v, I, Q_c)$ were multiplied

Fig.5-8

Comparison of the experimental cross-sections σ_{21} for Ar^{++} ions in Ne, Ar, and Kr with the σ_{21} theoretical solid curves from Eq.(2-40) of the two-state theory[9,10]. The average ionization potential used is 24.6 eV for the Ne target, 21.7 eV for the Ar target, and 20.8 eV for the Kr target. The energy defects Q used are listed in Table 5-3.

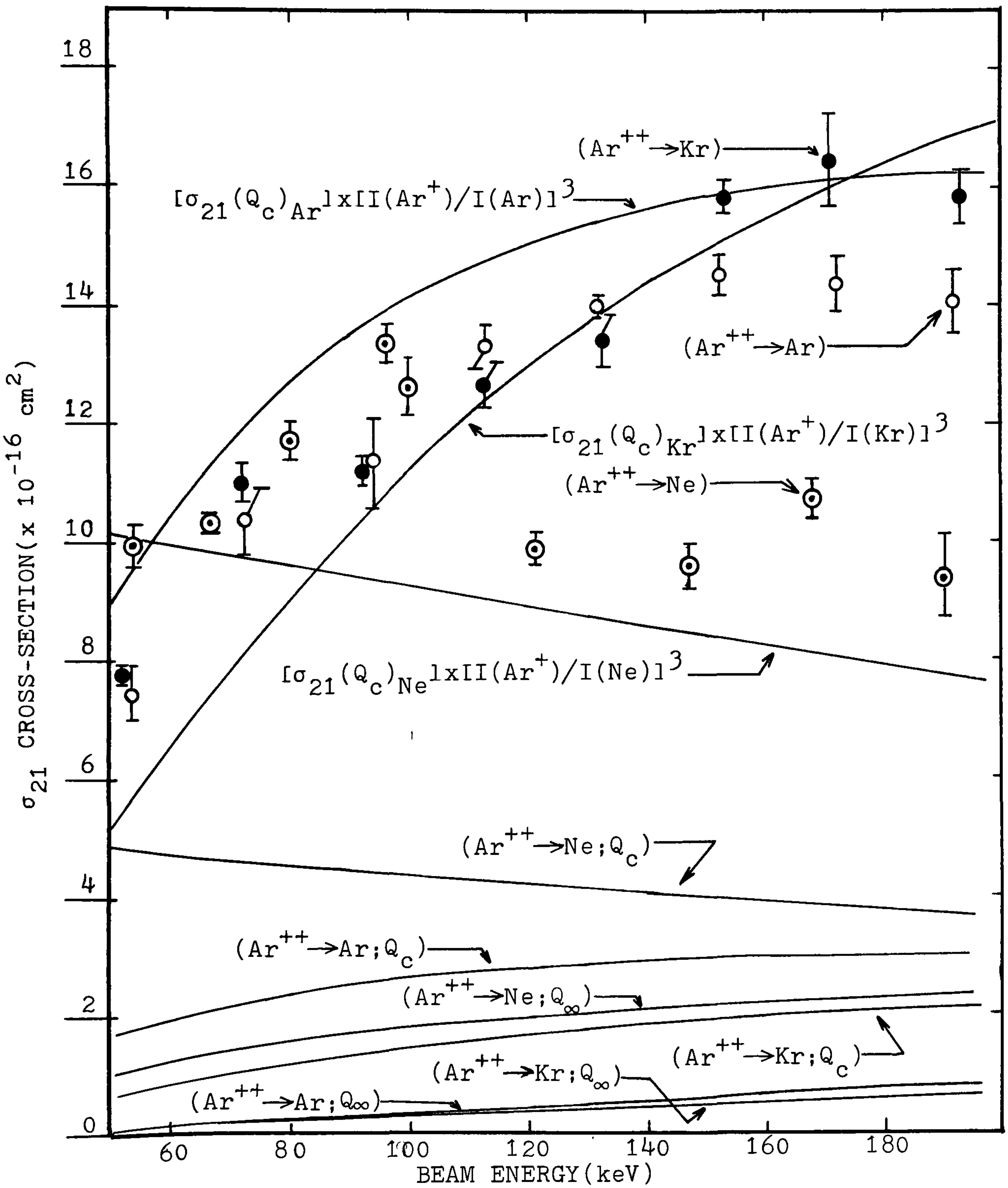

by an arbitrary correction factor $[I(Ar^+)/I(B)]^3$ where B = Ne, Ar, or Kr, as shown in fig. 5-8.

In summary, it appears that this rather coarse theory[9] is able to predict quite well the single electron loss cross-sections σ_{12}, but not so well the electron capture cross-sections σ_{21}. The differences between theory and experiment are to be expected in view of the crudity of the theory and the many approximations which it assumes.

Since no recoil particles were observed in the σ_{12} measurements with the inert target atoms, the charge-changing processes can not be distinguished from the charge transfer and stripping processes. In an electron stripping model, Firsov's statistical cross-section formula[13] in eq. (2-48) of Chapter II gives the general trend in the energy dependence of the cross-sections shown in fig. 5-9 in which the ratio σ_{th}/σ_{exp} over the present ion energy range is about 3 for the Ne target, about 9 for the Ar target, and up to about 20 for the Kr target. It therefore predicts an inverted relative ordering of the cross-sections between the three targets compared with the experimental data, whereas the above two-state theory agrees with the experimental ordering.

Fig. 5-9

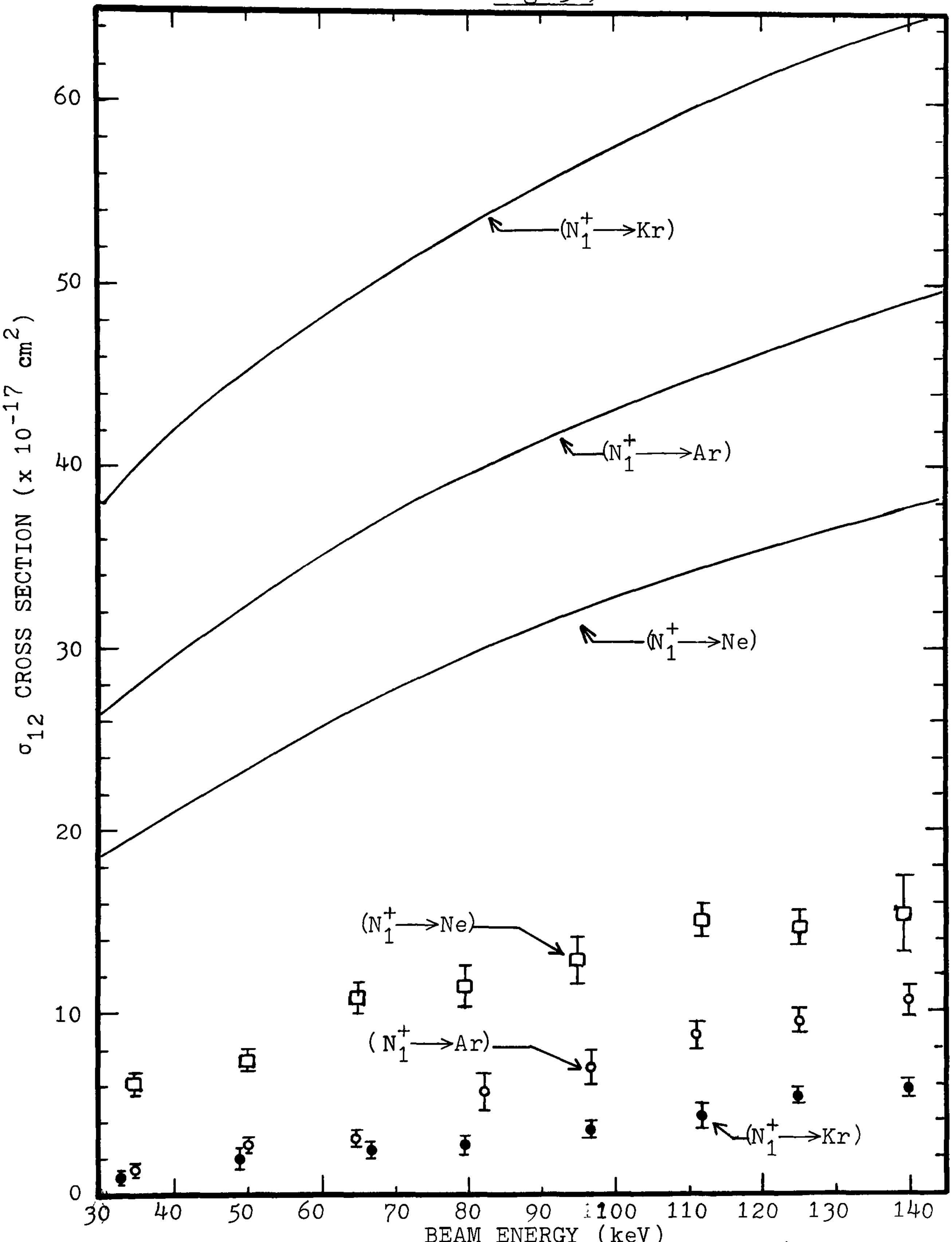

Comparison of the experimental σ_{12} cross sections for N_1^+ ions in Ne, Ar, and Kr(having I=29.61 eV) with the σ_{12} theoretical solid curves from Eq.(2-48) of the Firsov's statistical theory[13].

CHAPTER VI SUMMARY AND CONCLUSION

The absolute total cross-sections for both the single electron loss of N_1^+(30 keV - 150 keV) ions and the single electron capture of Ar^{++}(50 keV - 190 keV) on the gas targets Ne, Ar, and Kr were measured, and emphasis was placed on minimizing the systematic errors which may be present in many of the early data.

In the present σ_{12} experimental results, all the cross-sections for the three targets rise gradually with increasing energy of the N_1^+ ion. In general, the σ_{12} cross-sections are the order of about 10^{-17} cm^2 at the lowest energy of about 34 keV and the order of about 10^{-16} cm^2 at the highest energy of 140 keV. The present σ_{21} cross-section data for the Ar^{++} ions pass through a maximum at about 95 keV for the Ne target, about 150 keV for the Ar target, and about 170 keV for the Kr target. All the σ_{21} cross-sections over the ion energy range are in the range between 7×10^{-16} cm^2 and 1.7×10^{-15} cm^2. In general, the errors of the experimental data are estimated at about ±15% for the electron loss cross-sections and within ±4% for the electron capture cross-sections.

The corrections for both the angular-energy spreads and the target thickness were found to be significant, particularly for the σ_{12} electron loss cross-section measurements[1]. In addition, an important precaution in the instrumental tests[2] was the the detection efficiency of a channeltron as a particle detector was uniform across the windowless entrance aperture, even though the gain of the detector was shown experimentally to vary with the ion impact position across the aperture. No obvious relation between the counting rate ratio in the cross-section measurements and the operating conditions of the ion source was found, so that any long-lived excited ions in the incident beams were probably small enough to be neglected, or may be unimportant in the charge-changing cross-section measurements. The contamination of N_2^{++} ions in the N_1^{+} beam, which had not been checked in the previous published charge-changing cross-section measurements, was found to be small enough to be neglected in the present cross-section measurements.

In comparison with the previous experimental data, the lack of agreement among the previous measurements seems to be explainable in terms of the angular-energy spreads of the ions and the target thickness. The conventional method using the thin target approximation could be concluded to be inadequate, particularly for the electron loss cross-section measurements, and the power series solution of the differential equation using a four-charge component system in the beam from the target chamber was found to be necessary to determine the cross-sections.

A comparison of the present experimental data with the two-state theory[9-12] in a form which has many approximations shows the following.

(1) It is preferable to use effective(corrected) energy defects[12] in both the adiabatic maximum rule[12] and the cross-section theory[9], so that the energy of the cross-section maxima and the relative energy ordering between the different targets could be predicted reasonably by them.

(2) The rather doubtful function approximation which was made by Rapp and

Francis improves the fit of the two-state theory[9] to the present experimental data, so that the relatively more accurate form of eq. (2-42) of Chapter II is a worse fit to the present experimental data.

(3) The Lee and Hasted choice[10] for the b_1 parameter, the upper limit on the impact parameter integration seems to be better on the whole than that of Rapp and Francis[9] or Dalgano[16].

(4) Particularly for the electron loss collisions, the two-state cross-section theory[9] predicts very well the fit for both the absolute cross-section magnitudes and their energy variations, considering its crudity and the many approximation in its derivation.

(5) The theory predicts also the reasonable energy variations of the present electron capture cross-sections σ_{21}, but is unable to account for the relative cross-section ordering between the three targets. Here, it was found empirically that the theoretical cross-sections $\sigma_a(b_1, v. I, Q_c)$ agree well with the experimental data when an arbitrary correction factor $[I(Ar^{++})/I(B)]^3$ was multipled by the two-state cross-sections, where $I(Ar^+)$ is the ionization potential of the scattered ion Ar^+ and $I(B)$ is the ionization potential of the target atom B (= Ne, Ar, or Kr).

The statistical Firsov electron stripping cross-section formula predicts well the energy variations of the cross-sections q_{12}, but predicts an inverted relative cross-section ordering between the three targets and the absolute magnitudes of the cross-sections are quite wrong, perhaps because it is a neutral-neutral atom collision theory.

In total, both the rather coarse theories are able to predict the general trend of energy(velocity) dependence of the cross-sections.

The differences between theory and experiment are to be expected in view of the crudity of the theory and the many approximations which it assumes.

APPENDIX I

In the two-state theory[9,10], asymmetric charge exchange cross-sections for atomic collisions are calculated from

$$\sigma_a = S \ \tfrac{1}{2}\pi b_o^2 \ \Phi(u_1) \ a_o^2$$

where the statistical weighting factor S is the fraction of the initial molecular states which have the correct quantum numbers to form allowed final molecular states after the charge transfer, $b_o = b_1/a_o$ is the impact parameter in atomic units, and a_o is the Bohr radius. The values of b_o and of u_1 can be obtained from the collision velocity v(in cm/sec) using Table AI-1 for the known values of I, the ionization potential (in eV) and Q, the energy defect (in eV). The value of u_1 can then be used to obtain $\Phi(u_1)$ using Table AI-2.

Table AI-1 was made using eqs. (2-35) and (2-39) and the Lee and Hasted condition $P_s(b_1, v) = \sin^2(\pi/6)$ for the choice of b_1, those equations can be inverted to give respectively,

$$v = \left(\frac{2\pi}{\gamma}\right)^{\frac{1}{2}} \frac{6Ia_o b_o^{3/2}}{\pi\hbar} \left(1 + \frac{1}{\gamma b_o}\right) \exp(-\gamma b_o) \qquad \text{(A-1)}$$

$$u_1 I^{\frac{1}{2}}/|Q| = \frac{\pi}{12} (Ib_o^2)^{-\frac{1}{2}} \left(1 + \frac{1}{\gamma b_o}\right)^{-1} \exp(\gamma b_o) \qquad \text{(A-2)}$$

It is not easy to obtain an analytic solution for b_o from eq. (A-1), but the value of b_o can be obtained by interpolation from the Table.

Table AI -1

Ib_o^2 (eV)	$u_1 I^{\frac{1}{2}}/\lvert Q\rvert$	v (x 10^7 cm/sec)
0	0.07908	0.00000
20	0.10784	37.85481
40	0.14523	33.42854
60	0.18696	28.73643
80	0.23419	24.65254
100	0.28774	21.21511
120	0.34842	18.33738
140	0.41703	15.92261
160	0.49440	13.88682
180	0.58141	12.16135
200	0.67903	10.69105
220	0.78825	9.43177
240	0.91016	8.34802
260	1.04594	7.41116
280	1.19683	6.59793
300	1.36417	5.88928
320	1.54939	5.26958
340	1.75403	4.72584
360	1.97976	4.24729
380	2.22832	3.82488
400	2.50160	3.45102
420	2.80161	3.11928
440	3.13050	2.82422
460	3.49058	2.56119
480	3.88429	2.32620
500	4.31425	2.11585
520	4.78325	1.92720
540	5.29426	1.75769
560	5.85042	1.60512
580	6.45513	1.46758
600	7.11194	1.34338
620	7.82467	1.23106
640	8.59737	1.12935
660	9.43431	1.03711
680	10.34010	0.95335
700	11.31954	0.87719
720	12.37781	0.80786
740	13.52031	0.74468
760	14.75288	0.68703
780	16.08160	0.63427
800	17.51298	0.58622
820	19.05387	0.54215
840	20.71157	0.50177
860	22.49378	0.46474
880	24.40864	0.43075
900	26.46475	0.39952
920	28.67120	0.37081
940	31.03762	0.34438
960	33.57418	0.32005
980	36.29165	0.29761
1000	39.20130	0.27692

Ib_o^2 (eV)	$u_1 I^{\frac{1}{2}}/\lvert Q\rvert$	v (x 10^7 cm/sec)
10	0.09006	38.11560
30	0.12609	35.83003
50	0.16547	31.02262
70	0.20983	26.61036
90	0.26012	22.85768
110	0.31714	19.71250
130	0.38168	17.07772
150	0.45456	14.86199
170	0.53664	12.98903
190	0.62883	11.39730
210	0.73212	10.03743
230	0.84755	8.86989
250	0.97624	7.86279
270	1.11941	6.99037
290	1.27835	6.23158
310	1.45445	5.56919
330	1.64919	4.98893
350	1.86416	4.47902
370	2.10107	4.02957
390	2.36174	3.63230
410	2.64813	3.28024
430	2.96230	2.96748
450	3.30649	2.68896
470	3.68307	2.44041
490	4.09457	2.21814
510	4.54369	2.01898
530	5.03331	1.84020
550	5.56649	1.67942
570	6.14649	1.53458
590	6.77678	1.40391
610	7.46107	1.28582
630	8.20327	1.17895
650	9.00753	1.08211
670	9.87831	0.99423
690	10.82029	0.91437
710	11.83849	0.84172
730	12.93818	0.77554
750	14.12497	0.71520
770	15.40482	0.66011
790	16.78404	0.60976
810	18.26928	0.56370
830	19.86766	0.52152
850	21.58663	0.48286
870	23.43411	0.44784
890	25.41847	0.41481
910	27.54856	0.38487
930	29.83380	0.35732
950	32.28399	0.33197
970	34.90962	0.30860
990	37.72171	0.28706
1010	40.73190	0.26717

Table AI -1 continued

Ib_o^2 (eV)	$u_1 I^{\frac{1}{2}}/\lvert Q \rvert$	v (x 10^5 cm/sec)	Ib_o^2 (eV)	$u_1 I^{\frac{1}{2}}/\lvert Q \rvert$	v (x 10^5 cm/sec)
1020	42.31513	25.78121	1030	43.95256	24.88136
1040	45.64578	24.01635	1050	47.39656	23.18459
1060	49.20649	22.38478	1070	51.07752	21.61549
1080	53.01142	20.87543	1090	55.01002	20.16339
1100	57.07527	19.47821	1110	59.20916	18.81875
1120	61.41371	18.18394	1130	63.69097	17.57279
1140	63.69097	17.57279	1150	66.04312	16.98430
1160	68.47236	16.41755	1170	70.98081	15.87167
1180	73.57102	15.34577	1190	76.24519	14.83908
1200	79.00575	14.35083	1210	81.85528	13.88027
1220	84.79624	13.42667	1230	87.83129	12.98941
1240	90.96321	12.56781	1250	94.19464	12.16125
1260	97.52845	11.76915	1270	100.9676	11.39093
1280	104.5150	11.02609	1290	108.1737	10.67405
1300	111.9469	10.33437	1310	115.8378	10.00654
1320	119.8496	9.69014	1330	123.9857	9.38470
1340	128.2499	9.08982	1350	132.6452	8.80509
1360	137.1755	8.53013	1370	141.8446	8.26458
1380	146.6562	8.00809	1390	151.6143	7.76030
1400	156.7227	7.52092	1410	161.9859	7.28960
1420	167.4079	7.06607	1430	172.9929	6.85003
1440	178.7455	6.64122	1450	190.7715	6.24422
1460	197.0545	6.05552	1470	203.5236	5.87305
1480	210.1842	5.69658	1490	217.0411	5.52591
1500	224.0999	5.36081	1510	231.3656	5.20109
1550	262.6113	4.61231	1600	307.0270	3.97651
1650	358.1591	3.43514	1700	416.9191	2.97310
1750	484.3325	2.57789	1800	561.5471	2.23914
1850	649.8493	1.94818	1900	750.6801	1.69778
1950	865.6479	1.48189	2000	996.5517	1.29548
2050	1145.398	1.13405	2100	1278.888	1.02060
2150	1465.835	0.89571	2200	1677.644	0.78716
2250	1968.904	0.67526	2300	2246.506	0.59508
2350	2259.857	0.52505	2400	2913.167	0.46381
2450	3311.113	0.41017	2500	3758.866	0.36314
2550	4262.156	0.32185	2600	4287.355	0.28555
2650	5461.324	0.25361	2700	6171.929	0.22546
2750	6967.667	0.20063	2800	7857.921	0.17870
2850	8853.082	0.15932	2900	9964.554	0.14216
2950	11204.91	0.12697	3000	12587.83	0.11349
3050	14128.98	0.10153	3100	15844.61	0.09091
3150	17753.24	0.08146	3200	19874.98	0.07305
3250	22231.97	0.06556	3300	24848.41	0.05888
3350	27750.84	0.05292	3400	30968.38	0.04760
3450	34532.87	0.04284	3500	38478.51	0.03859
3550	42844.97	0.03478	3600	47672.73	0.03137
3650	53007.07	0.02831	3700	58898.40	0.02556
3750	65401.05	0.02310	3800	72573.25	0.02088
3850	80480.62	0.01889	3900	89193.81	0.01710
3950	98787.06	0.01549	4000	109348.2	0.01404

Table AI-2

Values of the integral $\bar{\Phi}(u_1)=(4/u_1^4)\int_0^{u_1} u^3(\mathrm{sech}^2 u)\,du$ for values of u_1 from 0.0 to 10.0.

u_1 ↓ \ u_1 →	0.00000	0.01000	0.02000	0.03000	0.04000	0.05000	0.06000	0.07000	0.08000	0.09000
0.0	1.00000	0.99993	0.99973	0.99940	0.99893	0.99834	0.99760	0.99674	0.99575	0.99462
0.1	0.99337	0.99198	0.99047	0.98883	0.98760	0.98517	0.98315	0.98101	0.97874	0.97636
0.2	0.97386	0.97124	0.96850	0.96564	0.96268	0.95960	0.95641	0.95311	0.94791	0.94620
0.3	0.94259	0.93888	0.93507	0.93117	0.92717	0.92307	0.91889	0.91461	0.91026	0.90581
0.4	0.90129	0.89668	0.89200	0.88726	0.88242	0.87752	0.87255	0.86751	0.86241	0.85726
0.5	0.85204	0.84676	0.84143	0.83605	0.83062	0.82514	0.81961	0.81405	0.80844	0.80279
0.6	0.79711	0.79139	0.78564	0.77985	0.77405	0.76821	0.76235	0.75647	0.75057	0.74465
0.7	0.73872	0.73277	0.72681	0.72084	0.71486	0.70887	0.70288	0.69689	0.69089	0.68490
0.8	0.67890	0.67291	0.66693	0.66095	0.65498	0.64901	0.64306	0.63712	0.63120	0.62538
0.9	0.61939	0.61351	0.60765	0.60181	0.59599	0.59019	0.58441	0.57866	0.57293	0.56723
1.0	0.56155	0.55590	0.55028	0.54469	0.53913	0.53359	0.52809	0.52262	0.51719	0.51178
1.1	0.50641	0.50108	0.49577	0.49051	0.48528	0.48008	0.47493	0.46981	0.46472	0.45968
1.2	0.45467	0.44970	0.44477	0.43988	0.43503	0.43021	0.42544	0.42071	0.41601	0.41136
1.3	0.40674	0.40217	0.39763	0.39314	0.38869	0.38428	0.37990	0.37557	0.37128	0.36703
1.4	0.36282	0.35865	0.35452	0.35043	0.34638	0.34237	0.33840	0.33447	0.33085	0.32673
1.5	0.32291	0.31914	0.31541	0.31171	0.30806	0.30444	0.30086	0.29732	0.29382	0.29035
1.6	0.28692	0.28353	0.28018	0.27686	0.27358	0.27033	0.26712	0.26395	0.26081	0.25771
1.7	0.25464	0.25161	0.24861	0.24565	0.24272	0.23982	0.23695	0.23412	0.23133	0.22856
1.8	0.22583	0.22313	0.22046	0.21782	0.21521	0.21264	0.21009	0.20757	0.20509	0.20261
1.9	0.20020	0.19781	0.19544	0.19310	0.19078	0.18850	0.18624	0.18401	0.18181	0.17963
2.0	0.17748	0.17536	0.17326	0.17119	0.16914	0.16712	0.16512	0.16315	0.16120	0.15928
2.1	0.15738	0.15550	0.15365	0.15182	0.15001	0.14822	0.14646	0.14472	0.14300	0.14130
2.2	0.13962	0.13796	0.13633	0.13471	0.13312	0.13154	0.12998	0.12845	0.12693	0.12543
2.3	0.12395	0.12249	0.12105	0.11962	0.11822	0.11683	0.11546	0.11410	0.11276	0.11144
2.4	0.11014	0.10885	0.10758	0.10632	0.10508	0.10386	0.10265	0.10146	0.10028	0.09912
2.5	0.09797	0.09683	0.09571	0.09460	0.09351	0.09243	0.09137	0.09032	0.08928	0.08825
2.6	0.08724	0.08624	0.08525	0.08428	0.08331	0.08236	0.08142	0.08050	0.07958	0.07868
2.7	0.07778	0.07690	0.07603	0.07517	0.07432	0.07349	0.07266	0.07184	0.07103	0.07024
2.8	0.06945	0.06867	0.06790	0.06714	0.06640	0.06566	0.06493	0.06420	0.06349	0.06279
2.9	0.06209	0.06141	0.06073	0.06006	0.05940	0.05875	0.05810	0.05747	0.05684	0.05622
3.0	0.05560	0.05500	0.05440	0.05381	0.05322	0.05265	0.05208	0.05151	0.05096	0.05041
3.1	0.04987	0.04933	0.04880	0.04828	0.04776	0.04725	0.04675	0.04625	0.04576	0.04527
3.2	0.04479	0.04432	0.04385	0.04339	0.04293	0.04248	0.04203	0.04159	0.04115	0.04072
3.3	0.04030	0.03988	0.03946	0.03905	0.03865	0.03825	0.03785	0.03746	0.03707	0.03669
3.4	0.03632	0.03594	0.03557	0.03521	0.03485	0.03450	0.03414	0.03380	0.03345	0.03311
3.5	0.03278	0.03245	0.03212	0.03180	0.03148	0.03116	0.03085	0.03054	0.03024	0.02994
3.6	0.02964	0.02934	0.02905	0.02876	0.02848	0.02820	0.02792	0.02765	0.02738	0.02711
3.7	0.02684	0.02658	0.02632	0.02606	0.02581	0.02556	0.02531	0.02507	0.02483	0.02459
3.8	0.02435	0.02412	0.02388	0.02366	0.02343	0.02321	0.02298	0.02277	0.02255	0.02234
3.9	0.02213	0.02192	0.02171	0.02151	0.02130	0.02110	0.02091	0.02071	0.02052	0.02033
4.0	0.02014	0.01995	0.01977	0.01958	0.01940	0.01922	0.01905	0.01887	0.01870	0.01853

Table AI-2 continued

u_1 → / v ↓	0.00000	0.01000	0.02000	0.03000	0.04000	0.05000	0.06000	0.07000	0.08000	0.09000
4.1	0.01836	0.01819	0.01802	0.01786	0.01770	0.01754	0.01738	0.01722	0.01707	0.01691
4.2	0.01676	0.01661	0.01646	0.01632	0.01617	0.01603	0.01588	0.01574	0.01560	0.01547
4.3	0.01533	0.01519	0.01506	0.01493	0.01480	0.01467	0.01454	0.01441	0.01429	0.01416
4.4	0.01404	0.01392	0.01380	0.01368	0.01356	0.01345	0.01333	0.01322	0.01310	0.01299
4.5	0.01283	0.01277	0.01266	0.01256	0.01245	0.01234	0.01224	0.01214	0.01204	0.01193
4.6	0.01183	0.01174	0.01164	0.01154	0.01144	0.01135	0.01126	0.01116	0.01107	0.01098
4.7	0.01089	0.01080	0.01071	0.01062	0.01054	0.01045	0.01037	0.01028	0.01020	0.01012
4.8	0.01003	0.00995	0.00987	0.00979	0.00971	0.00964	0.00956	0.00948	0.00941	0.00933
4.9	0.00926	0.00919	0.00911	0.00904	0.00897	0.00890	0.00883	0.00876	0.00869	0.00862
5.0	0.00856	0.00849	0.00842	0.00836	0.00829	0.00823	0.00816	0.00810	0.00804	0.00798
5.1	0.00792	0.00786	0.00780	0.00774	0.00768	0.00762	0.00756	0.00750	0.00745	0.00739
5.2	0.00734	0.00728	0.00723	0.00717	0.00712	0.00706	0.00701	0.00696	0.00691	0.00686
5.3	0.00680	0.00675	0.00670	0.00666	0.00661	0.00656	0.00651	0.00646	0.00641	0.00637
5.4	0.00632	0.00628	0.00623	0.00618	0.00614	0.00610	0.00605	0.00601	0.00596	0.00592
5.5	0.00588	0.00584	0.00580	0.00575	0.00571	0.00567	0.00563	0.00559	0.00555	0.00551
5.6	0.00547	0.00544	0.00540	0.00536	0.00532	0.00529	0.00525	0.00521	0.00518	0.00514
5.7	0.00510	0.00507	0.00503	0.00500	0.00496	0.00493	0.00490	0.00486	0.00483	0.00480
5.8	0.00476	0.00473	0.00470	0.00467	0.00464	0.00460	0.00457	0.00454	0.00451	0.00448
5.9	0.00445	0.00442	0.00439	0.00439	0.00433	0.00430	0.00428	0.00425	0.00422	0.00419
6.0	0.00416	0.00414	0.00411	0.00408	0.00405	0.00403	0.00400	0.00398	0.00395	0.00392
6.1	0.00390	0.00387	0.00385	0.00382	0.00380	0.00377	0.00375	0.00373	0.00370	0.00368
6.2	0.00365	0.00363	0.00361	0.00358	0.00356	0.00354	0.00352	0.00349	0.00347	0.00345
6.3	0.00343	0.00341	0.00339	0.00336	0.00334	0.00332	0.00330	0.00328	0.00326	0.00324
6.4	0.00322	0.00320	0.00318	0.00316	0.00314	0.00312	0.00310	0.00308	0.00306	0.00305
6.5	0.00303	0.00301	0.00299	0.00297	0.00295	0.00294	0.00292	0.00290	0.00288	0.00287
6.6	0.00285	0.00283	0.00281	0.00280	0.00278	0.00276	0.00275	0.00273	0.00271	0.00270
6.7	0.00268	0.00267	0.00265	0.00263	0.00262	0.00260	0.00259	0.00257	0.00256	0.00254
6.8	0.00253	0.00251	0.00250	0.00248	0.00247	0.00246	0.00244	0.00243	0.00241	0.00240
6.9	0.00238	0.00237	0.00236	0.00234	0.00233	0.00232	0.00230	0.00229	0.00228	0.00226
7.0	0.00225	0.00224	0.00223	0.00221	0.00220	0.00219	0.00218	0.00216	0.00215	0.00214
7.1	0.00213	0.00212	0.00210	0.00209	0.00208	0.00207	0.00206	0.00205	0.00203	0.00202
7.2	0.00201	0.00200	0.00199	0.00198	0.00197	0.00196	0.00195	0.00194	0.00193	0.00191
7.3	0.00190	0.00189	0.00188	0.00187	0.00186	0.00185	0.00184	0.00183	0.00182	0.00181
7.4	0.00180	0.00179	0.00178	0.00177	0.00176	0.00176	0.00175	0.00174	0.00173	0.00172
7.5	0.00172	0.00170	0.00169	0.00168	0.00167	0.00166	0.00166	0.00165	0.00164	0.00163
7.6	0.00162	0.00161	0.00160	0.00160	0.00159	0.00158	0.00157	0.00156	0.00155	0.00155
7.7	0.00154	0.00153	0.00152	0.00151	0.00151	0.00150	0.00149	0.00148	0.00148	0.00147
7.8	0.00146	0.00145	0.00145	0.00144	0.00143	0.00142	0.00142	0.00141	0.00140	0.00140
7.9	0.00139	0.00138	0.00137	0.00137	0.00136	0.00136	0.00135	0.00134	0.00133	0.00133
8.0	0.00132	0.00131	0.00131	0.00130	0.00129	0.00129	0.00128	0.00128	0.00127	0.00126
9.0	0.00082	0.00082	0.00082	0.00081	0.00081	0.00081	0.00080	0.00080	0.00080	0.00079
10.0	0.00056	0.00056	0.00056	0.00056	0.00055	0.00055	0.00055	0.00055	0.00055	0.00054

APPENDIX II AN EXPERIMENTAL INVESTIGATION OF CHANNELTRON GAIN VARIATIONS WITH THE POSITION OF THE ENERGETIC HEAVY ION IMPACTS ON THE ENTRANCE APERTURE.[2]

In the Amperex Type B312BL channeltron used to detect the ions in the present cross-section measurements, it was found that the channeltron gain is significantly changed depending on the positions at which an energetic heavy ion beam of 100 keV N_1^+ enters the channel electron multiplier. This particular multiplier has a windowless rectangular 10 mm x 3 mm cone and a closed end-output as mentioned in section III-3 of Chapter III. In contrast to this gain variation, the detection efficiency showed no significant variation with the point of the ion impact. This efficiency observation suggests that at least one of the electrons from the primary interaction of the ion with the secondary surface is multiplied by the channel to provide a detectable signal.

In the circuit which is described in section III-3 of Chapter III, pulses from a mercury pulse reference generator (CI, Model 1407) were fed through a small 1.5 pf capacitor in the emitter-follower-pre-amplifier to the multichannel analyzer, so that, for this particular investigation, a calibration of the current pulse amplitudes as a function of the channel number of the multichannel analyzer gives an estimate of the current gain of the channeltron as a function of the channel number of the multichannel analyzer.

By using the multichannel analyzer for investigating the current pulses, the pulse height distributions were observed for carefully chosen

Fig.A -1

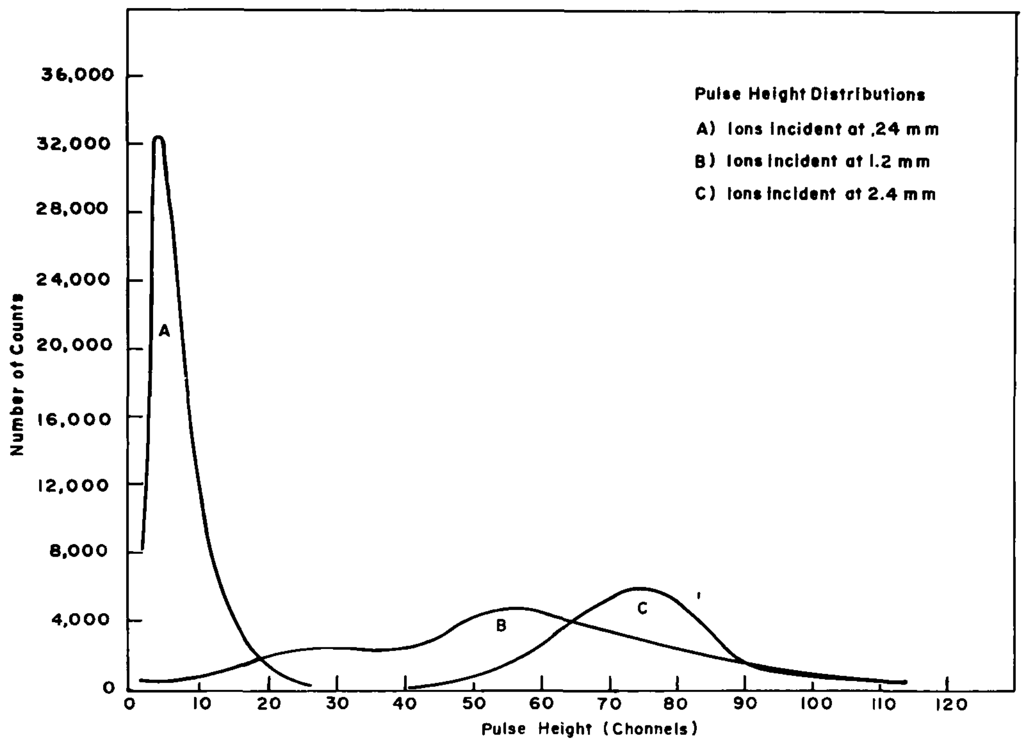

The pulse height distributions from the channel electron multiplier when the 100 keV N_1^+ ions had different regions of impact on the entrance aperture;A) represents a point of impact down the inside of the channel, B) represents an intermediate point of impact where some of the ions traveled down the channel and others struck the apex of entrance c cone, and C) represents a points a point of impact near the edge of the entrance cone.

positions of the ion impact across the entrance aperture of the channeltron. Some typical pulse height distributions are shown in fig. A-1. Examination of the pulse shapes on an oscilloscope showed that there was no detectable variation with the position, so that there was no indication of ion feedback effects within the channel of the multiplier. As shown in fig. A-2, the most probable pulse height which corresponds to the peak of each of the pulse height distributions was plotted as a function of the ion impact position. The outstanding feature of this figure is the sudden drop in pulse height in the central region, which corresponds very well in position and width to the internal diameter of the channel. The pulse heights from ions which strike the cone are evidently much larger than those from ions which go directly into channel.

As shown in fig. A-2, for a given voltage of 3.0 keV on the channeltron, the pulse heights measured with a positive bias voltage of 70V on the image slit of the electrostatic analyzer were generally smaller than those measured with no bias voltage. This seems to have resulted in about 15% increase in the pulse height for pulses from the cone region, decreasing somewhat towards the central region. The biggest pulse height difference variation occurs near the image slit. This may be explained by a loss of secondary electrons emitted from the cone edge to the image slit, when the positive bias voltage of 70V was applied to the slit. In the angle profiles, such bias voltages did not influence the counting rates in the flat-topped region whose length always corresponded closely to the horizontal length of the image slit,

Fig.A-2

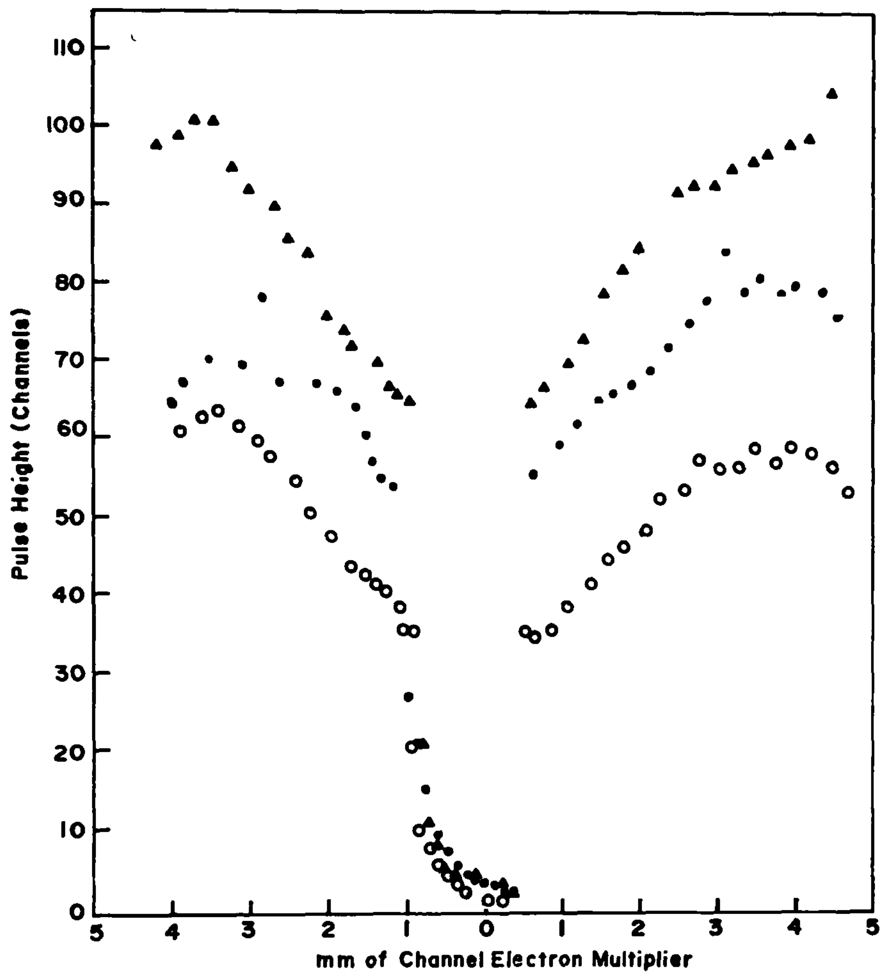

The most probable pulse height, corresponding to the peak of the pulse height distribution, as a function of the position along the entrance aperture at which the ions struck the channel electron multiplier. The solid circles represent measurements with a positive 70 V bias on the image slit and a 3 kV multiplier voltage. The triangles show the effect of removing the image slit bias, whereas the open circles show the effect of reducing the multiplier voltage to 2.7 kV. The vertical scale, which corresponds to the horizontal scale of Fig.4-1, is such that one channel represents a current gain of about 4.9×10^5.

where there was no focus in the horizontal (axial) field component of the electrostatic analyzer as described in the section III-2 of Chapter III. For a given positive bias voltage of 70V applied to the image slit, the saturation effects in the channeltron were tested by reducing the channeltron working voltage from 3.0 kV to 2.7 kV. In this case, the pulse heights were reduced uniformly by about 20% in the central region and by about 35% in the cone region. These changes were much smaller than those would be expected if there was no saturation. The general shapes of those pulse height profiles shown in fig. A-2 did not change between the two working voltages of the channeltron.

The interpretation of the above results is now discussed. Since the positive ions had much more momentum than the secondary electrons emitted from the cone and channel of the channeltron, the deep minimum region in the pulse height profiles shown in fig. A-2 may be explained by those ions which are not much deflected by the electric fields within the channel and cone, so those ions can travel directly into the end of straight part of the channel before striking the inside wall surface of the channel. There is less current gain because of the shorter length of the remaining part of the channel helix in which the secondary electrons can be multiplied. The width of the small pulse height profiles at the central region is in very good agreement with the inside diameter of the channel, which is specified as between 1.1 mm and 1.4 mm. On each side of the central region of the pulse height profiles shown in fig. 4-2, there are regions where both large and small pulse heights appeared simultaneously in the pulse height distributions. This is probably caused by the incident ion beam spread, so that some ions of the beam travel directly into the channel and the remainder strikes the cone surface near the boundary between the cone and the channel. The slope in the central region of the small pulse heights may be explained by the geometrical direction of the curvature at the end of the straight part of the channel. When the ion beam travels parallel and close to the inside wall of the straight part of the channel, the ions will strike further along the gradually curved part of the channel, and those pulse heights will be smaller.

In fig. A-2 in which one channel represents approximately 4.9×10^5 current gain when a single electronic charge starts the multiplication process, the pulse height profile made with 3.0 kV and 70V respectively of the channeltron working and slit bias voltages shows that the current gain for the ions which struck the cone is estimated to be 3.42×10^7 (at 70 channels of the multichannel analyzer). The total effective length of secondary electron emission surface is about 65 mm including about half the cone length. Assuming that there is no saturation in the channeltron and the multiplication is uniform along the length, the number n of the electronic charges is given by $dn/dx = kx$ for the pulse current at a point along the effective length x. The solution yields $n = \exp(kx)$ with the boundary condition $n = 1$, at $x = 0$, where k is a constant. Substituting $n = 3.42 \times 10^7$ at $x = 65$ mm into that solution, $k = 0.267\ \text{mm}^{-1}$. With this approximation for the current gain, the number n of electrons doubles every 2.6 mm along the length. If so, a change in the length of about 8.8 mm is sufficient to account for the variation. The pulse heights from the central region of a pulse height profile are about 10 times smaller than those from the cone region. However, an estimate of the current gain of a length of about 11 mm in the straight channel section gives a change of gain of about 19. So, according to this approximate argument, there was some saturation during the measurements. The variation of the pulse height profile, which occurs in the cone region must be accounted for by electron multiplication in the cone itself.

With sufficiently low discriminator threshold levels of the single channel analyzer and scaler in the pulse counting system as described in section III-3 of Chapter III, the detection efficiency is found to be uniform over the whole entrance aperture with no change between the cone and the channel.

There are previous experimental investigations[37] for a low momentum electrons or atomic hydrogen ions incident on a channeltron with conical or non-conical entrance aperture. Among these previous results, Ray and Barnett[37] observed for 20 keV protons incident on a Mullard Model B419BL channeltron with a circular entrance aperture both the asymmetric pulse height profile and the uniform efficiency over the whole entrance aperture similar to the present results, but they observed about three-fold decrease in the pulse heights from the protons which entered the channel compared with those that struck the cone. The pulse height variation is much smaller than the present result, probably because the momentum of the protons is smaller than that of the present 100 keV N_1^+ ions. The present results for the rectangular conical channeltron are probably applicable to other channeltrons having circular entrance cones.

REFERENCES

1. B. Hird and H. C. Suk, "Single-electron stripping cross of N_1^+ in Ne, Ar, and Kr between 35 and 140 keV", Phys. Rev., A14 (1976)928

2. B. Hird, H. C. Suk, and A. Guilbaud, "Channeltron entrance aperture gain variations for energetic heavy ions" Rev. Sci. Instrum., 47(1976)138

3. R. T. Brackmann and W. L. Fite, Experimental Research on Collisions of Heavy Particles at Energies up to 2 MeV", AFWL-TR-68-96(U.S.A.), (1968), (Unpulished)

4. L. I. Pivovar, M. T. Novikov, and A. S. Dolgov, Soviet Phys.-JETP, 23(1966)357

5. I. S. Dimitriev, V. A. Nikolaev, L. I. Fateeva, and Ya. A. Teplova Soviet Phys.-JETP, 15(1962)11

6. L. P. Flaks and E. S. Solov'ev, Soviet Phys.-Tech. Phys., 3(1958)564 & 577

7. N. V. Fedorenko, Zh. Tech. Fiz.(U.S.S.R.), 24(1954)769

8. H. Klinger, A. Müller and E. Salzborn, J. Phys.-B: Molec.Phys., 8(1975)230

9. D. Rapp and W. E. Francis, J. Chem. Phys., 37(1962)2631

10. A. R. Lee and J. B. Hasted, Proc. Phys. Soc., 85(1965)673

11. H. S. W. Massey, Rep. Progr. Phys. 12 (1948-9)248.

12. J. B. Hasted and A. R. Lee, Proc. Phys. Soc., 79(1962)702

13. O. B. Firsov, Soviet Phys.-JETP, 9(1959)1076

14. E. F. Gurnee and J. L. Magee, J. Chem. Phys., 26(1957)1237

15. I. Popescu Iovitsu and N. Ionescu-Pallas, Soviet Phys.-Tech. Phys., 4(1960)781

16. A. Dalgarno, Phil. Trans. Roy. Soc., A250(1958)426; A. Dalgarno, M. R. C. McDowell, and A. Williams, Phil. Trans. Roy. Soc., A250(1958)411; A. Dalgarno and M. R. C. McDowell, Proc. Phys. Soc., A69(1956)615

17. L. I. Schiff, "Quantum Mechanics", McGraw-Hill Book Company, Inc., New York, (1955), p236-239

18. N. Rosen and C. Zener, Phys. Rev., 40(1932)502

19. B. G. Skinner, Proc. Phys. Soc., A77(1961)551

20. "Handbook of Mathematical Functions with Formulas, Graphs, and Mathematical Tables", Ed. by M. Abramowitz and I. A. Segun. Dover Publ., Inc., New York, (1968) p378

21. L. Landau, Z. Phys. Sowjet, 2(1932)46

22. C. Zener, Proc. Roy. Soc., A137(1932)696

23. E. C. G. Stüeckelberg, Helv. Phys. Acta. 5(1932)370

24. M. H. Mittleman and L. Wilets, Phys. Rev., 154(1967)12

25. A. Russek and M. T. Thomas, Phys. Rev., 109(1958)2015
A. Russek and M. T. Thomas, Phys. Rev., 114(1959)1538
J. B. Bulman and A. Russek, Phys. Rev., 122(1961)506
A. Russek Phys. Rev., 132(1963)246

26. H. H. Fleischmann, R. C. Dehmel and S. K. Lee, Phys. Rev., A5(1972)1784

27. H. H. Lo and A. L. Fite, Atomic Data, 1(1970)305

28. R. C. Dehmel, H. K. Chau, and H. H. Fleischmann, Atomic Data, 5(1973)231

29. M. Islam, J. B. Hasted, H. B. Gilbody, and J. V. Ireland, Proc. Phys. Soc., 79(1962)1118

30. I. K. Fetisov and O. B. Firsov, Soviet Phys.-JETP, 10(1967)67

31. A. L. Hughes and V. Rojansky, Phys. Rev., 34(1929)284

32. R. Herzog, Z. Naturforsch, 10a(1955)887
R. Herzog, Phys. Z., 41(1940)18
R. Herzog, Z. Phys., 97(1935)596

33. H. Wollnik, in "Focussing of Charges particles", Ed. by A. Septier, Vol.II(1967), page 163, Academic Press, New York and London; H. Wollnik and H. Ewald, Nucl. Instrum. and Meth., 36(1965)93

34. R. G. Dromey, J.D. Morrison, and J. B. Peel, ReV. Sci.Instrum., 44(1973)913;
M. Arnow and D. R. Jones, Rev. Sci. Instrum., 43(1972)72;
A. D. Johnstone, Rev. Sci. Instrum. 43(1972)1030.
J. J. Leventhal and G. R. North, Rev. Sci. Instrum, 42(1971)120;
P. Bryce, R. L. Dalglish, and J. C. Kelly, Can. J. Phys., 51(1973)574;

D. Roy and J. -D. Carette, Appl. Phys. Lett., 16(1970)413;
H. Matsuda, Rev. Sci. Instrum, 32(1961)850;
H. G. Voorhies, Rev. Sci. Instrum., 26(1955)716
H. Ewald and H. Liebl, Z. Naturforsch, 10a(1955)872
T. Kitagaki, Sci. Repts., Tôoku Univ., First Ser., 44(1970)32;
E. G. Johnson and A. O. Nier, Phys. Rev., 91(1953)10;
N. Savartholm, Ark, Pys., 2(1950)195

35. L. H. Toburën, M. Y. Nakai, and R. A. Langley, Oak Ridge National Lab. Report, ORNL-TM-1988(1969)

36. G. N. Patterson, "Introduction to the Kinetic Theory of Gas Flows", Univ. of Toronto Press, (1971) page 112

37. D. H. Crandall, J. A. Ray, and C. Cisneros , Rev. Sci. Instrum. 46(1975)562;
R. L. Arnoldy, P. O. Isaacson, and D. F. Gats, Rev. Sci. Instrum., 44(1973)172;
J. A. Ray and C. F. Barnett, IEEE Trans. Nucl. Sci., NS-17(1) (1970)44;
B. Tatry, J. M. Bosqued, and H. Reme, Nucl. Instrum. and Meth., 69(1969)254;
C. N. Burrous, A. J. Lieber, and V. T. Zaviantseff Rev. Sci. Instrum., 38(1967)1477;
A. Egidi, R. Marconero, G. Pizzella, and F. Sperli, Rev. Sci. Instrum. 40(1969)88;
E. Yellin, L. I. Yin, and I Adler, Rev. Sci. Instrum., 41(1970)18;
J. F. Cuderman, Rev. Sci. Instrum., 42(1971)1094;
G. E. Iglesias and J. O. McGarity, Rev. Sci. Instrum., 42(1971)1728;
R. J. Archuleta and S. E. DeForest, Rev. Sci. Instrum. 42(1971)89;
G. Pashmann, E. G. Shelley, C. R. Chappell, L. F. Smith, and R. D. Sharp, Rev. Sci. Instrum., 41(1970)1706;

38. A. B. Wittkower and H. B. Golbody, Proc. Phys. Soc., 90(1967)353

39. G. J. Lockwood, Phys. Rev. A7(1973)125.